UNIVERSITY OF NAIROBI

DEPARTMENT OF PHYSICS

Fabrication and Characterization of TiO_2/Nb_2O_5 Composite Photo-Electrodes Deposited Using Electrophoretic Technique for Application in Dye-Sensitized Solar Cells

John Njagi Nguu

I80/82761/2012

Department of Physics

University of Nairobi

Kenya.

A Thesis Submitted in Fulfillment of the Requirements for Award of the Degree of Doctor of Philosophy in Physics of the University of Nairobi

December 2017

DECLARATION

I declare that this thesis is my original work and has not been submitted elsewhere for examination, award of a degree or publication. Where other people's work or my own work has been used, this has been acknowledged and referenced in accordance with the University of Nairobi's requirements.

Signature _____ .Date 14/12/2017

John Njagi Nguu
I80/82761/2012
Department of Physics
School of Physical Sciences
University of Nairobi

This thesis is submitted for examination with our approval as research supervisors:

Prof. Bernard O. Aduda
Department of Physics
University of Nairobi
P. O. Box 30197-00100
Nairobi, Kenya

Signature _____ Date 15/12/17

Dr. Francis W. Nyongesa
Department of Physics
University of Nairobi
P. O. Box 30197-00100
Nairobi, Kenya

Signature _____ Date 15/12/17

Dr. Robinson J. Musembi
Department of Physics
University of Nairobi
P. O. Box 30197-00100
Nairobi, Kenya

Signature _____ Date 15/12/2017

DEDICATION

I dedicate this thesis to my beloved wife Susan Mumbua and our children Victor, Nicholus and Joyesther who stood by me and encouraged me during the study.

ACKNOWLEDGEMENTS

I would like to thank our heavenly Father for giving me the ability and resources that enabled me study and complete my PhD studies.

Special thanks to my University advisors Prof. B. O. Aduda, Dr. F. W. Nyongesa, and Dr. R. J. Musembi for their guidance and advice during the course of this study. I acknowledge support of members of Department of Physics, University of Nairobi (UON) especially those in the Condensed Matter Group.

I am very thankful to Daystar University management board for allocating me a reduced workload and awarding me a scholarship to cover the tuition for my studies at the University of Nairobi. I am indebted to my Daystar University colleagues for moral support through the course of this study.

Special acknowledgement is to the National Commission for Science, Technology and Innovation (NACOSTI) and International Programme in Physical Sciences (IPPS) for financially supporting the sourcing of the chemicals, equipment, and materials used in this work. I thank the management at Chuka University (Kenya) for allowing me use the Hall Effect apparatus. I am grateful to Henry Barasa and Frandsen of the Joint United States Africa Materials Initiative (JUAMI) for facilitating my use of both the SEM and XRD.

ABSTRACT

This study has investigated a rapid, simple and cost effective electrophoretic deposition (EPD) technique for fabrication of nanoparticulate TiO_2/Nb_2O_5 composite electrode films for use in dye-sensitized solar cells (DSSCs). The EPD technique parameters were categorized into suspension-related and process-related parameters. The suspension-related parameters were maintained constant by fixing the solvent (2-propanol), charging system ($Mg(NO_3)_2.6H_2O$), pH (≈ 4.9) of suspension and EPD apparatus. The optimized process-related parameters of EPD technique obtained were: particle concentration (0.25 g/L), DC applied voltage (35V), and deposition time (90s). The optical properties like light absorption, transmission, extinction coefficient, Urbach energy, refractive index, and optical band gap energy of the composite thin films were investigated in this study. Band gap energies (E_g) for pure TiO_2, (3.932 eV), pure Nb_2O_5 (3.858 eV) and TiO_2/Nb_2O_5 composite films (3.884eV) were obtained based on the plot of the Tauc equation. The theoretical E_g of TiO_2 is =3.25 eV and E_g =3.49 eV for Nb_2O_5. The difference between theoretical and experimental values of E_g for both pure TiO_2 and Nb_2O_5 films was explained in terms of development of sub-band gap states lying deep in the tail of density of states in the TiO_2/Nb_2O_5 composite films. The band gap decreased slightly from 3.8911eV for films annealed at 450°C for 1 hour to 3.7965 eV for similar films annealed at same temperature for 6 hours. The narrowing of band gap was attributed to the decrease in transitions due to reduction of the oxygen defect width as a result of air annealing which fills up the vacant oxygen levels.

Light is absorbed in a material when extinction coefficient (k) is greater than zero i.e., $k > 0$, while light travels straight through the material when $k = 0$. In this study, a value of 0.0354 at $400 \leq \lambda \leq 700$nm was obtained for extinction coefficient which means there was some absorption of light by the TiO_2/Nb_2O_5 composite electrode thin films due to their large band gap energy. The results were consistent with the knowledge about high band gap semiconductors that must require sensitization with a dye to function as photoelectrodes in a dye sensitized solar cells.. The relatively small extinction coefficient was attributed to low absorption of light by the TiO_2/Nb_2O_5 composite electrode thin film due to its large energy band gap. The calculations of Urbach energy (E_U) yielded a value equal to 454 meV, which

indicated substantial introduction of tail states at the band edges that influence the electron transport. The average refractive index (n) of 1.643 was obtained for wavelengths between 1800nm and 2800nm.

The majority carriers in the TiO_2/Nb_2O_5 composite films were found to be electrons (n-type) which could be caused by caused by incorporation of Nb^{+5}, and O^{-2} ions in the composite. Charge carrier density (n_d) value for TiO_2/Nb_2O_5 composite films were 6.14 x 10^{18} cm^{-3} which was lower than the value (1.00 x 10^{19} cm^{-3}) reported in existing research. This was attributed to electrons trapping in surface states of the high surface area composite film while reduction of carrier mobility could have resulted from increased grain boundaries between the Nb_2O_5 and TiO_2 nanoparticles in a composite film. The SEM images showed the TiO_2/Nb_2O_5 composite films were devoid of cracks and essential for dye adsorption. Both TiO_2 and Nb_2O_5 nanoparticles were shown, by XRD graphs, to be presented in the composite films in the ratio 1.78:1 (or 1:0.56). The XRD graphs confirmed that surface of both TiO_2 and Nb_2O_5 particles suspended in 2-propanol became charged and therefore the charged particles were moved and deposited on oppositely charged electrode by the applied electric field. The XRD revealed dominant peak of TiO_2 at $2\theta = 25.5°$ and that of Nb_2O_5 at $2\theta = 26.5°$. Applying Scherer's equation, the average crystallite sizes at these peak positions were 15.36 nm and 15.49 nm and hence the crystallite dimensions were confirmed to the nanoscale.

The solar cell produced using the composite thin film had the following parameters: V_{OC} = 0.66V, J_{SC} = 5.25 mA/cm^2, *FF* = 0.57, and η = 2. The low conversion efficiency observed was accredited to factors such as composition of the composite, morphological defects, poor adhesion between film and FTO, or the type of dye used. Nonetheless, efficiencies in these types of devices where the electrode is deposited by EPD has remained low. Internal resistances were investigated by EIS measurements to explain the low cell efficiencies. All the cells exhibited the Gerischer impedance (R_D) characterized by Nyquist plot having a single, main arc in which impedance was associated with the electron recombination with electrolyte species being faster than the transport of electron within the TiO_2 film. The faster back reaction could have been caused by the relatively poor adhesion of the film on to FTO glass slides. The poor adhesion introduced high transport resistance and low interfacial (recombination) resistances. Blocking the electron leak by structural modification that includes developing a more compact composite structure and improved film/FTO glass

adherence that enhances electron conduction across the interface may be a possible way to obtain high JSC s and efficiencies in DSSCs.

Key words: Dye-sensitized solar cell, electrophoretic deposition, niobium (v) oxide, TiO_2/Nb_2O_5 composite electrode thin film, electrochemical impedance spectroscopy.

TABLE OF CONTENTS

LIST OF TABLES

LIST OF FIGURES

LIST OF SYMBOLS, ABBREVIATIONS, AND ACRONYMS

SYMBOLS

A	Surface area
B	Magnetic field
c	Particle (power) concentration in the suspension
CFC	Trichlorofluoromethane
CH_4	Methane
CO_2	Carbon dioxide
C_μ	Chemical capacitance
d	Electrode separation in EPD technique
d_{hkl}	Inter planar spacing of the crystal
D^*	Excited dye
D^+	Oxidized dye
D_n	Diffusion coefficient
E_{CB}	Conduction band energy
E_F	Fermi level energy
E_g	Optical band gap energy
E_U	Urbach energy
E_{VB}	Valence band energy
EJ	Exajoule (= 10^{18} Joules)
E_s	Electrical field strength
f	Volume fraction of one of the particles in the mixed nanoparticle composite
F_E	Electric force
F_B	Magnetic force
GaAs	Gallium Arsenide
h	Planck's constant
I_0	Amplitude of current signal
I^-/I_3^-	Iodide/triiodide

$I_2^{-\bullet}$	Di-iodide radical
I^*	Light intensity
I_{SC}	Short-circuit current
j	Imaginary number
$j_{\max}$	Current density at maximum power
j_0	Reverse saturation current
J_{SC}	Short-circuit current density
k	Extinction coefficient
k_B	Boltzmann's constant
l	Width
L_d	Electron diffusion length
m	Deposited mass
mL	Milliliter
$\overline{n}$	Complex refractive index
n_c	Refractive index of composite film
n_d	Charge carrier density
n_f	Refractive index of thin film
n_N	Refractive index of one nano particle N in composite
n_s	Refractive index of glass substrate
n_T	Refractive index of nanoparticle T in the composite
Nb_2O_5	Niobium (v) oxide
N_2O	Nitrous oxide
N719	Cis-bis(isothiocyanato)-bis(2,2'-bipyridyl-4,4'-dicarboxylato) ruthenium(II) bis-tetrabutylammonium
PJ	Peta-Joule (= 10^{15} Joules)
Pt	Platinum
P_{in}	Incident power
q	Elementary charge (= 1.6×10^{-19} Coulomb)

R_d	Diffusion resistance of ions in electrolyte
R_{DC}	DC resistance
R_H	Hall coefficient
R_t	Electron transport resistance
R_P	Parallel resistance
R_r	Recombination resistance
R_S	Sheet resistance
R_{SH}	Shunt resistance
R_{TCO}	Charge-transfer resistance for electron recombination from uncovered layer of TCO to electrolyte
R_{tot}	Total resistance of the solar cell
C_{TCO}	Capacitance at the triple contact TCO/TiO_2/electrolyte interface.
t	Deposition time
tBP	4-tert-butylpyridine
TiO_2	Titanium dioxide (titania)
τ_n	Electron lifetime
T_{emp}	Temperature
%T	Transmittance
T_{max}	Transmission spectra maximum
T_{min}	Transmission spectra minimum
Si	Silicon
S_λ	Energy per time per unit area
v_x	Average velocity
V_H	Hall voltage
V_O	Amplitude of voltage signal
$V\,\max$	Voltage at maximum power
V_{OC}	Open circuit voltage
Δw	Full width at half maximum
ω	Angular frequency
ω_d	Characteristic frequency of diffusion of redox ions in electrolyte
ω_r	Frequency of electron recombination with redox species

Y_0	Diffusion admittance.
z	Film thickness
Z	Impedance
$Z^{/}(\omega)$	Real component of impedance
$Z^{//}(\omega)$	Imaginary component of impedance
Z_C	Capacitive reactance
Z_{CPE}	Capacitive reactance of constant phase element
Z_d	Warburg impedance
$\|Z\|$	Magnitude value of impedance
α	Absorption coefficient
ε	Dielectric constant
η	Light-to-electric energy conversion efficiency
λ	Wavelength
ρ	Resistivity
σ	Electrical conductivity
μ_E	Electrophoretic mobility
μ_H	Hall mobility
ν	Frequency
ψ	Viscosity of the suspension
ϕ	*P*hase angle between excitation and response signals
ς	Permittivity
ξ	Zeta potential

ABBREVIATIONS AND ACRONYMS

AM	Air mass
AFM	Atomic force microscope
CCD	Charged chemical device
CE	Counter electrode
CdTe	Cadmium telluride
cP	Centipoise (= 10^{-3}dyn-s/cm^2)

CPE	Constant phase element
CIGS	Copper indium gallium selenide
DCV	Applied DC voltage
DSSC	Dye-sensitized solar cell
EPD	Electrophoretic deposition
EQE	External quantum efficiency
ESC	Excitonic solar cells
ETA	Extremely thin absorber-layer
eV	Electron volt (=$1.6x10^{-19}$ Joules)
FF	Fill Factor
FTO	Fluorine-doped tin oxide ($F:SnO_2$)
HFC-23	Fluoroform
HOMO	Highest occupied molecular orbital
IEP	Isoelectric point
LUMO	Lowest unoccupied molecular orbital
NREL	National Renewable Energy Laboratory (USA)
nm	Nanometer (10^{-9}m)
PV	Photovoltaic
SEM	Scanning electron microscope
TCO	Transparent conductive oxide
V_H	Hall voltage
XRD	X-ray diffraction
Zp	Zeta potential

CHAPTER ONE

INTRODUCTION

1.1 Background

Technological development, economic growth, and environmental stability depend on the availability of reliable and adequate energy sources. The world currently uses energy at a rate of $4.1x10^{20}$Joules per year, equivalent to power supply of 13 terawatts (TW). This energy consumption is expected to double (to 26TW) by 2050, and more than triple (to 46TW) by 2100 due to rapid technological measures and projected increase in Earth's population (to 9 billion) Crabtree & Lewis, 2007). Table 1.1 shows the primary energy consumption in million tonnes oil equivalent (Mtoe) (where 1 Mtoe = $4.1868x10^{16}$J) consumed in the world per year in different years. Around 87% of primary energy consumed in the world today is derived from fossil fuels, namely oil, natural gas and coal (Table 1.1) because their energy density is higher than that of other energy sources. The harnessing of energy from fossil fuels may, however, be unable to satisfy the growing energy demand (Crabtree & Lewis, 2007).

Table 1.1: World primary energy utilization (consumption) by fuel in million tonnes oil equivalent (Mtoe) (BP- statistical review of world energy reports, 2015)

Million tonnes oil equivalent (Mtoe)	2009	2010	2011	2012	2013	2014
Oil	3908.7	4031.9	4081.4	4138.9	4179.1	4211.1
Natural gas	2661.4	2843.1	2914.2	2986.3	3052.8	3065.5
Coal	3305.6	3532.0	3628.8	3723.7	3867.0	3881.8
Nuclear energy	614.0	626.3	600.4	559.9	563.7	574.0
Hydroelectricity	736.3	778.9	794.7	833.6	861.6	879.0
Renewables*	137.4	165.5	205.6	240.8	283.0	316.9

*(geothermal, wind, solar, wood); 1 Mtoe = $4.1868x10^{16}$J

The continued consumption of fossil fuels at the current rate, these sources will be completely depleted in the next 30 – 225 years depending on the type, also the CO_2 emission is a major concern to global warming. Table 1.2 shows list of greenhouse gases and their respective atmospheric lifetime in years.

Table 1.2: Greenhouse gases: gas concentration, global warming potential (GWP) and lifetime (Blasing, 2014).

Gas	Pre-1750 tropospheric concentration	Recent tropospheric concentration	GWP (100-yr time horizon	Atmospheric lifetime (years)
Gas concentration in parts per million (ppm)				
Carbon dioxide (CO_2)	280	395.4	1	100-300
Gas concentration in parts per billion (ppb)				
Methane (CH_4)	722	1762	28	12
Nitrous oxide (N_2O)	. 270	324	265	121
Tropospheric ozone (O_3)	237	337	n.a.	hours-days
Gas concentration in parts per trillion (ppt)				
CFC-11 (CCl_3F)	zero	234	4,660	45
CFC-12 (CCl_2F_2)	zero	527	10,200	100
CFC-113 (CCl_2CClF_2)	zero	74	5,820	85
HCFC-22 ($CHClF_2$)	zero	210	1,760	11.9
HCFC-141 (CH_3CCl_2F)	zero	21	782	9.2
HCFC-142 (CH_3CClF_2)	zero	21	1,980	17.2
Carbon tetrachloride (CCl_4)	zero	83	1,730	26

(GWP) Global warming potentials.

In order to mitigate against these challenges of climatic change and energy insecurity, three prominent options have been proposed namely (i) decarbonizing fossil fuels by capturing and sequestering carbon, (ii) use nuclear fusion power as the energy source, and (iii) improving energy efficiency and investing in renewable energy generation. Besides nuclear fusion renewable energy source, solar energy has the largest potential to meet the global energy need in the future (Schiermeier *et al*., 2008). Both nuclear fission and fusion are carbon-free energy generation processes and thus beneficial to environment. Main concern, however, about nuclear fission regards securing Uranium-235 and the power plant as well as disposing nuclear waste. Nuclear fusion currently takes place in laboratory experiments on a small scale where research is ongoing to make it feasible for large-scale energy production. The challenge of developing nuclear fusion is in containing the fusion materials since very high temperatures and high pressures are required. On the other hand, solar energy is ubiquitous, environmentally benign, and a source of renewable energy with almost unlimited supply capability. Solar energy, unlike geothermal, hydro, or wind energy is distributed evenly on

Earth as shown in Figure 1.1. It can be seen in Figure 1.1, that most countries of the world potentially could use solar energy as the main energy resource, especially the places along the equator.

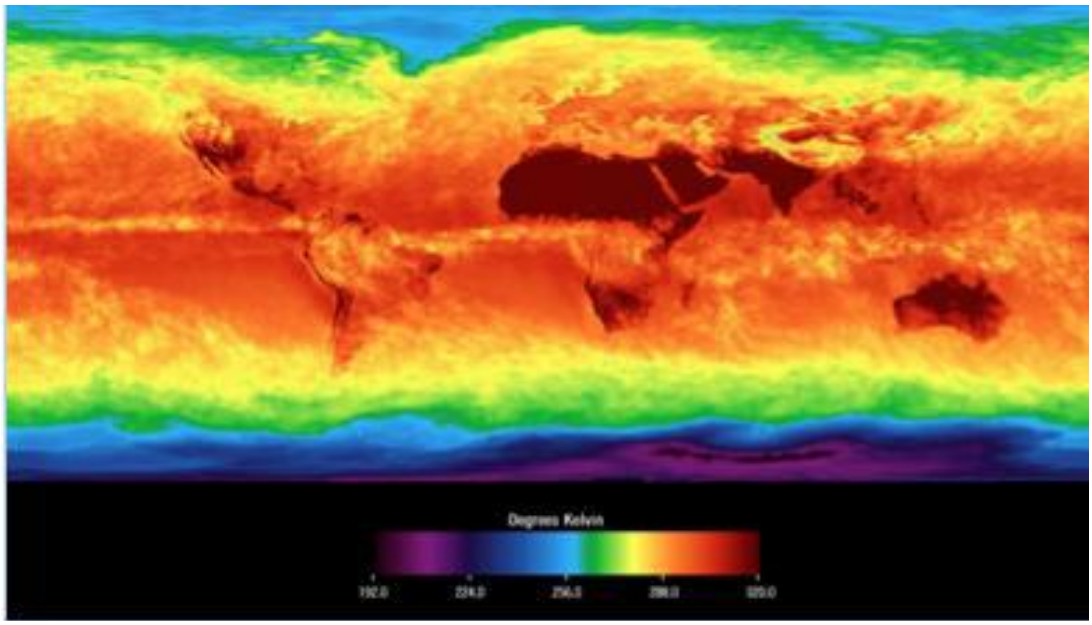

Figure 1.1: NASA Map of the world solar energy potential (Pentland, 2010).

The mean solar radiation reaching the Earth is estimated at 120,000 TW compared to 13 TW the mean global energy consumption (Lee *et al.*, 2009). Despite this huge potential, solar electricity provided about only 2% of the world's electricity in 2016 (IRENA, 2016). The huge gap between the abundant solar radiation and the present use of the solar energy presents a great challenge to research and development (R&D) efforts to develop cost-effective solar cell technologies.

Solar energy conversion systems are classified into two categories: (i) technological systems for direct solar energy conversion, and (ii) technological systems for indirect solar energy conversion (Quasching, 2005). Examples of direct solar energy conversion include; solar thermal power plants, photolysis transformation systems for fuel production, solar-water heaters and photovoltaic solar cells. Examples of indirect solar energy conversion methods include wind to electricity using the wind turbine generators, hydroelectric energy from river water and biofuel energy, which mainly includes biodiesel, biomass and biogas (Musembi, 2009).

This study focuses on the photovoltaic (PV) solar cell which works by converting absorbed light photons directly into electrical charges used to energize an external load. Electric energy is a convenient form of energy and the interest in conversion of abundant solar energy into electric energy has been driven principally by the great, long term energy potential and possible reduction of poverty in developing countries (Musembi, 2009). Solar cells were first used in space explorations. In addition, solar cells are used in remote locations off grid standalone systems such as street lamps and harbor beacons. In Kenya, it is estimated that only 5.5% of households and 23% businesses are connected to the grid (Lee *et al*., 2016). Photovoltaic cell research has resulted in the fabrication of different types of solar cells based on their performance and cost effectiveness.

Existing PV solar cells have been categorized into three generations with the first generation consisting of silicon bulk multi-junction cells, second generation consisting of thin film (amorphous Si, CIGS, CdTe and $Cu_2ZnSn(SSe)_4$) solar cells, and third generation consisting of organic photovoltaics (OPVs) and dye-sensitized solar cells (DSSCs). As shown in Figure 1.2, the commonly used single crystal silicon solar cells have a positive attribute of high power conversion efficiencies (25.0%). These cells, though dominant in the solar energy market, are expensive to fabricate partly due to the high cost of processing highly purified solar grade silicon using vacuum-based techniques. Power production of silicon based PV solar cells is limited by reserves of silver, which is used as an electrode (Feltrin & Freundlich, 2008).

A lot of research is therefore, geared towards developing low cost PV solar cells with adequate conversion efficiencies (Takamoto *et al.,* 2005). Consequently, among the emerging technologies, the DSSCs have gained widespread attention owing to their relatively low production costs, simple manufacturing techniques, great aesthetic features like color, potential for indoor and outdoor applications and fair photon to electron energy conversion efficiencies (Snaith, 2010). Table 1.3 and Figure 1.2 presents the historical progress of the best reported research cell efficiencies from various solar cell technologies to date (National Renewable Energy Laboratory (NREL), 2016).

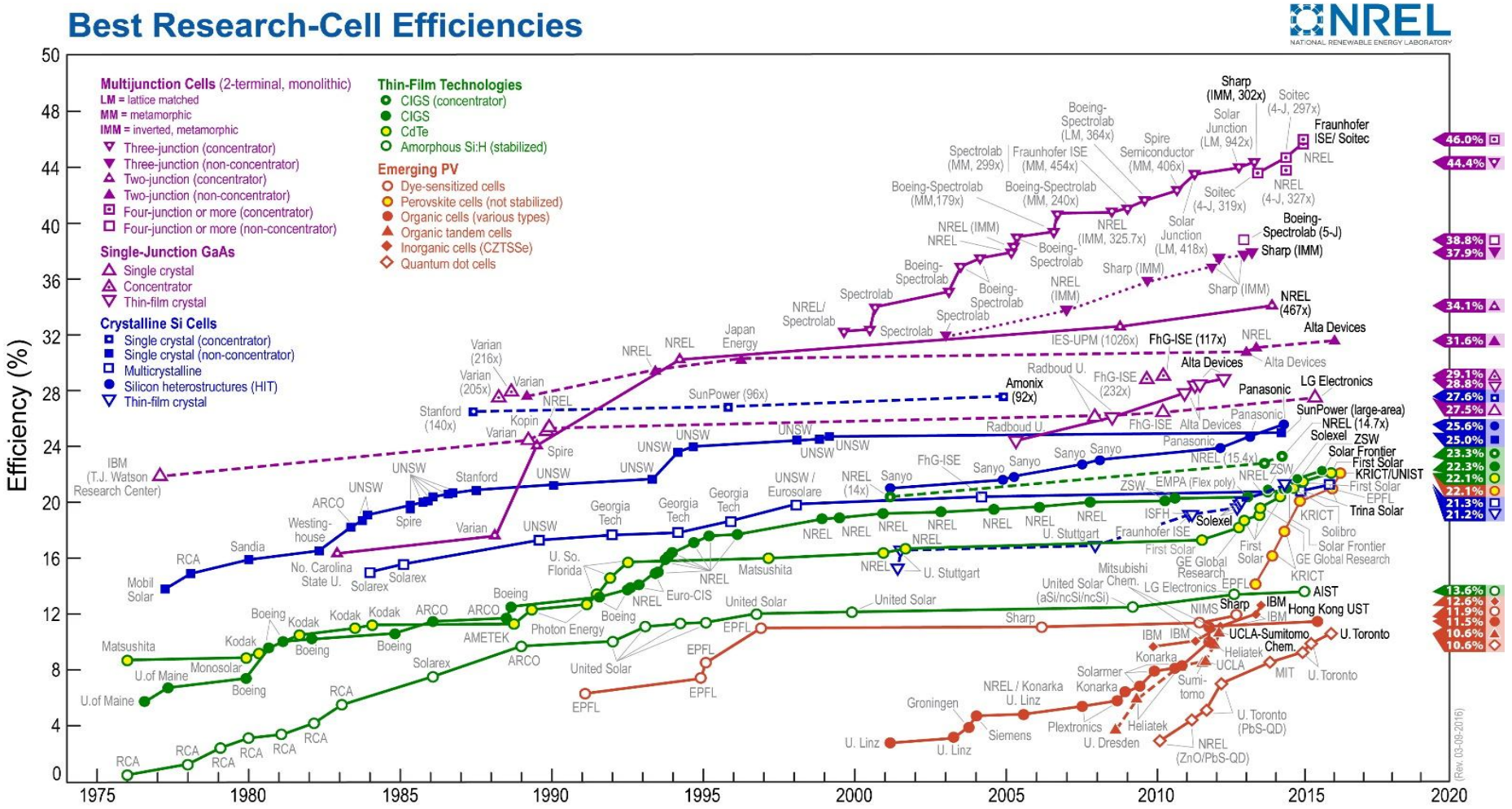

Figure 1.2: Record research-solar cell efficiencies reported by National Renewable Energy Laboratory (NREL)Source: NREL, 2016 Downloaded from http://www.nrel.gov/ncpv/images/efficiency_chart.jpg Jan 2016.

The typical structure of a DSSC comprises a photoelectrode (anode) consisting of a porous and nanocrystalline wide-band gap semiconductor thin film, an electrolyte containing red-ox couple typically iodide/triiodide (I^-/I_3^-), an organic dye sensitizer, and a counter electrode (CE) (cathode). O'Regan and Gratzel (1991) first reported a dye-sensitized solar cell (DSSC) based on highly effective dye-sensitized nanoporous and nanocrystalline titanium dioxide (TiO_2) film and which provided a conversion efficiency of 7.1%. Following intense research studies on DSSC from many research groups, the current light-to-electric energy-conversion efficiency (η) of liquid electrolyte-based DSSC using porous nanocrystalline TiO_2 stands at 11.8 % (Yella *et al.,* 2011). However, the conversion efficiency of solid-electrolyte based DSSC (Perovskite) stands at 15%, despite concerns being raised about the high lead content in perovskite material (Burschka *et al*., 2013).

Table 1.3: World record solar cell efficiencies for laboratory and research devices reported by National Renewable Energy Laboratory (NREL, 2016)

Type of cell	Description	Efficiency (%)
Multijunction Cells	Three-junction (concentrator)	43.5%
	Three junction (non-concentrator)	34.1%
	Two-junction (concentrator)	32.6%
Single Junction GaAs	Single crystal	26.4%
	Concentrator	29.1%
	Thin film crystal	28.8%
Crystalline Si Cells	Single crystal	27.6%
	Multicrystalline	20.4%
	Thick Si film	NA
	Silicon Heterostructures (HIT)	23.0%
Thin-Film Technologies	CIGS	20.3%
	CdTe	17.3%
	Amorphous Si:H (Stabilized)	12.5%
	Multijunction polycrystalline	NA
Emerging PV	Dye-sensitized cells	11.9%
	Perovskite	15.0%
	Organic cells (various types)	10.6%
	Organic tandem cells	10.6%
	Inorganic cells	11.1%
	Quantum dot cells	5.1%

NA: Not available

However, the photocatalytic activity of TiO_2 is so high in ultra-violet radiation in natural sunlight that organic materials in DSSC may decompose during outdoor use resulting in long-term reliability problems for the conversion efficiency (Ito *et al.,* 2008). Consequently, other porous metal oxide electrodes with much lower photocatalytic activity have been examined. They include, binary metal oxides such as ZnO (Chiu *et al.*, 2011; Yan *et al.*, 2012; Benehkohal, 2013), Nb_2O_5 (Rani *et al*., 2014), Al_2O_3 (Quedraogo & Savadogo, 2013), SnO_2 (Ito *et al*., 2004), CeO_2 (Jose *et al.,* 2009) and composites such as ZnO/TiO_2 (Yan *et al.,* 2012), ZnO/SnO_2, (Chen *et al*., 2009; Pan *et al*., 2012), MgO/TiO_2, (Wu *et al*., 2008), SnO_2/CeO_2 (Ito *et al.,* 2008), ZnO/ZnS (Rouhi *et al.,* 2015), and ZrO_2/TiO_2 (Wang, *et al.,* 2012). Table 1.4 compares photovoltaic performances of DSSCs using composites, doped and core shell photoelectrodes. The d-block transition metal oxides (Fe_2O_3, TiO_2 and ZnO) promise to be the best candidates as photoelectrodes in DSSCs due to the orbital dissimilarities comprising their valence bands and conduction bands (Jose *et al.,* 2009). These orbital dissimilarities decrease the probability of charge recombination and enhance the carrier lifetime in these materials.

Table 1.4: Photovoltaic performances of DSSCs using composites, doped and core- shell photoelectrodes.

Type of electrode	**Composition**	**Efficiency (%)**	**Source**
TiO_2-metal oxide composite	TiO_2/ZrO_2	5.8	Kitiyanan & Yoshikawa, (2005)
	TiO_2/GeO_2	5.7	Kitiyanan *et al*., (2006)
	TiO_2/Nb_2O_5	1.9	Eguchi *et al*., (2000)
	TiO_2/ZnO	1.87	Yan *et al*., (2012)
Doped TiO_2	TiO_2_ZrO_2	8.1	Durr *et al*., (2006)
	TiO_2_Nb_2O_5	1.8	Jose *et al.*, (2009)
TiO_2 core-shell metal oxide structures	TiO_2-ZrO_2	3.6	Palomares *et al.,* (2003)
	TiO_2-Nb_2O_5	4.7	Zaban *et al*., (2000)
	TiO_2-ZnO	4.5	Yan *et al.,* 2012
	TiO_2-SiO_2	4.4	Roh *et al*., (2006)
	TiO_2-Al_2O_3	5.6	Palomares *et al*., (2002)
	TiO_2-$SrTiO_3$	4.4	Diamant *et al*., (2003)

The TiO_2 and Nb_2O_5 structures (composite and doped TiO_2) have reported low efficiencies compared with structures of other combinations (Table 1.4). The efficiencies from doped and composite structures compare closely for compositions shown. Composite photoanodes of more than one material have gained interest because they seek to take advantage of best properties of each component that forms the composite (hybrid). The concept of a composite goes way beyond a mixture and falls between the concept of a mixture and a compound. The composite concepts, therefore, fall in a category where the interface between the components is increased compared to a mixture (Yacaman *et al.,* 1996).

Additionally, the potential of using titanium dioxide and niobium (v) oxide (TiO_2/ Nb_2O_5) composite has not been fully elucidated. The conduction band of Nb_2O_5 lying at least 0.25V above that of TiO_2 could make it suitable for the formation of mixed-particles structures which could result in a higher DSSC photovoltage (Wei *et al.,* 2008). It is of interest to study TiO_2/Nb_2O_5 composite electrode films fabricated with the goal of exploiting the advantages of Nb_2O_5 which include its high stability, high conduction band energy and high transport rate of injected electrons from dye molecules in DSSC application (Lee *et al.,* 2009). Further, it will be of interest to explore the electrophoretic deposition technique for film preparation.

1.2 Problem Statement

Film deposition techniques such as screen printing, doctor blade, and sol-gel have been explored to prepare porous photoelectrode thin films for application in solar cells. The Sol gel and electrophoretic deposition (EPD) techniques have been used in vehicle painting. Bandy *et al*., (2011), fabricated a DSSC based on electrophoretically deposited TiO_2 photoelectrodes, which produced a relatively high (η = 4.91%) conversion efficiency. Notably, the EPD technique has not been fully exploited in the fabrication of electrodes for application in dye-sensitized solar cells despite being a relatively inexpensive technique which could be scaled up for mass production if successfully developed. Additionally, the potential of using titanium dioxide and niobium (v) oxide (TO_2/Nb_2O_5) composite has not been fully developed. In this study, we seek to optimize the parameters of electrophoretic deposition technique for fabrication of nanocrystalline and porous TiO_2/Nb_2O_5 composite electrode thin films and characterize the films and the assembled dye-sensitized solar cells.

1.3 Aim of the Study

The aim of this study is to fabricate and characterize TiO_2/Nb_2O_5 composite thin film electrodes deposited using the electrophoretic technique for application in dye-sensitized solar cells.

Specific objectives

The specific objectives of the study are:

1. To optimize electrophoretic deposition (EPD) parameters for fabrication of TiO_2/Nb_2O_5 composite electrode thin films;
2. To perform structural and morphological characterization of TiO_2/Nb_2O_5 composite electrode thin films;
3. To carry out optical and electrical characterization of TiO_2/Nb_2O_5 composite electrode thin films;
4. To fabricate and characterize a TiO_2/Nb_2O_5 based DSSC solar cell through I-V and EIS characterizations.

1.4 Justification and Significance of the Study

The charge injection and transportation are processes that occur within a photoelectrode and influence the light to electric energy conversion efficiency in a DSSC. Titanium (IV) oxide (TiO_2) is a key semi-conducting material for fabricating photoelectrodes since they were successfully employed in 1991 by O'Regan and Gratzel for DSSCs. However, the efficiency of DSSC is fairly low compared with that of the established silicon based solar cells used in the market. Composite materials of TiO_2 and other metal oxides are being developed to reduce charge recombination and improve DSSC efficiency. As a technique for fabricating the photoelectrode thin films, electrophoretic deposition has scarcely been employed in deposition of composite electrode thin films despite being a cost effective method which can readily be scaled up for mass production. The outcome of the study will be useful in producing crystalline, nanoparticulate and nanoporous photoelectrodes suitable for application in the dye-sensitized solar cells. Such modified photoelectrodes could contribute to reduction of recombination of charges, improvement in electron injection and transmission in semiconductors, and enhancement of the conversion efficiency of DSSCs. The uptake of PV cells in the market could increase if these DSSCs are successfully fabricated with high

conversion efficiencies or low production cost or both through use of low cost methods like EPD. The results of this research will contribute extra knowledge in fabrication of dye-sensitized solar cells using low cost film-deposition methods.

Thesis outline

The thesis is divided into six chapters. Following this introduction chapter is the literature review of previous studies on DSSCs and EPD technique. Chapter 2 also discusses the knowledge gap being filled by this work. The theory governing the calculation of numerical results is discussed in Chapter 3. In Chapter 4, there is a presentation of the apparatus, materials and experimental procedures for fabricating TiO_2/Nb_2O_5 composite film. In addition, the chapter presents procedures for characterizing the fabricated DSSC as well as the process of obtaining the results. Chapter 5 presents the analysis and discussion of results. Finally, Chapter 6 summarizes the conclusions drawn from this work and states suggestions for further work.

CHAPTER TWO

LITERATURE REVIEW

2.1 DSSC Structure

A dye-sensitized solar cell (DSSC) comprises a working electrode (dye-sensitized semiconductor film coated on a TCO) and a counter electrode, sandwiching an electrolyte containing a red-ox couple as shown in Figure 2.1.

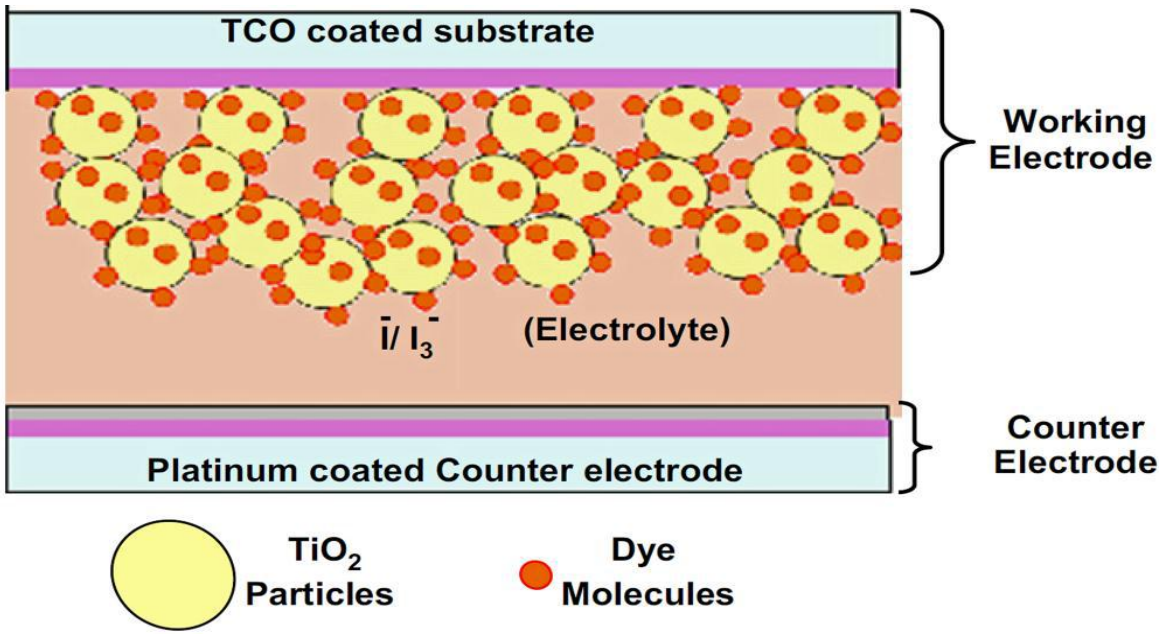

Figure 2.1: Basic structure of a dye-sensitized solar cell (Weerasinghe *et al*., 2013).

The dye-sensitized photoelectrode (also called photoanode) serves as the working electrode and consists of porous, nanocrystalline semiconductor film deposited on a glass substrate coated with a thin film of transparent conducting oxide (TCO). The most common TCO materials coated on glass substrates include fluorine doped tin oxide (FTO) and indium tin oxide (ITO) because of their favourable work function as compared to the semiconductor electrode. The counter electrode consists of glass substrate coated with a TCO layer and further coated with a catalytic material like platinum. The space between the dye-sensitized photoelectrode and the counter electrode is imbued with an electrolyte that includes a red-ox couple. The commonly used red-ox couple is a mixture of iodine and iodide in an organic solvent. The DSSCs resolve the problem in wide band gap semiconductors insensitive to visible light by using a dye to inject the electrons across the wide band gap of the

semiconductor. The light adsorbed by the dye generates electrons which flow through the cell resulting in the production of electricity (O'regan & Gratzel, 1991). Research on DSSC is considered promising due to the dependence of the cell's light-to-electric-energy conversion efficiency on its materials. It is noteworthy that the materials alone are not sufficient to guarantee a highly efficient DSSC, which is also low cost, as its features are intertwined with the photoelectrode film coating methods (Wang *et al*., 2012).

2.2 Techniques for Fabricating DSSC Photoelectrode

A major component of a DSSC is the photoelectrode, whose function is to transmit light and the injected electron to an external circuit. It follows therefore that photoelectrodes should have the properties of high optical transparency and good electrical conductivity (Gratzel, 2005). To realize an improvement in efficiency of DSSCs, researchers must take into account the materials used and the film deposition techniques. Techniques employed in fabrication of photoelectrodes can broadly be categorized into either physical or chemical techniques. The following is a review, including merits and demerits of the various techniques for photoelectrode preparation.

(a) Physical deposition techniques

The physical deposition techniques use mechanical or thermodynamic means to prepare and deposit the materials (Asim *et al*., 2014). Physical methods can be categorized according to phase of their precursors whether liquid or gas. The following is a brief review of various physical deposition techniques used in film preparations.

i) Screen printing

The screen printing technique uses a mesh to transfer a paste onto a substrate by a mechanical squeegee. During printing, the screen with paste is placed onto the surface on which film is deposited (substrate) and a squeegee is made to traverse the substrate under pressure. The screen printing process is detailed in Figure 2.2. This method produces highly reproducible thick films of around 10-15 microns. It is used in electronic industries to produce massive and highly reproducible structures. Yan *et al*., (2012), fabricated DSSCs based on ZnO/TiO_2

composite thin films using screen printing, colloidal spray coating and electrophoretic deposition techniques. Their cells produced conversion efficiency of 1.87%.

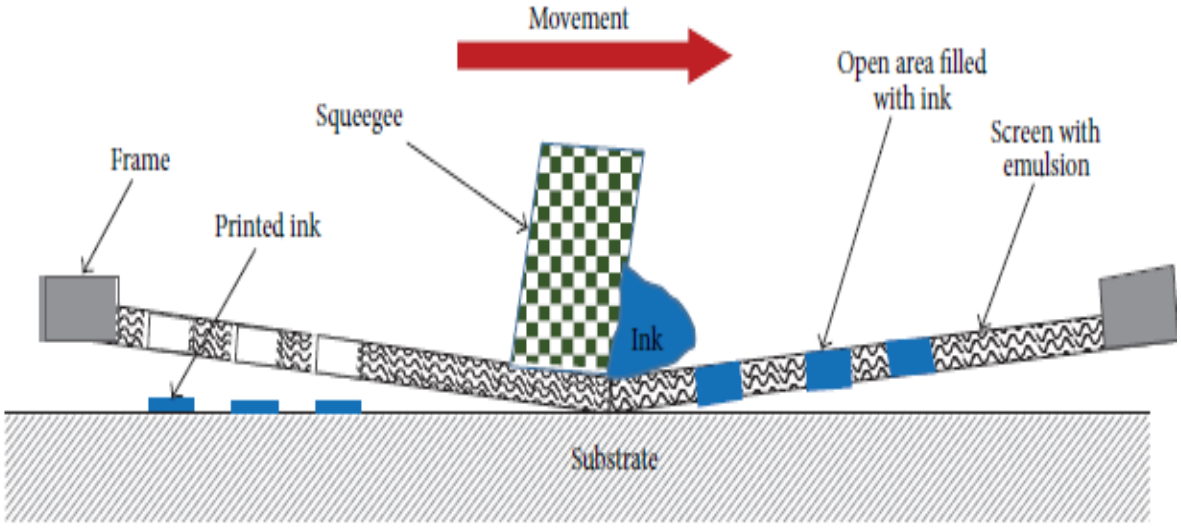

Figure 2.2: Schematic of diagram of screen printing process (Krebs, 2009).

A high efficiency of 9.1% has been obtained for DSSCs fabricated with porous nanocrystalline TiO_2 films (Yan *et al.*, 2012). However, a major limitation of using the screen printing method is that it cannot use water as solvent because of formation of cracks on the film. Water is usually replaced with organic solvents in this technique. Another disadvantage is the use of organic binders which require thermal activation. Furthermore, constituting the right paste composition for application in screen printing is usually a tedious process (Tan *et al*., 2006).

ii) Doctor blade method

The doctor blade technique, also called tape casting or knife coating is a method in which a film is deposited by spreading a paste on to a substrate using a slanted blade. The stages of doctor blade method include paste deposition on glass substrate, paste spreading, and film drying. A fixed amount of paste is put on a substrate and a glass rod rolled over the paste, guided by the spacers to determine film thickness (Padinger *et al*., 2000). Doctor blade method is a relatively cheap approach for metal oxide paste coatings (Ahmadi *et al*., 2013). Some disadvantages of using this technique include wastage of spread out paste, and the extended time required to determine the best coating parameters (Padinger *et al.*, 2000).

iii) Spin coating

Spin coating method uses centrifuge forces to coat a film on a substrate from a suspension placed onto a substrate and rotated at a high speed. Process of spin coating typically includes coating, spin up, spin off, and evaporation. The desired film thickness is determined by the solute concentration in solution, type of solvent, and the continuous rotation of the coated substrate (Hall *et al*., 1998). Jin *et al*., (2012), used spin coating technique to deposit TiO_2 films for application in DSSCs and obtained 1.57% efficiency. Chou *et al*., (2011) also used spin coating processes to deposit TiO_2/NiO composite films on FTO coated glass from a mixture of TiO_2 and NiO powders. The solar cells employing the composite structure yielded a higher conversion efficiency (3.8%) than that of the screen printed TiO_2 film-based dye-sensitized solar cell (3.27%). The improvement in the conversion efficiency was attributed to the blocking effect of the NiO particles. The spin coating technique has the advantage of simple set-up, low power consumption, and produces uniform films. However, the spin-coating technique has the limitation of requiring a substrate with a flat surface of limited size (Ahmadi *et al*., 2013).

iv) Dip coating

The dip coating method consists of immersion and withdrawal processes of the substrate in material solution at a constant speed. The substrate is dipped in material solution and then pulled out which occasion the formation of a thin film deposit on the substrate. The coating thickness is regulated by the speed with which the substrate is pulled: a thicker coating forms if the removal speed is high. The quality of resulting film depends on surface tension, viscous force and force of gravity (Scriven, 1988). A novel DSSC based on dip coated porous TiO_2 films on an FTO substrate produce a cell efficiency of 10.8% (Ito *et al.,* 2008). This technique has the disadvantage of using volatile solvents to evaporate solutions on the coating (Ito *et al.,* 2008).

v) Sputtering

Sputtering involves depositing (metal) on a surface by using fast ions to eject metal particles from a target. In the sputtering technique, incident particles in the form of ions are accelerated by an applied electrical potential. Sputtering has been categorized to DC magnetron sputtering and radio frequency (RF) magnetron sputtering. The RF magnetron

sputtering process is suited for insulating materials as it induces a positive charge on the target surface (Ahmadi *et al*., 2014). Conflicting results have been reported in the literature for DSSCs fabricated using RF magnetron sputtered porous TiO_2 films on FTO substrate. Jin *et al.,* (2012), obtained efficiency of 4.60% whereas Jeong *et al.,* (2011), obtained efficiency too low to be reported. The RF magnetron sputtering has the advantage of allowing direct sputtering of insulators. A possible limitation of this technique is the obstruction of the RF radiation by electromagnetic protecting. Additionally, RF networks demand matching networks and complicated apparatus like power supplies (Awais *et al*., 2011).

DC magnetron sputtering is an older sputter deposition method than the RF sputter. It is used for conductive materials and unsuitable for dielectric metal targets. Typical DC magnetron sputtering equipment operates at an applied potential of between 1,000 and 3,000V, the vacuum pump of 10^{-3} Pa, and pressure of about 10 to 16 Pascal. Waita *et al.,* (2009) used DC magnetron sputtering technique to deposit TiO_2 blocking layers for films applied to DSSCs. An efficiency of 0.78% was obtained for DSSC based on sputter deposited TiO_2 thin films on SnO_2:F coated substrates (Hossain *et al*., 2008). However, Awais *et al*., (2011), used magnetron sputtering to fabricate films for application in DSSCs and obtained cell efficiency too low to be reported. TiO_2/Nb_2O_5 composite films have been fabricated using DC magnetron technique and consequently, the DSSC based on these composite films yielded conversion efficiency of 1.86% (Eguchi *et al*., 2000).

From the reported values of efficiency, sputtering methods appear unsuitable for film deposition to be used in DSSCS. Some of its advantages include good film adhesion on substrate, low levels of contamination, good control of deposition temperature and pressure. The disadvantages of the method include heat generation when plasma electrons bombard the substrates, low deposition rate, and high pressures of working gas (Hossain *et al*., 2008).

(b) Chemical deposition techniques

A chemical deposition techniques typically involves a fluid precursor that experiences a chemical change at a surface of a solid resulting in a solid layer (Choy, 2003).

i) Chemical vapor deposition technique (CVD)

The chemical vapor deposition (CVD) method is the result of chemical reactions that occur between the gaseous reactants close to the surface of a heated substrate. CVD is able to produce dense materials and still allow manipulations at the atomic or nanometer scale. In addition, films deposited by CVD are highly uniform, with good adhesion (Choy, 2003). The method can be used to coat complex-shaped components due to its good throwing power (Choy, 2003). The CVD rate of deposition is readily adjustable to produce epitaxial thin films at low deposition rates and thick protective films at high deposition rates. A DSSC based on nanocrystalline TiO_2 thin films deposited by chemical vapor method yielded an efficiency of 0.17% (Shinde, & Bhosale, 2008). However, the cells based on ZnO/TiO_2 composite films deposited by thermal chemical vapor method produced too low an efficiency to be reported (Kim *et al*., 2007).

The disadvantages of this technique include, chemical and safety hazards caused by use of toxic and corrosive precursor gases. These issues however, have been addressed through use of variants of CVD methods like combustion chemical deposition (CCVD) which employ more environmentally friendly precursors. Another drawback of CVD is the difficulty in depositing multicomponent materials due to different vaporization rates of different precursor. This limitation can be solved by using single-source chemical precursors (Asim *et al*., 2014).

ii) Hydrothermal method

Hydrothermal method is suitable for production of semiconductor nanowires at low temperatures. Hydrothermal method or synthesis involves reactions in aqueous media under 100°C and 1.0 bar pressure conditions (Tacchini *et al.,* 2012). Hydrothermal experiments require that starting materials be of known composition, highly purified and homogeneous (Tacchini *et al.*, 2012). Hydrothermal method, followed by a fast dip coating, has been used by Feng *et al.,* (2012) for preparation of TiO_2/ZnO nanowire arrays. Their DSSC achieved an efficiency of 3.8%. The advantages of hydrothermal method include; ability to induce the materials to solubility through application of heat and pressure. The products of specific phase can be readily produced and compounds of specific condensed state can be synthesized. Hydrothermal method can achieve precise control of the crystallinity of the end product via adjustment of parameters such as surfactants and precursors, and reaction time.

This method also enhances the chemical activities of the reactant. Limitations of hydrothermal method include the safety issues and difficulties of observing the reaction process.

iii) Successive ionic layer adsorption and reaction (SILAR)

This is a method that is based on immersion of a substrate into anionic and cationic precursors, followed by rinsing of the substrate between every immersion in double distilled water in order to circumvent homogeneous precipitation. The cations are adsorbed onto a substrate surface via successive immersion of substrate into a cationic precursor. The process of immersion and rinsing in both cationic and anionic precursors forms a complete cycle. A multilayer film forms on substrate after a few repetitions of these cycles. Das *et al*., (2012), used SILAR and CVD methods to prepare graphene film electrodes for DSSC. Their fabricated solar cell reached an efficiency of 3.4%. Chung *et al*., (2012), deposited thin ZnSe layers on ZnO nanowires using SILAR method for DSSC application. The cells achieved improved efficiency due to the facilitation of electron transfer. In a SILAR technique, the deposition of a sufficiently thick film requires an extended period of time which necessities the use of a microprocessor (Pawar *et al*., 2011).

iv) Spray pyrolysis deposition (SPD)

In spray pyrolysis method, a solution (precursor) is atomized and its small droplets sprayed onto a heated substrate which results in the formation of a dry precipitate and thermal decomposition (Patil, 1999). The technique involves a number of variable parameters that affect quality of deposited film. These parameters include, deposition temperature, flow rate, solute concentration in solution, carrier gases, and deposition time. When TiO_2 blocking layer was coated on a substrate by SPD method, the DSSC achieved efficiency too low to be reported (Jiang *et al*.,2013). On the other hand, Xia *et al*., (2007) recorded an efficiency of 3.35% for DSSC fabricated using Nb_2O_5 blocking layer deposited by spray pyrolysis. Dye-sensitized solar cells using porous TiO_2 films deposited using SPD produced efficiency of 3.2% (Okuya *et al.,* 2002). Unlike SILAR method, spray pyrolysis continuously produces the films and pyrolysis occurs within the created submicron-sized liquid droplets. Spray pyrolysis method does not necessarily require high quality substrates.

v) Sol-gel coating

The Sol-gel coating is a wet technique which results in a pure, homogeneous, and highly adhesive film to the substrate. It is a method widely used in the synthesis of materials originating from a chemical-solution precursor for gel formation. The Sol-gel deposited TiO_2 thin films are highly structured and cauliflower-like at the surface, but at the boundary (interface) with FTO coated glass, they are compact and nonporous (Musembi, 2009). The Sol-gel method was used by Jin *et al.*, 2010, to prepare nanoporous TiO_2 thin films. The resulting DSSC managed to achieve an efficiency of 1.2%. Efficiency of 0.31% has been obtained for DSSCs based on mesoporous nanocrystalline TiO_2 films deposited using hydrolysis-limited Sol-gel process (Fu *et al.*, 2009). Notably, the use of Sol-gel technique results in highly adhesive, homogeneous and pure films and it is a low temperature processing technique.

vi) Electrophoretic deposition (EPD)

In electrophoretic deposition (EPD), charged particles suspended in a solvent are forced to move and deposit on an oppositely charged electrode upon application of electric field. The EPD is fast becoming a promising technique owing to its adaptability, lucidity and cost effectiveness (Besra & Liu, 2007). Electrophoretic deposition differs from electrochemical plating in that particles are deposited from suspension whereas in particles are deposited from solution in the electrochemical plating. In contrast to other physical and chemical techniques which require high temperatures and pressures, Electrophoretic deposition can be conducted under normal conditions of pressures and temperatures (Cabanas-polo & Boccaccini, 2015). The EPD has the limitation of film detachment from the substrate or film crack formation following the evaporation of residual solvent after film deposition. Films non-chemically attached to the substrate and adhesion must be effected through firing. An aspect of EPD explored in this study is the possibility of simultaneously depositing nanoparticles in the desired ratios leading to fabrication of composite films.

2.3 Factors Affecting Efficiency of DSSCs

A dye-sensitized solar cell is affected by factors related to components such as types of dyes, electrolytes, counter electrodes and photoelectrodes. These factors are discussed in the following section.

(a) Types of dyes

The dyes (photosensitizers) absorb sunlight photons and inject electrons to the conduction band (CB) of the wide band gap metal oxide constituting the photoelectrode (O'Regan & Gratzel, 1991). For photosensitization of TiO_2-based DSSCs, Ruthenium polypyridyl dyes have proved to be most efficient due to their broad absorption spectra combined with favorable photo-electrochemical properties and high stability in the oxidized state (Bingwen *et al*, 1997). The most commonly used ruthenium complex dyes in DSSCs include N719 or Ruthenium 535-bisTBA dye whose chemical formula is $(RuL_2(NCS)_2TBA)_2$, where L=2,2'-bipyridine-4,4'-dicarboxylate and N3 (black dye, $RuL_4(NCS)_2$), (Boschloo & Hagfeldt, 2009).

The conversion efficiency of ruthenium dyes based DSSCs is still better than that of cells sensitized with other types of dye compounds like chlorophyll derivatives (Kay & Gratzel, 1993). Ruthenium (Ru) metal dyes have the disadvantage of low molar absorption coefficient in short wavelength regions (about 350 nm - 500 nm). Therefore, efforts have been devoted to synthesize dyes with high molar absorption coefficient in order to improve DSSC efficiency (Boschloo & Hagfeldt, 2009; Qin & Peng, 2011).

(c) Types of electrolyte

The electrolyte in dye-sensitized solar cell (DSSC) transfers electrons from the counter electrode to the oxidized dye thus completing the circuit. Electrolytes for DSSCs are categorized into liquid, solid, and quasi-solid state electrolytes based on their viscosities (ψ). A liquid state electrolyte typically comprises organic solvent, red-ox couple, and additives with the red-ox couple being the major component. The iodide/triiodide (I^-/I_3^-) red-ox couple is obtained when lithium iodide or other iodide compounds like potassium iodide and iodine are dissolved in organic nitrite solvents. The iodide/triiodide red-ox couple has advantages of good solubility in organic solvents, rapid dye regeneration, suitable red-ox potential, and high conversion efficiency (Boschloo & Hagfeldt, 2009). However, the I^-/I_3^- red-ox couple has the limitations of low open circuit voltage (V_{OC}) and corrosion of electrodes. Other types of red-ox couples including (Br^-/Br_3^- (Ferrere *et al.*, 1997), $SCN^-/(SCN)_3^-$ (Oskam *et al*., 2001), and $SeCN^-/(SeCN)_3^-$ (Wang *et al*., 2004) have been

synthesized and investigated for use in DSSCs. The efficiency of DSSCs with iodide/triiodide electrolyte red-ox couple, however, remains unmatched by that of cells based on alternative red-ox couples.

Another component of liquid electrolyte is the organic solvent. It functions to facilitate the dissolution and diffusion of iodine/triiodide ions. Acetonitrile (ACN) and 3-methoxypropionitrile (MePN) have been widely used for DSSC electrolytes because they are low viscosity and low boiling point solvents. Decreasing viscosity of the solvent increases the short circuit current due to better diffusion of the red-ox couple. Acetonitrile is preferred to MePN because of its excellent stability, and capability to dissolve salts (Pugliese, 2014). However, a demerit of using acetonitrile and iodine in liquid electrolytes includes the potential environmentally adverse effects contributed by these chemicals.

Electric additives constitute the other component of liquid electrolyte. They are employed to suppress charge recombination in DSSCs. The most efficient additives are 4-tert-butylpyridine (4TBP) (Kopidakis *et al*., 2006), methylbenzimidazole (MBI) (Figgemeier & Hagfeldt, 2004), and Lithium (Li) cations (Mehmood, 2014). The most probable mechanism is that these additives adsorb on the semiconductor surface and block the reduction sites to keep tri-iodide ions away from contact. The main disadvantages of liquid electrolytes include solvent leakage and corrosion of terminals affecting the long-term stability of the cells. Surlyn^{R} ionomer resin is a sealing material used to reduce liquid electrolyte leakage as well as resist corrosion from iodine. (Snaith & Schmidt-Mende, 2007).

(d) Types of counter electrodes

The counter electrode (CE) comprises a catalyst deposited on a transparent conductive oxide (TCO) to facilitate reduction of excited dye. The preferred catalyst is platinum (Pt) because of its high exchange current density, high catalysis, and transparency (Boschloo & Hagfeldt, 2009). The performance of CE depends on the method of Pt deposition on the TCO coated glass substrate. The deposition methods include thermal decomposition of hexachloroplatinic salt in 2-propanol (Hafez *et al*., 2012), sputtering (Nazeeruddin *et al*., 1993), and spin coating (Lee *et al*., 2001). The deposition method affects the charge-transfer resistances and stability of the counter electrode. It is reported that the activity of the platinum (Pt) catalyst decreases with time in presence of iodide/triiodide red-ox couple due to alteration of its electrocatalytic properties (Mehmood, 2014). Despite showing excellent catalytic action, platinum has the

disadvantage of being an expensive material. Deposition processes require annealing of the film at relatively high temperatures (450 °C) to form a film on FTO. This high temperature treatment of the film limits the application of this method to plastics and other thermally sensitive materials. Graphene, carbon and conductive polymers have been synthesized as alternative catalytic materials to replace platinum based on their high electronic conductivity, and good reactivity for triiodide reduction (Li *et al.*, 2012). However, the DSSCs based on these alternate catalytic materials have been low due to lower catalytic activity for triiodide reduction compared with Platinum.

(d) Photoelectrodes for dye-sensitized solar cells

In 1991, O'Regan and Gratzel developed the first dye-sensitized solar cell based on highly effective porous titanium dioxide (TiO_2) electrodes. TiO_2 is a material that is non-toxic, transparent, abundant-, environmentally stable, chemically resistant and relatively cheap (Gratzel, 2005). TiO_2 has extensively been used, in conjunction with ruthenium dye complex, as a photoelectrode for the fabrication of DSSCs because of its overall high conversion efficiency. Titanium dioxide is a semi-conducting oxide that has three crystalline polymorphs, namely anatase (E_g = 3.23 eV), rutile (E_g = 3.05 eV), and brookite (E_g = 3.26 eV) (Nowotny *et al.*, 2008). The Fermi level of rutile is 0.1 eV lower than that of the anatase, making anatase preferable in DSSCs applications. However, the application of TiO_2 in DSSCs is hindered by recombination of the photo-generated electrons with the red-ox couple in electrolyte limiting the conversion efficiency.

Other metal oxides have been examined as photoelectrodes for DSSCs application and their films fabricated by variety of deposition techniques. They include ZnO (Chiu *et al.*, 2011), Nb_2O_5, (Rani *et al*., 2014), Al_2O_3 (Quedraogo & Savadogo, 2013), and CeO_2 (Jose *et al.*, 2009). Although the DSSCs based on individual performances of these semiconductors are not so efficient, some of their combinations have shown promising results. Consequently, composites such as MgO/TiO_2, (Wu *et al*., 2008), SnO_2/CeO_2 (Ito *et al.*, 2008), ZnO/SnO_2 (Chen *et al*., 2009; Pan *et al*., 2012), ZnO/TiO_2 (Yan *et al.*, 2012), ZnO/ZnS (Rouhi *et al.*, 2015), and ZrO_2/TiO_2 (Wang *et al.*, 2012), have been explored for application as photoelectrodes. However, the conversion efficiencies of solar cells fabricated from these materials are much less ($\eta < 6\%$) than those of TiO_2 based solar cells which presently stand at $\eta = 11.8\%$ (Yella e*t al.*, 2011). Solar cells from composites of TiO_2/other metal oxides

showed relatively higher efficiencies. Niobium (V) oxide and titanium (iv) oxide (Nb_2O_5/TiO_2) composite electrode films will be investigated in this study. Niobium (V) oxide (Nb_2O_5) is a semiconductor with a wide band gap energy(E_g) of 3.49 eV (Jose *et al.*, 2009), which is larger than E_g of TiO_2 by 0.29 eV (Sancho-Parramon *et al.*, 2008). Nb_2O_5 based photoelectrodes in DSSCs, sensitized with N3 dye produced higher V_{OC} than TiO_2 based photoelectrodes in DSSCs. The higher V_{OC} for Nb_2O_5 based cells was attributed to its higher conduction band edge compared with TiO_2 and larger optical band gap (Hara *et al.*, 2000). In this study, photoelectrodes formed through a mixed particle structure are expected to incorporate an alteration in CB edge in composites of TiO_2 and Nb_2O_5 thus yielding high V_{OC} for DSSCs.

2.4 Electrophoretic Deposition (EPD) and Factors Affecting Film Deposition

As mentioned earlier, electrophoretic deposition (EPD) is a colloidal method in which an applied DC electric field force charged particles suspended in a solvent to move and deposit on an oppositely charged electrode resulting in formation of a condensed film as shown in the following Figure 2.3.

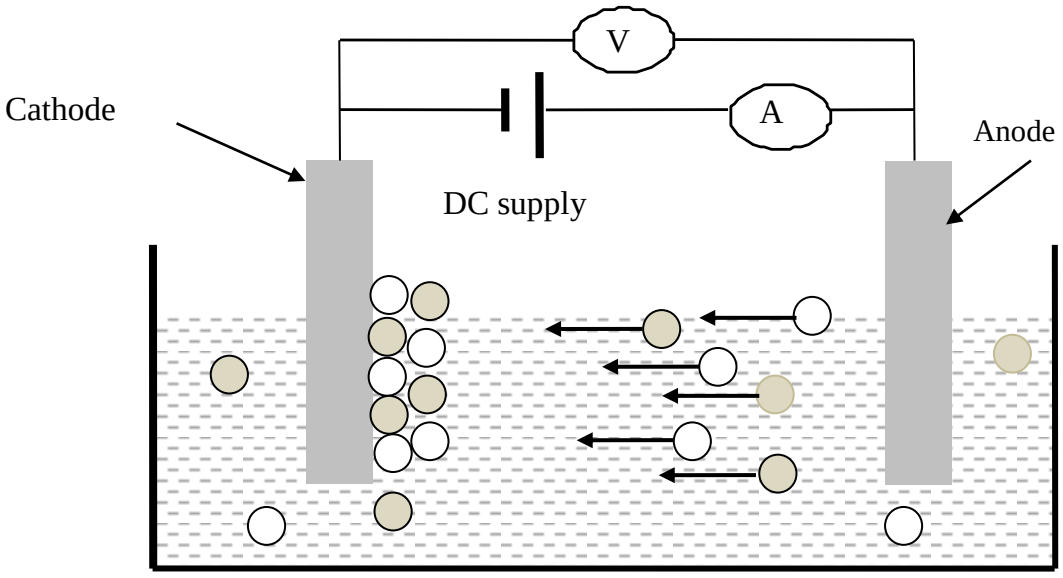

Figure 2.3: Schematic drawing of the EPD setup showing cathodic deposition of charged particles of mixed metal oxides.(Dickerson & Boccaccini, 2012).

The EPD technique has been studied since 1807 when Ruess first observed that solid particles (clay) suspended in water moved upon application of an electric field (Sarkar & Nicholson, 1996). Hamaker was the first scientist to study and apply EPD to ceramics (Hamaker, 1940). The kinetics of EPD is not yet well understood and scientists continue to investigate the process as they seek to develop a quantitative understanding of its kinetics and thus enable its application in material processing (Dickerson & Boccaccini, 2012). The EPD technique has the advantage of simple equipment, rapid coating production, high reproducibility, adaptability to mass production processing, and low cost of film fabrication (Boccaccini, *et al*., 2010). Compared to other film forming techniques like screen printing and doctor blade, EPD process offers ease in controlling the morphology and thickness of a deposited film by simple alteration of the particle concentration in suspension, deposition time, and applied electric voltage. Unlike electrochemical plating in which deposition is from a solution, electrophoretic deposition uses charged particles (metal oxides) in suspension.

The characteristics of electrophoretically deposited films may be controlled by EPD conditions and parameters, including the nature and choice of solvent, charging mechanism, particle concentration in suspension, electric field strength, and deposition times (Dickerson & Boccaccini, 2012). Various authors have applied different combinations of these EPD conditions to deposit TiO_2 -based nanostructured films (Table 2.1). Following is a brief review of the EPD processing conditions/parameters.

(a) Particle charging mechanism

The electrophoretic deposition process is governed by the particles ability to develop electric charges when suspended in a liquid. Iodine, Zinc nitrate $Zn(NO_3)_2$ and Magnesium nitrate hexahydrate ($Mg(NO_3)_2.6H_2O$, and have been used as additives in previous studies to constitute charging mechanisms of single or many nanoparticles systems as shown in Table 2.1. Particle charging of nanoparticles using $Mg(NO_3)_2.6H_2O$ is achieved by adsorption of $MgNO_3^+$ to the particle surface (Yum *et al.,* 2005). It is believed that in the case of iodine additive, the particle charging mechanism is achieved through adsorption of protons (Benehkohal, 2013).

Table 2.1: Summary of electrophoretically deposited TiO_2 based films applied to dye-sensitized solar cells.

Nano-structure	Substrate	Solvent	Additive	EPD parameters	Efficiency (%)	Reference
TiO_2 layers	ITO-PET	_	_	d=0.3 mm, DCV=6 V, t=0.5-1 min.	4.30	Miyasaka & Kijitori (2004)
TiO_2 nP	ITO-PET	2-propanol	$Mg(NO_3)_2$.$6H_2O$	d=2 cm, c=2.5 g/L, DCV=20-160 V, t=180 s.	1.03	Yum *et al*., (2005)
TiO_2 nT	FTO	Methanol & water	__	__	6.72	Kim *et al*., 2007
TiO_2 nP	FTO			d=1 cm, c=10 g/L, DCV=5-20 V t=1-8 min	__	Jarernboon *et al*., (2009)
TiO_2 nP	FTO	2-propanol	$Mg(NO_3)_2$.$6H_2O$	d=2 cm, c=2.5 g/L, DCV= 20-60 V, t=15 min.	4.91	Bandy *et al.,* (2011)
TiO_2/ZnO	ITO-PEN	2-propanol	_	d=1.5 cm, c=2.5 g/L, *I*=20 μA/cm^2, t=5 min.	5.54	Chiu *et al*., (2011)
TiO_2	Flexible-glass		$Mg(NO_3)_2$.$6H_2O$	d=2 cm c=0.25 g/L DCV=75 V t=3 min	__	Lee *et al*., (2011)
ZnO/TiO_2 comp	FTO	Ethanol & water	_	d=1.5 cm, c=1.33 g/L, DCV=60 V.	0.10	Yan *et al*., (2012)
TiO_2 nP	FTO & PEN-ITO	Ethanol/2-propanol/ Butanol	I_2	d=7 mm, c=33.3 g/L, DCV=30 V	5.20	Xue *et al*., (2012)
TiO_2/ZnO comp	FTO& stainless steel	Water & 2-propanol	$Zn(NO_3)_2$	d=2 cm, c=5 g/L, DCV=3.1 V, t=5-15 min.	5.57	Benehkohal, (2013)

KEY: nP nanoparticles, nT nanotube, nR nanorods, comp composites, d electrodes separation, *c* particle concentration, DCV applied (DC) voltage, *I* current, and *t* deposition time.

(b) **Particle concentration in suspension**

The particle concentration in electrophoretic deposition (EPD) suspensions constitutes another important parameter in electrophoretic deposition process with values as low as 0.25 g/L up to 33.3 g/L reported in the literature (Table 2.1). According to Hamaker's Equation (2.1), the deposit mass (thickness) increases exponentially with particle concentration in suspension. This finding has been confirmed in practice as reported by Ata *et al*., (2014) among other authors (Figure 2.4). It can be seen from the Figure 2.4, that deposition rate was high for concentrations lower than 0.1 g/L and no significant variation in deposit mass was observed at higher concentrations. Radice *et al*., (2010), however, noticed that no deposit was formed in some systems below a particular particle concentration independent of applied voltage or deposition time. Indeed, Ata *et al.*, (2014), could not obtain film deposition below a concentration of 0.05 g/L. Since a wide range of values for particle concentrations has been reported, it was difficult to determine the optimum value of particle concentration in suspension to enable deposition of composite films suitable for intended applications by EPD the method.

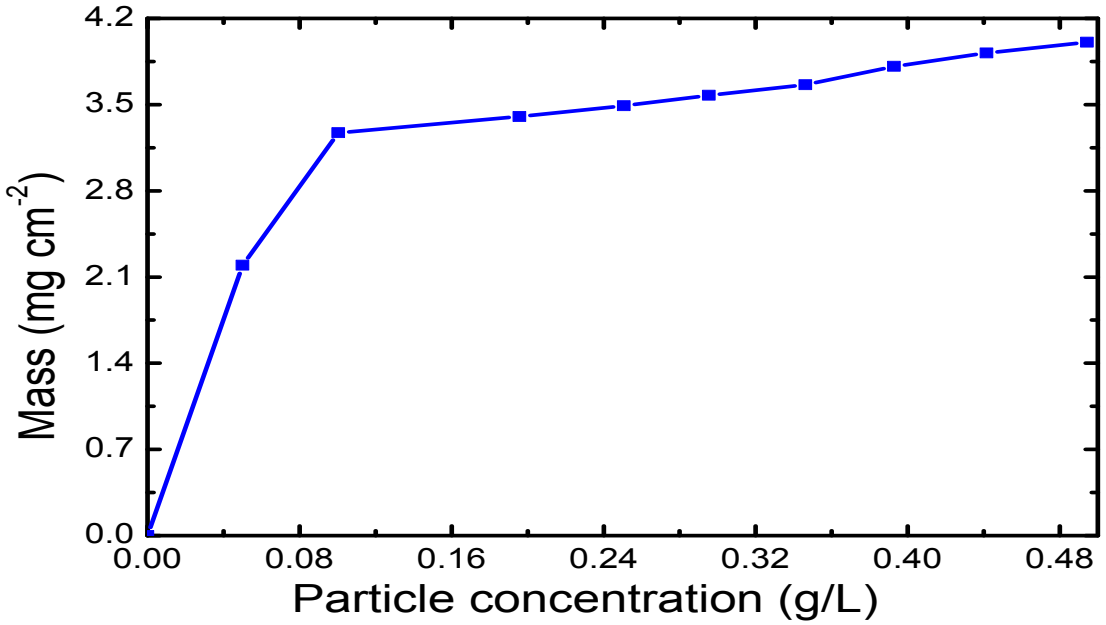

Figure 2.4: Typical deposit mass versus particle concentration for films prepared from 10 g/L TiO_2 suspension in ethanol for deposition time of 5 min and applied voltage of 40V, and (Ata *et al*., 2014).

(c) Electric field strength

Typical configuration of electrophoretic deposition technique involves parallel arrangement of electrodes. The electrode separation distance (l) is usually fixed to provide constant and uniform electric field strength $\left(V/l\right)$ for film deposition. As an EPD process parameter, electric field strength leads to a linear increase in deposition mass according to Hamaker's equation (Besra & Liu, 2007);

$$m = \frac{2}{3} \cdot c \cdot \varsigma_0 \cdot \varsigma_r \cdot \xi \left(\frac{1}{\psi}\right)\left(\frac{V}{b}\right) \cdot t \qquad (2.1)$$

where m is the deposited mass, c is powder/particle concentration in the suspension, ς_0 is permittivity of free space, ς_r is relative permittivity of the solvent, ξ is the zeta potential of the particles, ψ is the viscosity of the solvent, V is the applied DC voltage, b is the distance between the electrodes, and t is the deposition time. Electric fields in range 10 V/m to 50 V/m have been applied in EPD technique as shown in Table 2.1.

Low fields (around 20 V/m) result in good film assembly Basu *et al.,* (2001). However, Konig *et al.,* (2008) observed that suspensions in organic liquids generally require high fields (> 100 V/m) due to their low dielectric constants. In many EPD applications, applied voltage (V) values for fixed electrode separation distances are frequently used rather than electric fields values (V/m). The setback of using high voltages, however, is the film quality deterioration. Moderate applied DC voltages (25 – 60 V) may provide uniform films for DSSC application.

Electrophoretic deposition techniques can be conducted either under constant voltage or constant current while, in either case, keeping the particle concentration in suspension either constant or changing with deposition time. Although constant-current depositions can provide better and easier control over the EPD process for thick films, constant-voltage conditions are ideal for thin films and allow for uniform microstructures (Nyongesa *et al.,* 2007). The challenge is in optimization of the applied electric potential to fabricate films suitable for the intended applications.

(d) Nature of the solvent

The first EPD process used water as the solvent (Hamaker, 1940). The use of water as a solvent has many advantages including, its environmentally friendly nature, low cost, wide availability, ability to control higher temperature during the deposition, and faster EPD kinetics due to high dielectric constant (Dickerson & Boccaccini, 2012). However, high electric fields cause electrolysis of water, adversely affecting the quality of the deposits formed (Besra & Liu, 2007). Other liquid solvents like 2-propanol (Yum *et al*., 2005; Bandy *et al.*, 2011; Chiu *et al*., 2011), and mixtures of water and organic liquids like methanol & water (Kim *et al*, 2007), ethanol & water (Yan *et al*., 2012), and water & 2-propanol (Benehkohal, 2013) have been explored as alternatives to use of water in EPD (Table 2.1). Organic solvents are only little affected by relatively large values of electric field as their use results in little or no electrolysis (Besra & Liu, 2007). The choice of liquid solvent used in EPD is influenced by values of viscosity and relative dielectric constants of solvents suitable for type of film application (Table 2.2.).

Table 2.2: Physical properties of solvents (Dean, 1999).

Solvent	Viscosity [ψ] cP(=10^{-3}Ns/m^2)	Dielectric constant (ε) at 20°C
Methanol	0.557	32.63
Ethanol	1.089	24.55
1-Propanol	1.937	20.13
2-propanol	2.857	18.30
2-butanol	2.588	17.26
Acetonitrile	1.090	37.50
Water	0.890	80.10

Besra & Liu, (2007), used these organic solvents to determine the incidence of deposition for beta-alumina suspensions as function of dielectric constant (ε) of liquid. They obtained film deposition for liquids with dielectric constants in the range of 12-25. Deposition failed for EPD of films from solvents of too low (< 12) dielectric constant (ε) because of insufficient dissociative power. Deposition also failed for electrophoretically deposited films from solvents with too high (> 25) dielectric constant due to the high ionic concentration in the

solvent which contributed to reduction of electrophoretic mobility of charged particles (Miyasaka & Kijitori, 2004). According to the Derjaguin-Landau-Verwey-Overbeek (DLVO) theory, it is noted that that for particle concentrations above a crucial value, the repulsive forces were overcome by the attractive Van der Waals forces resulting in coagulation. (Dickerson & Boccaccini, 2012). The best solvents for EPD suspension are characterized by low viscosity values and high deposition rate (Benehkohal, 2013). 2-propanol, despite having relatively higher viscosity than other solvents, has low relative dielectric constant (18.30) and becomes a favorable candidate solvent for electrophoretic deposition of composite films.

(e) Deposition time

The film deposition rate for a constant applied electric field and constant particle concentration in the EPD process is known to decrease with increased deposition time (Besra & Liu, 2007). A typical variation of deposit mass (approximated by film thickness) with deposition time is shown in Figure 2.5 (Nuryadi & Aprilia, 2012). Initially, the thickness increases nearly linearly and attains a plateau at higher deposition times. For EPD at constant voltage and fixed distance, the plateau results from decrease in EPD electric field possibly due to creation of a non-conducting film deposited on the surface of the electrode. The results are consistent with theoretical predictions based on Hamaker's equation (2.1). Jarernboon *et al*. (2009) approximated the optimum TiO_2 film thickness to $z \sim 14\mu m$ for the highest DSSC efficiency. Films of such thickness are highly porous and therefore very favorable for application in DSSCs where there is increased dye loading. Films of thickness larger than $14\mu m$ result in deterioration of film adhesion to the substrate. Our literature review however established that the efficiency obtained by Jarernboon *et al*., (2009), was too low to be reported.

An optimized-photoelectrode film thickness (z) is required to address the conflict between light harvesting and charge transport and thus enhance conversion efficiency. Electrophoretic deposition (EPD) technique is explored as alternative technique to deposition techniques to overcome the challenge of film thickness control, a factor affecting efficiency of resulting solar cell (Vilarinho *et al*., 2013).

From the literature, we have seen that various techniques can be used to fabricate DSSCs. Although screen printing method is good, it is limited in its inability to use water as solvent because of crack formation in deposited films upon firing. Other limitations of spin coating

process include the low efficiencies and requirements for a substrate with a flat surface of limited size.

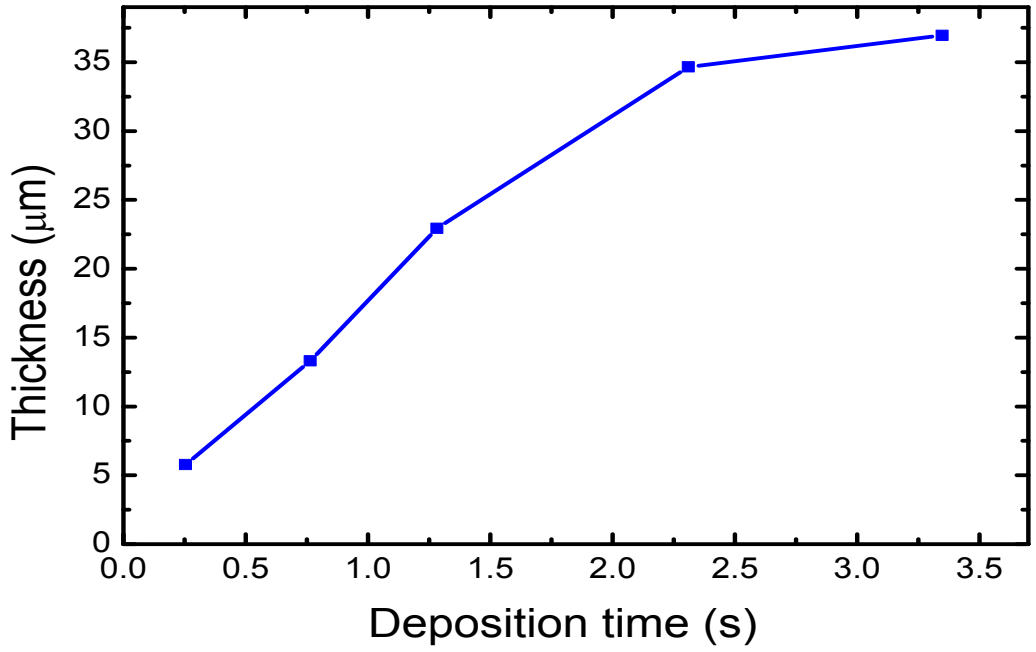

Figure 2.5: Typical TiO_2 thickness versus deposition time of BNT electrophoresis for acetone with iodine –based suspension (Vilarinho *et al*., 2013)

Although dip coated films used in DSSC produce high efficiency (10.8%), the technique has disadvantage of using volatile solvents to evaporate solutions on the coating surfaces (Ito *et al.*, 2008). Electrophoretic deposition technique has been widely explored due to its advantage including, simple equipment, high reproducibility, rapid coating production, and low cost of film fabrication. It also offers an easy manipulation of the morphology and thickness of a deposited film via simple control of the process parameters. Moreover, electrophoretic deposition can be achieved at standard temperature and pressure. Although it produces films of low efficiency, in this work, we wish to explore the use of EPD for the fabrication mixed-particle composites of TiO_2 and Nb_2O_5 for application in dye-sensitized solar cells.

2.5 Electrochemical Impedance Spectroscopy Characterization of DSSC

Electrochemical impedance spectroscopy (EIS) is an important tool for examining the qualities and properties of dye-sensitized solar cells. It enables separation of interfacial capacitances, electron-transfer resistances, charge and ions diffusion components in the film and electrolyte respectively. Before the advent of DSSC, EIS was largely put to use in photoelectrochemistry (Bisquert, 2002). Photoelectrochemistry is a field investigated using electrodes comprising monocrystalline semiconductors for light to electric energy conversion (Bisquert, 2002). In these systems, EIS supply information on the rates of charge transfer at the interface as well as on the concentration of electrons at the surface (Bisquert & Fabregat-Santiago, 2010). Impedance replaces resistance as a more general circuit parameter. In dye-sensitized solar cells, the transport of electrons through TiO_2 film by diffusion is coupled with recombination at the TiO_2/electrolyte boundary. The impedance of electronic diffusion and recombination at the photoelectrode/electrolyte interface in a DSSCs has been widely studied (Bisquert, 2002; Adachi *et al*., 2006; Fabregat-Santiago *et al*., 2007).

A key concept in the DSSC analysis is the chemical capacitance which is normally absent in classical photo-electrochemistry but is critical in the analysis of techniques requiring frequency-resolution in dye-sensitized solar cells (Bisquert & Fabregat-Santiago, 2010). Analysis of EIS measurements often involve use of Nyquist plot whose limitations include the inexplicit frequency presentation on the plot and small impedances being swamped by large impedances. Operation of conventional solar cells has been well explained using equivalent circuits. Han *et al.*, (2004), investigated internal resistances of DSSC using EIS measurements and observed that resistance elements associated with charge transport at the dye/TiO_2/electrolyte interface displayed diode-like behaviour.

A typical electrochemical impedance spectrum for a high performing DSSC displays three arcs in the Nyquist plot: two small ones on both sides of a large central arc (Figure 2.6). The arc on the left, for impedances measured at high frequencies, relates to the charge transfer process at the Platinum coated counter electrode (R_{CE}) while the arc on the right (for impedances at low frequencies) can be attributed to Warburg resistances (Z_d) in Nernst diffusion process of I_3^- ions in the electrolyte. The central arc (in intermediate-frequency region) corresponds to charge transport resistance in TiO_2 film (R_t), charge transfer (recombination) at the TiO_2/dye/electrolyte interfaces (R_{ct}) and the chemical capacitance (C_μ).

Figure (2.6b), shows the characteristic frequencies inserted in the graph in the order of increasing frequency whereby, ω_d corresponding to diffusion of red-ox ions in electrolyte, ω_r to electron recombination with red-ox species, ω_t to electron diffusion in TiO_2, and ω_{CE} to charge transfer at pt/electrolyte interface (Sarker *et al.*, 2014).

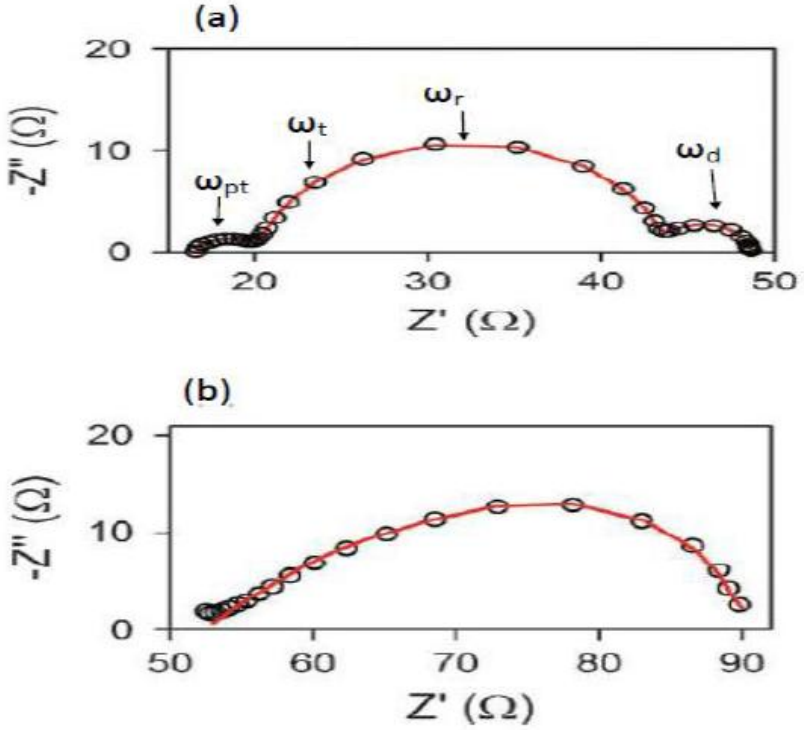

Figure 2.6: Typical experimental impedance spectra for DSSC with an ionic liquid based electrolyte (a) at open circuit conditions 0.6 V, (b) the Gerischer impedance spectra whereby recombination resistance is less than transport resistance (Fabregat-Santiago *et al.*, 2011; Sarker *et al*., 2014).

The EIS spectra of DSSCs do not always show three distinct arcs in the Nyquist plot as evidenced by Nyquist plots exhibiting only the central arc correspond to Gerischer impedance (Figure 2.6c). In such a case, the experimental data must be properly inspected to assist efficient extraction of the physical parameters of the cell. Physical parameters of a solar cell can be derived from cell EIS spectra by fitting the spectra to an equivalent electric model. Several researchers (Bisquert *et al.*, 2000; Fabregat-Santiago *et al*., 2005; Wang *et al*., 2005) have developed equivalent circuits' models to characterize DSSCs. The most widely used equivalent circuit model on DSSCs is the transmission line model due to its accuracy in modeling the cells physical properties (Sarker *et al*., 2014).

CHAPTER THREE

THEORETICAL FRAMEWORK

This chapter gives theories relating to the working of a DSSC, EPD deposition technique, EIS and characterization of films and cells.

3.1 The Working Principle of a Dye-Sensitized Solar Cell (DSSC)

The working principle of a dye-sensitized solar cell (DSSC) is depicted schematically in Figure 3.1. A dye-sensitized solar cell is a photo-electrochemical system, in which a porous, nanocrystalline semiconducting metal-oxide film sensitized with dye molecules and deposited on a transparent conductive glass substrate (such as FTO), serves as a photoelectrode or working electrode (Zhang & Cao, 2011). A counter electrode comprises a catalyst (usually platinum) coated on conducting glass plate.

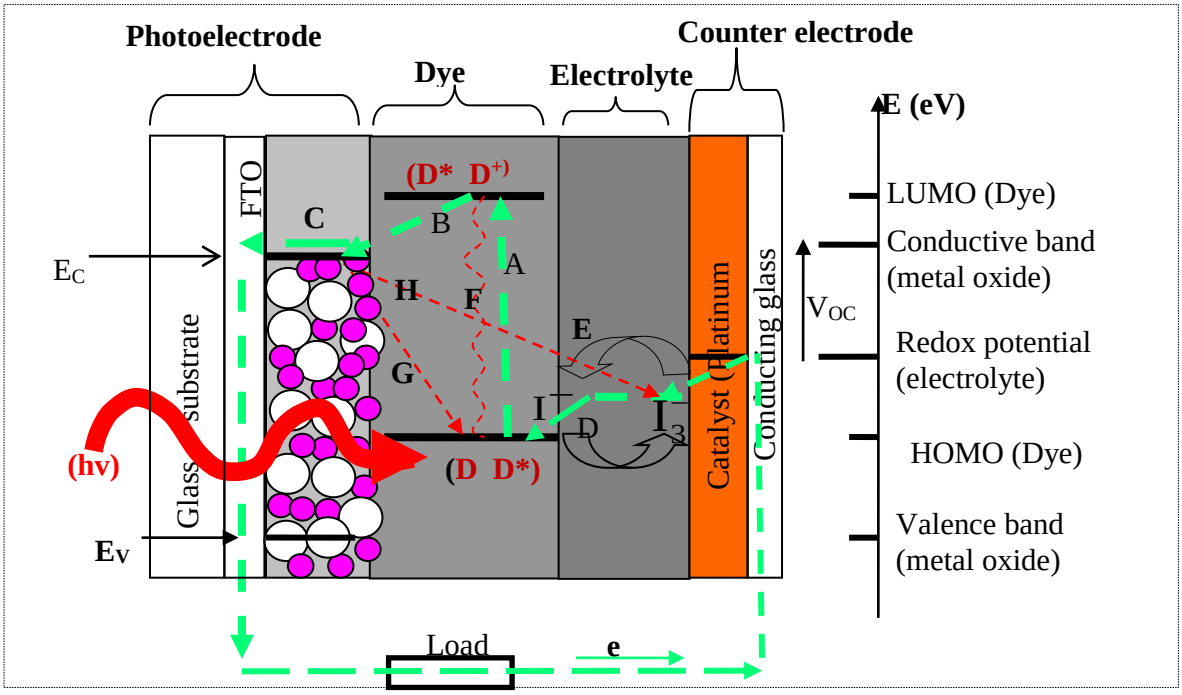

Figure 3.1: Schematic diagram of the working principle of a dye sensitized solar cell. Each component in the DSSC is represented by an isolated block while each electron transfer process is represented by a letter. The vertical line on the right indicates the energy scale in eV and the energies of each functional material are represented by horizontal lines (Luo *et al*., 2009).

The space between the two electrodes is usually filled with a liquid (or solid) electrolyte containing red-ox couples such as I^-/I_3^-, and serves as an electric conductor between the two electrodes. In Figure 3.2, the different electron transfer processes are represented by letters A to G. The light adsorbed by the dye produces electrons which flow through the cell resulting in the generation of electricity (O'regan & Gratzel, 1991).

According to Gratzel (2005), the change of solar energy into electric energy using a solar cell is the result of the dynamic competition between the forward processes (A-E) and back processes (F-H) as indicated in Figure 3.2.

Process A: Photon absorption and dye excitation. The dye molecules adsorbed on the semiconductor film absorb light photons incident on the solar cell. A photon of energy *hv* is absorbed by the dye in the ground state (D) and which promotes it to an excited state (D^*) according to equation (3.1).

$$D + h\upsilon \rightarrow D^* \qquad (3.1)$$

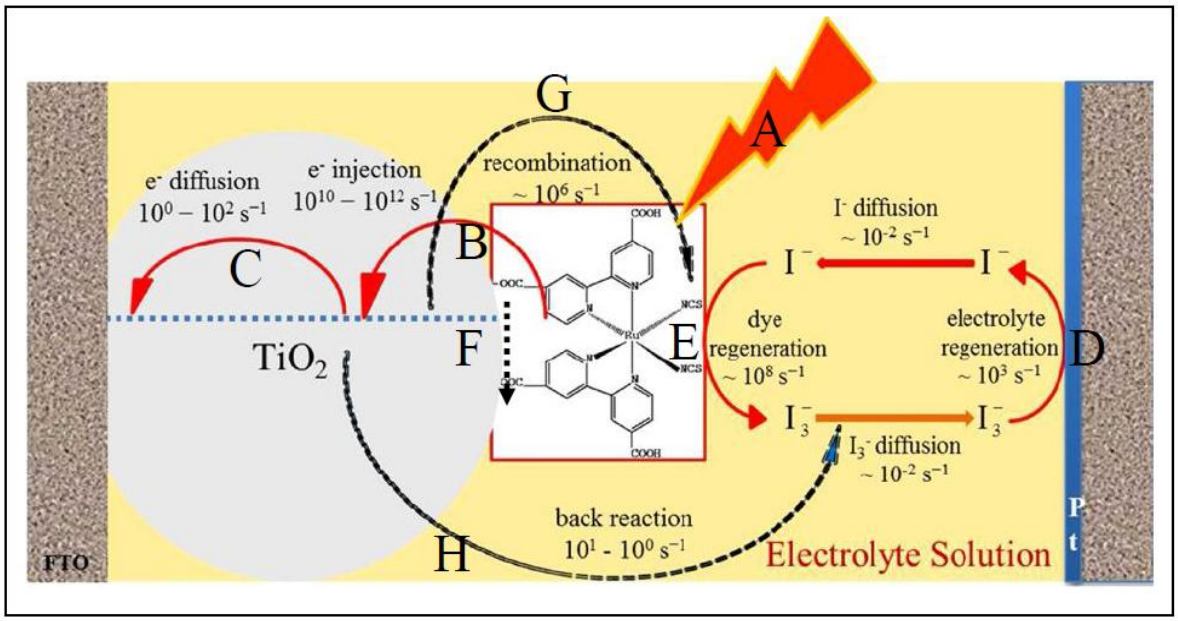

Figure 3.2: The charge transfer kinetics and associated timescales (rates) in DSSC The letters **A**, **B**, **C**, **D**,& **E** represent forward and desired processes while letters **F**, **G** & **H** represent recombination processes (back reactions) in the cell. (Rahman *et al*., 2015)**.**

Process B: Electron injection. The excited dye (D^*) injects electrons (e^-) into the conduction band (CB) of the semiconductor film and becomes oxidized (D^+). The time rate of occurrence of this process is on 10^{10} - 10^{12} s^{-1} scale.

$$D^* \rightarrow D^+ + e^- \quad (3.2)$$

Process C: Electron transport. The injected electrons are transported by diffusion along the semiconductor particulate network towards the external conducting FTO coated glass, via the external load to the platinum-coated FTO counter electrode. Transport of injected electrons occurs by diffusion rather than drift due to negligible field across the semiconductor film. Electron diffusion in film takes place in order of 10^0-10^2 s^{-1} time scale (Figure 3.2).

Process D: Reduction of the red-ox couple at platinum electrode. Finally, the injected electrons reduce triiodide (I_3^-) ions to iodide ($3I^-$) ions according to

$$I_3^- + 2e^-(pt) \rightarrow 3I^- \quad (3.3)$$

This process is in order of 10^3 S^{-1} scale (Rahman *et al*., 2015).

Process E: Regeneration reaction of dye in red-ox couple. After electron injection into semiconductor by the dye, a positively charged (oxidized) dye remains. This oxidized dye (D^+) is reduced to ground state by a red-ox couple in the electrolyte. The highest regeneration efficiency has been achieved by iodide/triiodide (I^-/I_3^-) red-ox species. The equation for reduction of oxidized dye is given by equation 3.4;

$$D^+ + 3I^- \rightarrow D + 2e^- \quad (3.4)$$

This regeneration process is in the order of 10^8 s^{-1}.

The processes **A** to **E** are forward and desirable processes. However, there exist some back reactions (recombination) denoted by processes **F** to **H** as outlined in following section which are not desirable.

Electron Recombination Processes.

Process F: Decay of the excited dye to the ground state,

$$D^* \rightarrow D \qquad (3.5)$$

As shown in Figure 3.2, recombination by dye decaying to the ground state is limited because it takes place in the nano second range which is slower than the electron injection happening in the picoseconds range.

Process G: Recombination of oxidized dye with the injected electrons,

$$D^* + e^- \rightarrow D \qquad (3.6)$$

The process takes place in order of $10^6 s^{-1}$. This process contributes to reduction of electron density in the TiO_2 leading to a change in the energy of the TiO_2 conduction band, thus directly affecting the V_{OC} (Maluta, 2010).

Process H: Capture of injected electrons by the tri-iodide in the electrolyte. As electrons diffuse through the TiO_2 (metal oxide) film, some electrons may become trapped at the surface of the TiO_2 particles and recombine with I_3^- ions in electrolyte. This back reaction (recombination process) is represented by equation (3.7) which resembles equation 3.3 for reduction of red-ox couple at counter electrode;

$$2e^- + I_3^- \rightarrow 3I^- \qquad (3.7)$$

Some of portions of FTO coated glass surface will inevitably get uncovered by the film thus necessitating the electrolyte to reach it thereby causing electron leakage. The recombination takes place at 10^1 to 10^0 s^{-1}.

Electron transport

The electron transport mechanism in a DSSC is related to the matching of energy levels between the CB of the semiconductor and the excited state of the dye. The semiconductor nanoparticle network serves as a transporter of the electrons injected by the dye molecules.

Electrons do not drift through the film but instead diffuse through it. The drift of electrons through the film is out ruled because of the small size of the nanoparticles forming the film which inhibits the creation of a built-in electric field and a space charge layer inside the particles (Pugliese, 2014). There exists sub-band gap states in the semiconductor film that influence the electron transport. Electrons diffuse through the film characterized by a de-trapping of electrons from these sub-band gap states (Hagfeldt & Gratzel, 2000). The electron diffusion is caused by non-uniformity or gradient in electron concentration generated by the collection of the electrons in the conduction band of the semiconductor particles under light irradiation.

The traps characterizing the electron diffusion are localized energy states within band gap and just below the conduction band margin of the metal oxide. The quasi-Fermi level rises in a cell exposed to a high illumination and the number of traps increases resulting in a high photocurrent. If the cell is exposed to low illumination, a low photocurrent is obtained since contribution to electron transport is only by the deep traps. (Hagfeldt & Gratzel, 2000). Three important parameters in the electron transport process include electron diffusion length (L_d), electron lifetime (τ_n) and diffusion coefficient (D_n). Electron diffusion length (L_d) is defined by the average distance the electron travels through the semiconductor before recombination. Electron lifetime (τ_n) is the period from electron generation until recombination or extraction. The diffusion process can be expressed in terms of diffusion coefficient (D_n). The electron diffusion length (L_d) is determined by taking the square root of the product of the effective diffusion coefficient (D_n) and lifetime (τ_n) as given in the following equation (Wang *et al*., 2004);

$$L_d = \sqrt{D_n \tau_n} \tag{3.8}$$

The electron diffusion length in DSSCs can be measured by incident photon conversion efficiency (IPCE) or electrochemical impedance spectroscopy (EIS) methods (Jennings *et al*., 2010; Maluta, 2010). In case electron diffusion length (L_d) is equal to or greater than the film thickness ($L_d \geq z$), all the photogenerated electrons will be statistically collected, raising the current density and efficiency of the cell (Pugliese, 2014). In terms of time, a good solar-cell performance must meet the condition that the electron extraction or transport time should be

shorter than the electron lifetime ($\tau_t \leq \tau_n$) to enable the electrons to reach the front electrode before recombination. Intensive research efforts have been focused on how to enhance forward processes (A-D) and suppress the back reaction or charge recombination in process (D-G) and thereby increasing the conversion efficiency(η).

3.2 Solar Radiation and Materials for Solar Cells

The efficiency of a solar cell is controlled by the variations of the intensity of spectral irradiance of the incident light. The solar radiation impinging the Earth surface depends on factors such as location, atmospheric conditions, and time of the day. Consequently, a power density and standard spectrum have been defined to provide for an accurate cell I-V characterizations as well as comparison among different solar cells. Figure 3.3 shows two curves for comparison: a zigzag one for the sun's radiations received on the earth and a continuous curve for black body at a temperature of around 6000 K. The solar spectrum is similar in shape to that of black body and is influenced by adsorption of some molecules such as ozone gas and water in the atmosphere (Figure 3.3). The optical path through which the solar radiation passes through before reaching the ground depends on the Sun's position and is called Air Mass (AM). The standard air mass used for solar cell testing is AM 1.5G where G stands for Global which is the sum of direct and diffuse light (Weeranghe *et al*., 2013).

The solar cell efficiency also depends on the structure and morphology of photoelectrodes of the DSSC because these properties affect the optical and electronic properties of the photoanode. Porous nanostructures making the photoelectrodes present a larger surface area for adsorption of the dye leading to an enhanced light absorption from a substantial part of the solar spectrum. Materials with wide optical band gaps display a poor reaction to light in the visible region ($0.4 < \lambda < 0.7$ μm, Figure 3.3). This challenge is overcome by coating them with dyes to extend their optical absorption into the visible light region. Titanium dioxide (TiO_2) (E_g = 3.23 eV) (Jose *et al*, 2009) and Niobium (v) oxide (Nb_2O_5) (E_g = 3.49 eV) (Sancho-Parramon, *et al.,* 2008) are wide-band gap materials and only about 8% of light photons (E = 1.77 - 3.2 eV) are capable of promoting electrons from the valence band to the conduction band of TiO_2 or Nb_2O_5. The wide-band gap materials are chemisorbed with dye molecules to enable them to function as solar cell materials. A key requirement of solar cell

materials is the ability to allow radiation in the visible light region (shown by parallel dashed lines in Figure 3.3) to go through them and excite the dye.

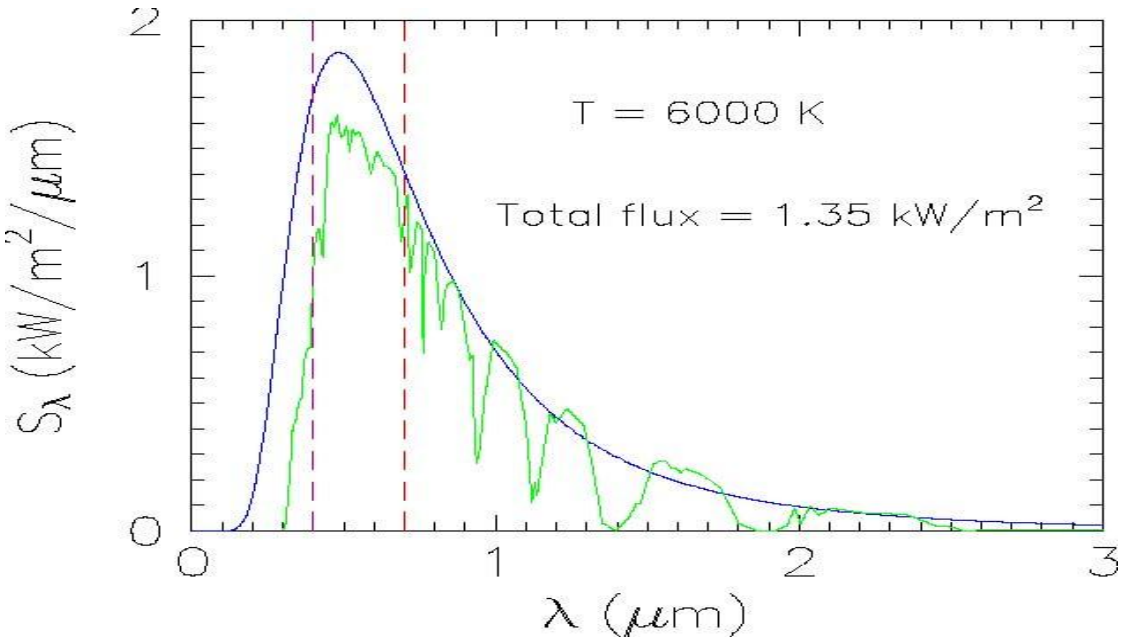

Figure 3.3: Spectral irradiance against wavelength requirement for solar cell materials. The two vertical dashed lines represent the visible region of the electromagnetic spectrum (Smestad *et al.*, 2008).

Methods for fabricating photoanodes for DSSC are determined by their ability to deposit highly porous films that provide increased surface area for dye attachment and electrolyte penetration. The electrophoretic deposition technique (EPD) is explored in this study to fabricate photoanodes comprising of TiO_2/Nb_2O_5 composite films for application in dye-sensitized solar cells.

3.3 Possible Film Structures from EPD Deposition

There are three possible film structures obtained when two particles are deposited simultaneously using EPD technique: Core-shell film structures (Diamant, *et al.*, 2004; 2011), mixed particles-composite structures (Chou *et al.*, 2011) and layered film structures (Paula *et al.*, 2014). Core-shell structures comprise a core structural domain of nanostructures

such as nanoparticles, or nanowires, and a shell structural domain of a coating layer covering the surface of core nanomaterials (Figure 3.4a). Since TiO_2 is the material of choice in fabricating photoelectrodes for DSSC, it is typically used as the core material while other metal oxides like MgO, ZnO, ZrO_2 are used as the overlayer materials in core-shell structures.

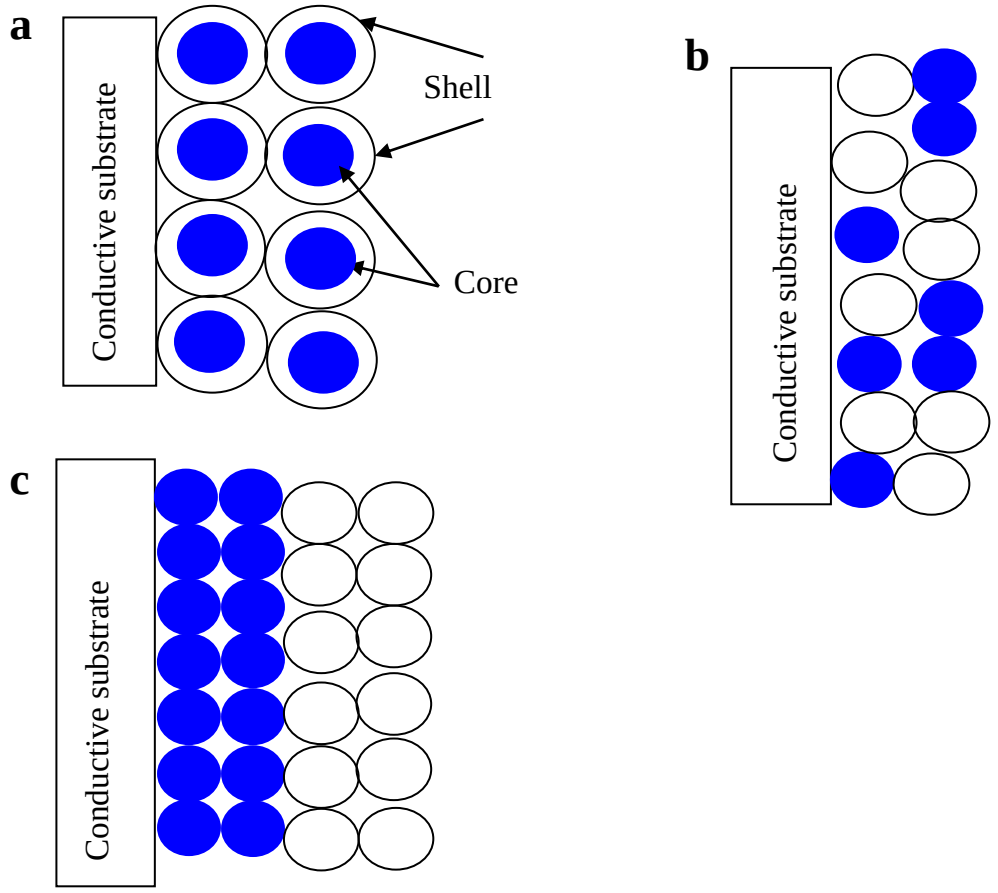

Figure 3.4: Possible film structures of two-particle EPD deposition (a) Core-shell structures (b) mixed particles structure and (c) layered structures. (Diamant, *et al.*, 2004; Chou *et al.*, 2011; Paula *et al.*, 2014)**.**

The goal is to enhance cell performance by decreasing the charge recombination using the metal oxides. Mixed particles-composite structures (Figure 3.4b), involve mixing particles of two materials and depositing the film on a glass substrate. Layered structures (Figure 3.4c) involve depositing alternate films of two particles to form a layered film.

(a) The Dye (sensitizer)

The dye molecules absorb light photons, become excited, and inject electrons into the CB of the metal oxide or semiconductor. The ideal dye should firmly chemisorb to the surface of the semiconductor through carboxylate groups (COOH) as attachment units (Gratzel, 2005). As the dye molecule bonds with the metal oxide (e.g., TiO_2), a proton (H^+) is released, leaving the dye molecule negatively charged. Categories of sensitizers include metal-free organic sensitizers, metal- complex sensitizers, and natural sensitizers. The dyes based on transition metals like ruthenium (Figure 3.5) have been shown to yield higher cell efficiencies (Kalyanasundaram and Gratzel, 2009). The relative positions of the energetic levels of excited dye and metal oxide are responsible for the charge separation i.e., the lowest unoccupied molecular orbital (LUMO) level of all dyes is much higher than that of the semiconductor band edge (- 4.0 eV). Molecules in excited states have a strong ability to inject electrons into the semiconductor conduction band.

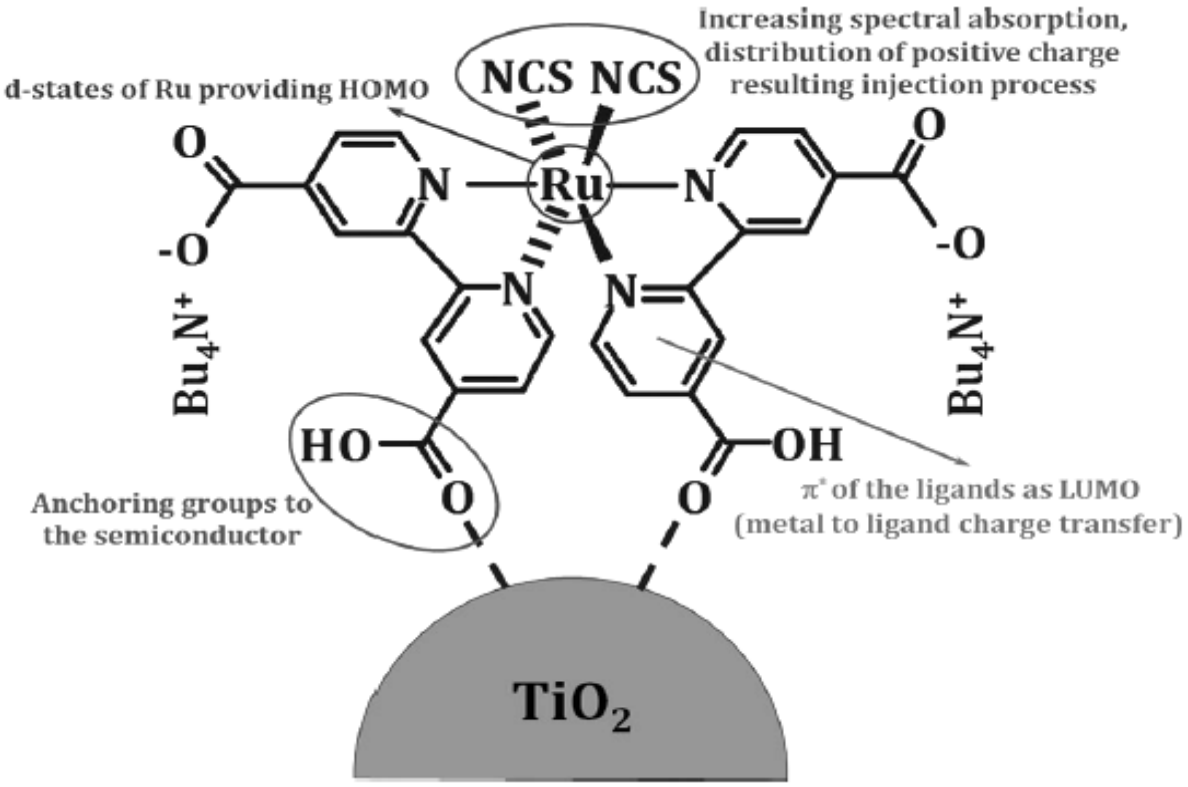

Figure 3.5: The molecular structure of cis-bis(isothiocyanato)bis(2,2'-bipyridyl-4,4'-dicarboxylato)-ruthenium(II) bis-tetrabutylammonium [Dye N719] illustrating the function of different components and the absorption spectrum (Gratzel, 2005).

The highest occupied molecular orbital (HOMO) level of all dyes is lower than that of red-ox couple such as iodide/triiodide (I^-/I_3^-) (ca. -4.8 eV) (Boschloo & Hagfeldt, 2009). The excited dye molecules become restored by obtaining electrons from the electrolyte. Thus, the regeneration of oxidized dye molecules, and electron injection into conduction band of a semiconductor are energetically permitted processes.

(b) Electrolytes

An important component of the electrolyte is the red-ox couple which reduces the oxidized dye after it injects electrons into the CB of the semiconductor. The electrolyte also functions as transporter of charges between the photoelectrode and the counter electrode. It is required that the electrolyte have a low viscosity and high electrical conductivity for faster electron diffusion. A liquid electrolyte facilitates high mobility of electrons and penetrates easily into the nanopores of the semiconducting film. The iodide /triiodide red-ox couple (I^-/I_3^-) has been widely employed because it has consistently yielded the highest conversion efficiency. The dye reduction mechanism by red-ox couple, consists of multi charge transfer process given in following set of equations (Benekohal, 2013);

First, the iodide (I^-) and the oxidized dye (D^+) form a dye-iodide $(D...I_2^{-\bullet})$ complex according to;

$$I^- + D^+ \rightarrow (D...I_2^{-\bullet}) \qquad (3.9)$$

Second, the dye-iodide complex $(D...I_2^{-\bullet})$ dissociates to dye (D) and iodide complex ($I_2^{-\bullet}$) according to;

$$(D...I_2^{-\bullet}) \rightarrow D + I_2^{-\bullet} \qquad (3.10)$$

Lastly, the $I_2^{-\bullet}$ form triiodide (I_3^-) and iodide (I^-) according to;

$$2I_2^{-\bullet} \rightarrow I_3^- + I^- \qquad (3.11)$$

The triiodide (I_3^-) ions migrate to the counter electrode where they are reduced to iodide (I^-) ions. Concentration of iodide (I^-) ions is around ten times greater than concentration of triiodide (I_3^-) ions in typical electrolytes (Boschloo & Hagfeldt, 2009). Charge transfer processes between the electrodes are restricted by the diffusion of the I_3^- ions.

(c) Counter electrodes

The counter electrode (CE) comprises a catalyst deposited on a transparent conductive oxide (TCO) to ensure sufficient fast reduction kinetics (Boschloo & Hagfeldt, 2009). Reduction of the red-ox couple (triiodide (I_3^-) ions to iodide ($3I^-$)) takes place at platinum-counter electrode as was described in equation 3.3;

$$I_3^- + 2e^- \rightarrow 3I^- \qquad (3.3)$$

Platinum (Pt) is generally used as the catalyst in CE because of its high catalytic activity for reduction of the red-ox couple as well as its chemical stability (O'Regan & Gratzel, 1991)

3.3.1 Theory of electrophoretic deposition (EPD) of photoanode

Electrophoretic deposition (EPD) is a, versatile, fairly rapid and cost effective colloidal method consisting of two-steps: electrophoresis and deposition. In electrophoresis, particles suspended in a liquid acquire electric charges and are forced to move towards the electrode that is oppositely charged, upon application of an electric field to the suspension. In deposition, the particles coagulate at one of the electrodes and form a coherent deposit on it as depicted in Figure 3.6 (Van der Biest and Vandeperre, 1999; Kawakita *et al.*, 2009).

Electrophoretic deposition (EPD) of particles can be achieved by either cathodic deposition where particles in suspension develop positive charges and deposit on the cathode or by anodic EPD where negatively charged particles deposit on the anode. Electrophoretic deposition (EPD) is distinguished from electrolytic deposition (ELD) in that whereas ELD is based on ion species from a salt solution, EPD is based on charged particles suspended in a solvent.

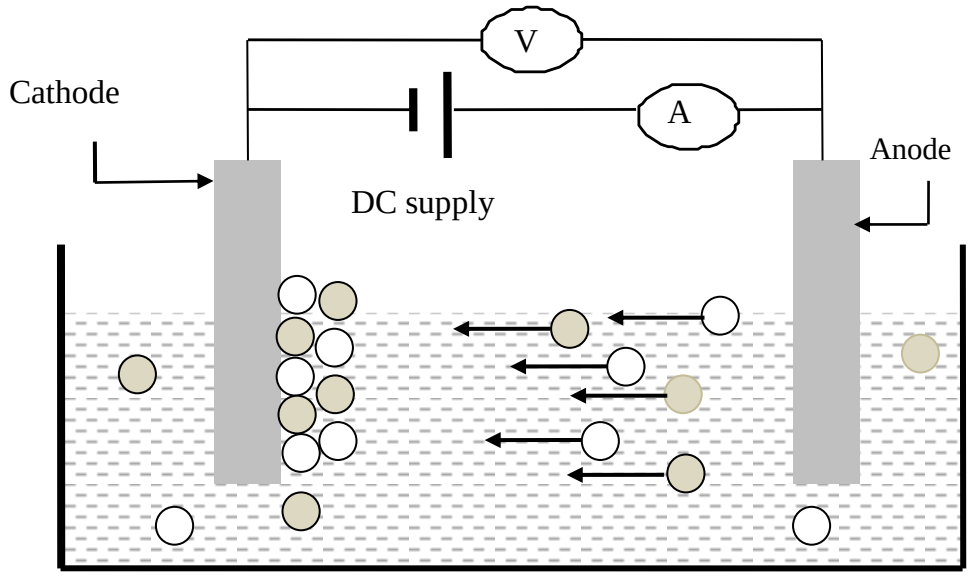

Figure 3.6: Schematic drawing of the EPD setup showing cathodic deposition of charged particles of mixed metal oxides.(Dickerson & Boccaccini, 2012).

There are no chemical reactions between electrodes and particles involved in EPD process and therefore charged particles retain their charge on being deposited (Sarkar and Nicholson, 1997). The electrophoretic deposition technique usually produces a porous particle film which can be followed by a densification step such as sintering to enhance density/compactness of the film.

3.3.2 Factors influencing EPD

The electrophoretic deposition (EPD) process is governed by a number of parameters included in the following Equation (3.12) and which was first proposed in 1940 by Hamaker (Besra & Liu, 2007). Equation (3.12), earlier on referred to as Equation (2.1), is a modified Hamaker's equation relating the mass of electrophoretically deposited film to EPD parameters.

$$m = \frac{2}{3} \cdot \varsigma_0 \cdot \varsigma_r \cdot \xi \left(\frac{1}{\psi}\right)\left(\frac{V}{b}\right) \cdot c \cdot t \qquad (3.12)$$

where m is the deposited mass, ς_0 is permittivity of free space, ς_r is relative permittivity of the solvent, ξ is the zeta (electrokinetic) potential) of the particles, ψ is the viscosity of the solvent, V is the applied DC voltage, b is the electrodes separation distance, c is particle/powder concentration in the suspension, and t is the deposition time.

The parameters in Hamaker's equation (3.12) have been categorized into two groups: (i) those associated with the suspension such as permittivity of solvent, zeta potential, and viscosity of solvent, and (ii) those associated with the EPD process such as powder/particle concentration, applied voltage, distance between electrodes, and deposition time (Van Tassel & Randall, 2006). Additionally, parameters such as surface properties of suspended particles, the physicochemical nature of the liquid medium, and the influence of type of charging mechanism or additives must be considered regarding the suspension properties. These broad suspension parameters are related to viscosity, dielectric constant, and the zeta potential. The suspension parameters can be maintained constant by fixing the type of solvent used, the type of particles in suspension, the additives used, and the apparatus for EPD.

(i) Suspension related parameters

(a) Viscosity of suspension and dielectric constant

Viscosity (ψ) is considered a major controlling parameter in the casting processes like EPD.
In the EPD process, the particle concentration in suspension is low which mean that viscosity should never be used to assess the dispersion state. The high concentration of ions in the solvents with high dielectric constants, decreases the size of the double layer region leading to electrophoretic mobility and deposition. The concentration of the ions in the liquid must be maintained low. The desired properties of the suspension include high dielectric constant, low viscosity, and low conductivity (Van Tassel & Randall, 2006).

The Zeta (electrokinetic) Potential (Z_p)

An important parameter that contributes to the stability of suspensions and particle mobility is the Zeta potential (Z_p) (Van der Biest & Vandeperre,1999). Zeta potential measures the potential difference (in mV) between the suspension containing the particle and the layer of fluid holding the oppositely charged particles related to the nanoparticle surface. A schematic

of the diffuse layer accompanied by potential distribution across the diffuse layer is shown in Figure 3.7.

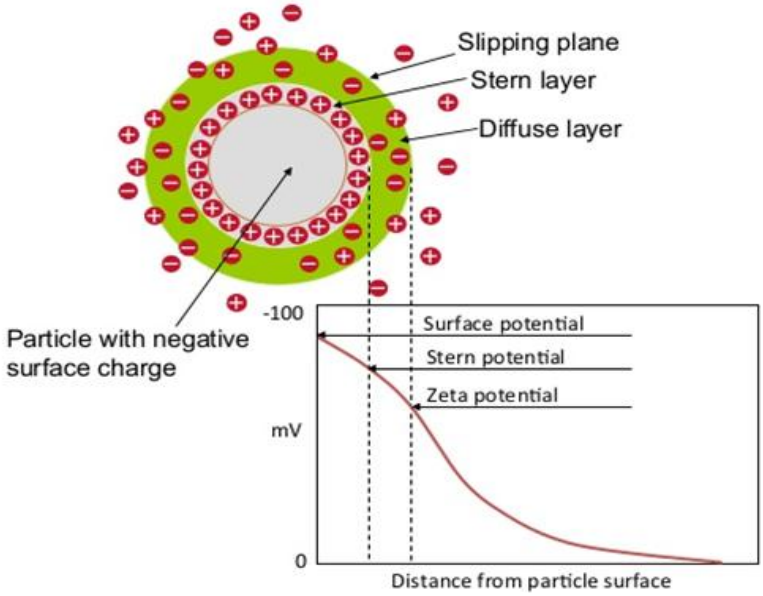

Figure 3.7 Schematic of the electrical diffuse layer at the surface of a particle suspended in solvent and the potential distribution across the double layer (VanderBiest & Vandeperre, 1999).

The magnitude of the Zeta Potential (Z_p)significantly indicate the extent of electrostatic repulsion between all the adjacent, like charged particles in a solution or dispersion. Higher magnitude of Zeta potential exhibit increased electrostatic repulsion and therefore increased stability. Zeta potential can be controlled through use of charging agents like adsorbed ions, acids, and bases (Van Tassel & Randall, 2006). The charging agents control the polarity and magnitude of induced charge on the particle. For example, magnesium nitrate ($Mg(NO_3)_2$) salt was used by Yum *et al.*, (2005) as additive in suspension of TiO_2 in 2-propanol. They observed that values of zeta potential of suspension changed from negative to positive, a change they attributed to the adsorption of $MgNO_3^+$ ion to the particle surface. For particles in the nanoscale range a high zeta potential improves the stability problems (Van Tassel & Randall, 2006).

Figure 3.8 shows a typical variation of Zeta potential (Z_p) with pH of a suspension. If the pH of suspension is reduced up to a specific point referred to as isoelectric point, the surface charge (and zeta potential) on particle becomes zero. Particles with negative Zeta potential

will bind to positively charged electrode, while those with positive Z_p will bind to negatively charged electrode.

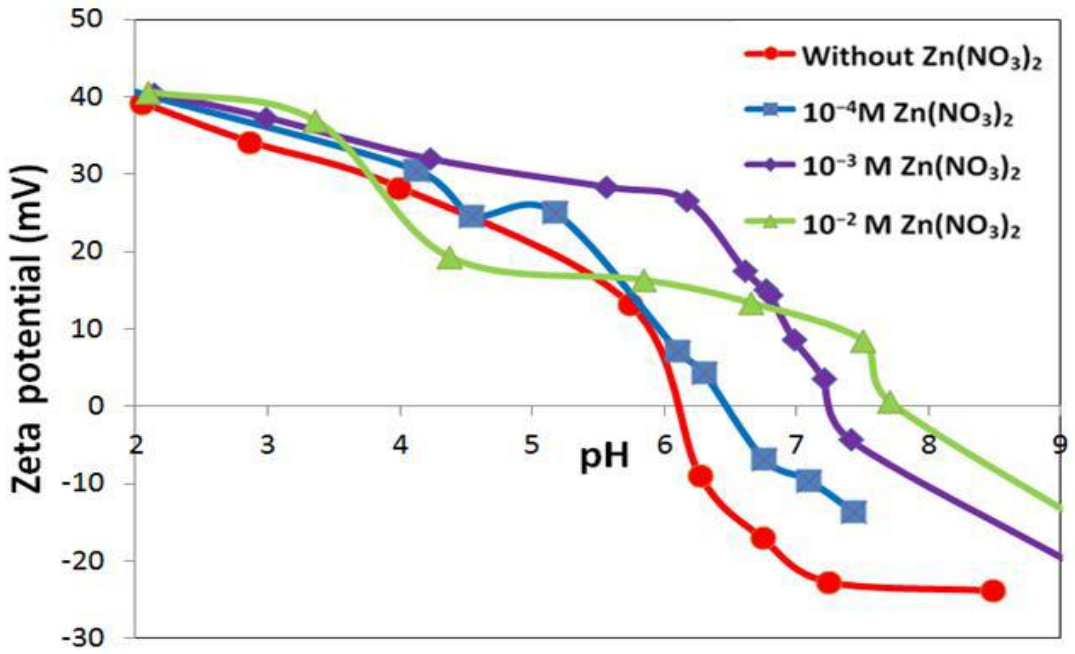

Figure 3.8: Typical variation of Zeta potential of TiO_2 nanoparticles as a function of pH for different concentrations of $Zn(NO_3)_2$ in the 5%*v/v* isopropanol-water suspension containing different amounts (Benehkohal, 2013)

Benehkohal (2013) investigated the variation of zeta potential on pH of suspension using different amounts of $Zn(NO_3)_2$ as a charging agent. He obtained the best suspension stability with pH of 4 corresponding to Zeta potential of 36mV and 1mM $Zn(NO_3)_2$ .From Figure 3.8, the increased positive charge density on the surface of the nanoparticles at lower pH increases the zeta potential value.

(b) Charge of particles

The presence of charge on the surface of suspended particles is a key factor in electrophoretic deposition. Charging of particles in suspension is greatly enhanced by presence of ions or decomposing additives. A variety of additives such as $Mg(NO_3)_2.6H_2O$, iodine and $Zn(NO_3)_2$ can be added to EPD suspensions as charging agents. Particle surfaces in suspension acquire positive charge if metal ions adsorb on the particle's surface. Magnesium nitrate hexahydrate ($Mg(NO_3)_2.6H_2O$) dissociates according to:

$$Mg(NO_3)_2 \rightarrow Mg\,NO_3^+ + NO_3^- \quad (3.13)$$

The $Mg\,NO_3^+$ ion charges the particles positively causing them to move to the cathode when a DC electric field is applied.

(ii) Process-related EPD parameters

If the apparatus for the EPD, and the suspension are fixed, then the zeta potential, permittivity, viscosity and electrode separation in equation (3.13) are constant. Consequently, the mass (m) of electrophoretically deposited film is a function of process-related parameters i.e., applied voltage V, particle concentration c, and deposition time t according to following equation (3.14) (Besra & Liu, 2007);

$$m \propto CVt \quad (3.14)$$

The particle concentration, applied voltage and deposition time being process-related parameters corporately contribute to film mass. It is necessary to determine the electrophoretic deposition parameters for all combinations of particle concentration in suspension, deposition time, and applied voltages to predict the deposition behaviour.

3.4 Optical Characterization of Deposited Films

Optical properties of a semiconductor can be defined as properties that involve the interaction between light and the semiconductor. They include absorption, transmission, extinction, Urbach energy, and band gap energy. The theoretical foundation of these optical properties is given in following sections.

(a) Absorption coefficient and transmittance

When light is incident on surface of a semiconductor material, it can be reflected off its surface, transmitted through the material, or absorbed by the material. Light is further attenuated by a significant amount, as it passes through a semiconductor thin film as shown in Figure 3.9. When light of intensity I_0^* is incident on surface of a thin film of semiconductor, a portion of the light is transmitted through the film, and exits the material with intensity $I^*(z)$.

The rate of absorption of monochromatic light varies exponentially with the intensity for a given wavelength.

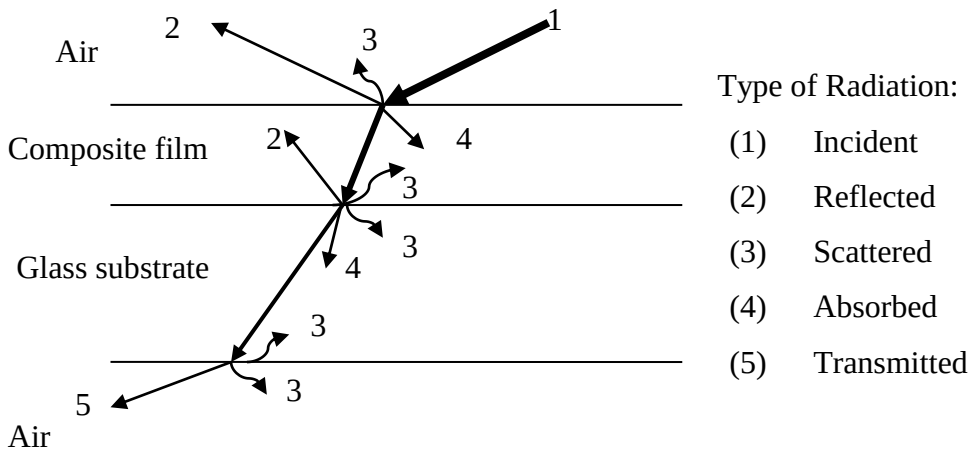

Figure 3.9: Typical transmission of radiation through a film and substrate. Also shown are the sources of attenuation of incident light including reflection, scattering and absorption of the light.

The following equation models the exponential decay of monochromatic light as it travels through a semiconductor (Goetzberger, 1998).

$$I^*(z) = I_0^*(z)e^{-\alpha z} \tag{3.15}$$

where $I^*(z)$ is the intensity at a distance z below the surface, $I_0^*(z)$ is intensity at surface point z_0 and α is the absorption coefficient, which determines the depth at which light of certain wavelength penetrates the semiconductor.

Absorption coefficient reflects how strongly a particular photon gets absorbed in a material. It is a material property whose values vary from material to material. The value of absorption coefficient $\alpha(\lambda)$ is controlled by the wavelength of the monochromatic radiation and is a determining parameter in calculating the required film thickness for absorbing most of the solar radiation falling on the material. The absorption coefficient as a function of transmittance (*%T*) is given by; (Tepantlan *et al*., 2008)

$$\alpha(\lambda) = \frac{1}{z}\ln\left(\frac{100}{\%T}\right) \tag{3.16}$$

where z is film thickness and $\%T$ is equal to 100 multiplied by the ratio of intensity of light (I^*) to the intensity of incident light (I_0^*).

Small values of absorption coefficient (α)indicate weak absorption while large values of α indicate strong absorption of light in a material. The inverse of α is known as absorption length (z_a) and expressed as:

$$z_a = 1/\alpha \tag{3.17}$$

A requirement for solar cells is for film thickness (z) to be significantly larger than the adsorption length to ascertain the quantitative light harvesting in the spectral absorption range (Gratzel, 2005). High value of α for a semiconductor represents high absorption probability since only photons are involved in light absorption. Thinner solar cells can be fabricated from direct band gap semiconductors because for high value of α, only a small thickness in range of a few micrometers is required to absorb relevant range of photons. It follows that the thickness of the nanocrystalline film applied in DSSC is typically of the order of a few micrometers in order to ascertain enhanced light absorption.

(b) Optical band gap (E_g)

In an intrinsic semiconductor, optical band gap indicates the region linking the top of the valence band (V_B) which is completely filled with electrons, and bottom of the conduction band (C_B) that is bare of electrons. Ideally, it is the energy range over which the density of states is zero. The optical band gap is very large for insulators but nil for metals. The band gap in semiconductors is typically intermediate between these two. The ability of a semiconductor to absorb light from solar spectrum depends on the size of its band gap. To examine the band gap of a semiconductor, light with variable photon energy near the band gap is used. In such a case, light with lower energy photons does not get absorbed and light with high photon energy is absorbed. The photon energy at which transition between absorbing and non-absorbing behaviour takes place correspond to the optical band gap energy. This transition between absorption and transmission is gradual and thus provides

information into some details of the transitions between energy states in valence band and conduction band. The region of this transition is called absorption edge. It is difficult to define the absorption edge experimentally due to formation of a tail in the absorption spectrum (Li *et al.*, 2009). As a result, the Tauc model has been devised as an empirical model for measuring the optical band gap (Sanchez, 2014). The optical absorption edge in semiconductors is analyzed using the Tauc model given in following equation (Tauc, 1966);

$$\alpha h\upsilon = B(h\upsilon - E_g)^m \tag{3.18}$$

where α is absorption coefficient, h is Planck's constant, υ is frequency, B is a proportionality constant (band tailing parameter) taking values between 10^7 and 10^8 m^{-1} (Illican, 2008), E_g is the optical band gap energy, and m is a constant that assumes values $m = ½$ for direct band gap or $m = 2$ for an indirect band gap (Gould & Lamont, 2010). The optical band gap energy (E_g) for semiconductor thin films can be evaluated by considering transition between valence band and conduction band when a photon of energy, $h\upsilon$, falls on the semiconductor.

i) For direct transitions, $m = ½$ and equation (3.18) becomes;

$$(\alpha h\upsilon)^2 = B(h\upsilon - E_g) \tag{3.19}$$

The plot of $(\alpha h\upsilon)^2$ versus $h\upsilon$ should be linear over a wide range of photon energies for direct transition. The intercept of this plot on the energy axis gives the energy band gap (E_g) (Swanepoel, 1983).

ii) For indirect band gaps: $m = 2$ and equation (3.19) becomes

$$\alpha h\upsilon = B(h\upsilon - E_g)^2 \tag{3.20}$$

Plotting α versus $h\upsilon^2$ shows a linear dependence.

The photon energy is related to wavelength in (nm) according to;

$$E = h\upsilon = h \cdot \frac{c}{\lambda} = \frac{1240}{\lambda(nm)} \qquad (eV) \tag{3.21}$$

From equations (3.20) and (3.21) the absorption coefficient (α) of a material depends on the wavelength of light incident. Since only light photons with $h\upsilon > E_g$ can excite electrons across a materials band gap and contribute to solar cell performance, the band gap is important in synchronizing a solar cell to solar spectrum.

(c) Urbach energy (E_U)

In optical absorption in a semiconductor, electrons get excited across the energy band gap from the top of the valence band (VB) to the bottom of the conduction band (CB). If the electrons encounter disorder during this transition, their density of states decrease exponentially (tail off) into the energy gap away from CB. This tail of density of states extending into the energy band gap is termed Urbach tail and the energy associated with it is the Urbach energy. Swanepoel, (1983) and Caglar, (2006) reported that absorption coefficient (α) near the band edge assume an exponential dependence on photon energy estimated by following equation;

$$\alpha = \alpha_0 \, exp\left(h\upsilon / E_U\right) \tag{3.22}$$

where E_U is Urbach energy and α_0 is a material dependent constant.

Thus, the Urbach energy can be estimated by plotting $ln\,\alpha$ against photon energy $(h\upsilon)$. The linear part of the resulting curve can then be fitted with a straight line. The Urbach energy equals the inverse of the slope. Thus the exponential band tailing can explain the observed Urbach tail of the absorption coefficient versus photon energy. The values of Urbach energy indicate the degree of structural disorder in a semiconductor. High E_U indicates substantial formation of tail states at the band margins.

(d) Refractive index (n**)**

The refractive index (n) of a material is defined as the ratio of speed of light in a vacuum to phase velocity of light in the medium. The concept of refractive index is widely used with

components of the electromagnetic spectrum from radio waves to x-rays. The refractive index varies with the wavelength of light and can be calculated from the measured transmittance (T) and reflectance (R) using any of the following three equations: (i) equation (3.23) when the absorption is high (ii) equation (3.24) when interferences are determined and (iii) equation (3.25) when absorption is low and there are no interferences (Born & Wolf, 2005). In the first case where the absorption is high and there is nil or minimal interferences, Equation (3.23) was developed to calculate refractive index n_f for thin films (Benno & Joachim, 2003).

$$n_f = \left(1 + R + 2\sqrt{R}\right) \Big/ \left(1 - R\right) \tag{3.23}$$

In the second case, where absorption of the film is negligible and interferences are determined from the maxima in the transmission spectra, the refractive index (n_s) of the thin film-substrate can be derived by the following equation (Padera, 2013).

$$n_s = \left(1 + \sqrt{1 - T_{\max}^{\,2}}\right) \Big/ T_{\max} \tag{3.24}$$

where T_{max} is maxima in transmission spectra.

In the third case, where the absorption is low and there are nil or minimal interferences the sample refractive index (n_f) can be computed from the transmission minima (T_{min}) by using the following equation:

$$n_f = \sqrt{M + \sqrt{M^2 - n_s^2}} \tag{3.25}$$

When light, an electromagnetic wave, propagates through a material, part of the light gets attenuated. This attenuation can be accounted for by defining a complex refractive index $(\vec{n})$ as follows;

$$\vec{n} = n + i\,k \tag{3.26}$$

where n is the real part and k is the imaginary part of the complex refractive index. In addition, k is also known as extinction coefficient associated with the attenuation of light passing through the material. In a material science, the properties of a composite material (film) can be predicted using the rule of mixtures given in following expression: (Callister & Rethwisch, 2010).

$$n_c = f\, n_N + (1 - f) n_T \tag{3.27}$$

where n_c is the refractive index of composite film, f is the volume fraction of one of the particles in the mixed-nanoparticle composite, n_N and n_T are refractive indices of the two nanoparticles respectively.

(e) Extinction coefficient (k)

The extinction coefficient (k) is the imaginary part of the complex refractive index and measures the fraction of light lost due to scattering and absorption per unit distance in the participating medium when an electromagnetic wave propagates through a material. Since all components of electromagnetic waves or radiations travel in a vacuum at the speed of light, c, the extinction coefficient can be related to the absorption coefficient (α) according to following equation (Yakuphanoglu *et al*., 2007):

$$k = \frac{c\,\alpha}{4\pi\nu} = \frac{\alpha\,\lambda}{4\pi} \tag{3.28}$$

The extinction coefficient (k) is zero when light travels through the material without loss, whereas, k > 0 when light is absorbed. The extinction coefficient- depends on wavelength (λ) of incoming light and on the intrinsic qualities of the material. A high extinction coefficient is necessary for absorption of sunlight to make a good solar cell.

3.5 Electrical Characterization

Electrical characterization of thin films can be used to determine the electrical resistivity (ρ), sheet resistance (R_s), conductivity (σ), Hall mobility (μ_H), charge carriers density (n_d)

and type of charge carriers. The following sections give the theoretical foundations governing the measurement of electrical properties by the Hall effect and the four point probe techniques.

3.5.1 The Hall Effect

In 1879, Edwin Hall reported that when a magnetic field is applied transverse to the direction of an electrical current in a conductor, an electric potential difference proportional to both the magnetic field and the current is developed across the material in a direction perpendicular to both current and potential (see Figure 3.10). This Hall Effect has been used to ascertain the polarity of the moving charges that form the electric current. The Hall Effect measurements are critical in electrical characterization of semiconductor materials and films because the type of charge carrier, charge carrier density, and Hall mobility can be derived from the Hall voltage. The many important applications of Hall Effect include position and motion detectors, detection and measurement of magnetic fields for instance in cars electronic ignition systems, and determination of type of charge carriers in semiconductor materials (Pengra *et al.,* 2014). For semiconductors, the particle size and band structure can give rise to both negative (electron-like) or positive (hole) or absence of an electron) effective charge carriers.

In equilibrium, the magnetic force (F_B) equals to the electric force (F_E) and for a conductor of width l , the developed Hall Voltage (V_H) is given by;

$$V_H = E_H\, l = v_x\, B_y\, l \tag{3.29}$$

Where E_H is the measured Hall electric field, v_x is the average velocity of charge carriers, and B_y is magnetic field in the y direction.

The average velocity (v_x) of charge carriers is obtained from (Jewett & Serway, 2010)

$$v_x = I_x / n_d q l z \tag{3.30}$$

where I_x is the current through the sample, n_d is the charge carrier density, (q) is the elementary charge, l is the semiconductor width and z is the semiconductor thickness.

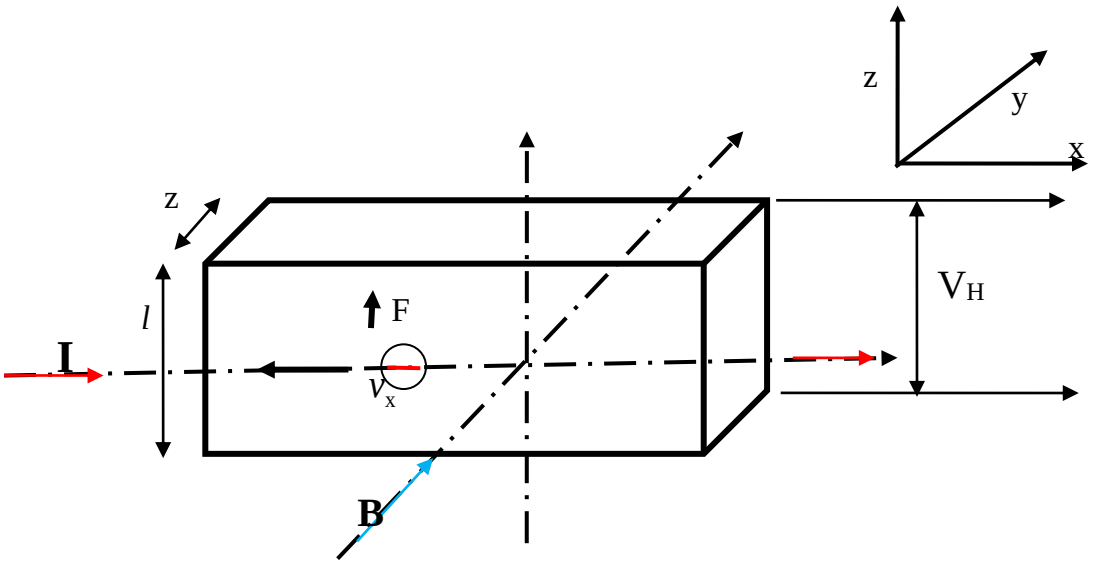

Figure 3.10: Arrangement for measuring the Hall voltage showing current in x-direction, magnetic field in y- direction and Hall voltage measured in z-direction.(Jewett & Serway, 2010).

(a) The Hall voltage (V_H) and Hall coefficient (R_H)

The Hall voltage (V_H) can be obtained from equations (3.29) and (3.30) as:

$$V_H = \frac{I_x B_y}{n_d q z} = R_H \frac{I_x B_y}{z} \tag{3.31}$$

where R_H is the Hall coefficient and given by

$$R_H = \frac{1}{n_d q} \tag{3.32}$$

According to this equation (3.32), the Hall coefficient (R_H) varies inversely with the number of charge carrier density (n_d). From equation (3.32), the Hall coefficient is expressed in terms of measurable quantities according to;

$$R_H = \frac{z V_H}{I_x B_y} \ (cm^3 C^{-1}) \qquad (3.33)$$

Where V_H is the Hall voltage measured along z-axis, I_x is current, B_y magnetic field and z is the sample thickness.

The values of Hall voltage, current and magnetic field are measured using the Hall Effect equipment. With known value of thickness (z), the Hall coefficients can be obtained from equation (3.33).

(b) Charge carrier density (n_d)

Charge carrier density is an important electrical property of semiconductors typically measured using the Hall Effect technique. Using equation (3.33), the number density of charge carrier (n_d) is evaluated from fundamental charge (q) and Hall coefficient (R_H) according to following equation 3.34:

$$n_d = \frac{1}{qR_H} \ (cm^{-3}) \qquad (3.34)$$

The sign of Hall coefficient determines the type of charge carriers in the sample. It is negative if majority charge carriers are electrons ($n-$type semiconductors), and positive if charge carriers are holes ($p-$type semiconductors).

(c) Film resistivity

In a semiconductor, the electrical conductivity is determined by Hall mobility among other factors. The electrical resistivity (ρ) can be readily measured using the four point probe. For a thin sample, film resistivity (ρ) is expressed as:

$$\rho = \frac{\pi}{\ln 2}\frac{V}{I} \ z = R_S \ z \qquad (\Omega^{-1} cm^{-1}) \qquad (3.35)$$

and $$R_S = \frac{\pi}{\ln 2}\frac{V}{I} = 4.532 \times \frac{V}{I} \qquad (\Omega / square) \qquad (3.36)$$

where R_s is the sheet resistance, V is voltage, I is current and z is sample thickness.

Electrical resistivity of the film is therefore the product of film thickness (z) and sheet resistance (R_S). As indicated in equation (3.36), the voltage becomes an indication of sheet resistance if a constant current source is used. The sheet resistance influences the series resistance of the cell. A low value of sheet resistance is preferred, but low sheet resistance requires thicker layers causing reduced light transmittance and efficiency (Han *et al*., 2005). The sheet resistance of semiconductor films can be measured using the four point probe where two probes are used for current injection and the other two probes are used to measure the voltage drop. The more usual probe geometrical configuration is when the four probes are placed in a straight line (Deen & Pascal, 2006).

(d) Hall mobility (μ_H)

The Hall mobility (μ_H) is defined as product of Hall coefficient (R_H) and electrical conductivity (σ) according to:

$$\mu_H = R_H \ \sigma \tag{3.37}$$

Equation (3.37) can be used to determine the mobility of the charges in the deposited films.

3.6 Structural Characterization

The crystalline phase composition is analyzed using X-ray diffractometer (XRD). The x-ray photons with energy typical of the target material are used. The photons are typically displayed in the form of high intensity-characteristic peaks used for diffraction analysis. When these x-rays are focused on a material, they get reflected by the atoms in specific directions. The difference in path length of reflected beams must be an integral number of wavelengths for maximum intensity according to Bragg's law;

$$n\lambda = 2d_{hkl}\sin\theta \tag{3.38}$$

where λ is the x-rays wavelength, d_{hkl} is inter planar crystal spacing, and θ is the angle made by incidence x-rays with crystal planes.

The process of reflection occurs when reflected beams are generated from at angle 2θ from the incident beam. The shape of the unit cell determines the indices ***h,k,l*** that define the possible ***d***-spacing. i.e.,

$$\sin\theta = n\lambda / 2d_{hkl} \tag{3.39}$$

The highest electron densities are found around atoms. Thus, the intensities depend on the type of atoms present in material and positions in the unit cell. Equation (3.39) is used in the analysis of the diffraction patterns of the sample material and hence is used for elemental identification and the kind of crystal orientation (Simiyu, 2010). The diffraction pattern of the sample is obtained by plotting the X-ray intensity in ***a.u***. on the y-axis and the measured diffraction angle 2-Theta on the x-axis. The diffraction pattern consists of a series of peaks which correspond to x-rays diffracted from a specific set of planes in the specimen. The positions of peaks depend on the crystal structure of the material that enables the determination of structure and lattice parameters of the material. The standard peaks and intensities for materials can be obtained from databases of powder diffraction files (PDF) such as that of the Joint Committee on Powder Diffraction Standards (JCPDS). Experimentally obtained peaks may vary slightly from the standard ones and the main variation arise from the peak broadening that is mainly caused by the size of the crystal and the overlapping of the peaks.

Subsequent to optical, electrical, and structural characterization, the semiconductor films can be chemisorbed with a dye thereby forming photoelectrodes to be used in a dye-sensitized solar cell. The dyes inject electrons into conducting band of the films which in turn, conduct the electrons to the external circuit resulting in an electric current (O'Regan & Gratzel, 1991). Consequently, the assembled DSSCs are characterized to determine their performance.

3.7 Characterization of DSSCs

Dye-sensitized solar cells are usually characterized using photoelectric current-voltage (I-V) measurements and curves. The photovoltaic parameters corresponding to I-V measurements include short-circuit current density (J_{SC}), fill factor (*FF*), open circuit voltage (V_{OC}), and efficiency (η).

(a) The short circuit current density (J_{SC})

When a load is connected to a solar cell, a voltage develops across the terminals of the cell. A solar cell is usually treated as a diode. The dark current density (J_{dark}) is given by following equation, (Maluta, 2010)

$$J_{dark} = J_0\left(\exp\left(qV \big/ k_B T_{emp}\right)\right) \tag{3.40}$$

where J_0 is the reverse bias saturation current density, q is elementary charge, V is the voltage across the terminals, k_B is Boltzmann's constant, T_{emp} is temperature.

The short circuit current density (J_{SC}) is the current drawn when the terminals of the circuit are connected together and therefore the applied voltage across the device is zero. The net current density (*J*) can be attained from the difference between the short circuit current density (J_{SC}) and dark current density (J_{dark}):

$$J = J_{SC} - J_{dark} = J_{SC} - J_0\left(\exp\left(qV \big/ k_B T_{emp}\right) - 1\right) \tag{3.41}$$

The short circuit current (I_{SC}) increases linearly with light intensity. It also depends on the amount of the dye chemisorbed onto the semiconductor and on the electrochemical or electrokinetic properties of the red-ox couple in the electrolyte.

(b) The open circuit voltage (V_{OC})

Photovoltage in a solar cell originate from the accumulation of electrons in metal oxide such as TiO_2 film. The open circuit voltage (V_{OC}) is the voltage developed when the terminals of

the circuit are isolated (infinite load resistance) and is equal to the difference between the Fermi level (E_F) of nanocrystalline semiconductor film and the electrochemical potential (ΔV_{redox}) of the red-ox couple in electrolyte, i.e.,

$$V_{OC} = E_F - \Delta V_{redox} \tag{3.42}$$

In an n-type semiconductor with electrons as majority charge carriers, the Fermi level is near the conduction band edge.

At the open circuit condition, $J_{dark} = J_{SC}$, and open circuit voltage (V_{OC}) is given by following equation (Maluta, 2010);

$$V_{OC} = \frac{k_B T_{emp}}{q} \ln\left(\frac{J_{SC}}{J_0} + 1\right) \tag{3.43}$$

The equation (3.43) shows that V_{OC} increases logarithmically with short circuit density (J_{SC}) and to reciprocal of the reverse saturation current (J_0).

(c) The fill factor (*FF*),

The fill factor (*FF*) is defined as the squareness of the IV-curve. It is therefore the ratio of areas of two rectangles marked A and B shown in Figure 3.11. Fill factor measures the ideality of the solar cell and is defined as the ratio of the maximum power output ($I_{max} \times V_{max}$) from the solar cell to the product of V_{OC} and I_{SC} ,i.e.,

$$FF = \frac{maximum\ \ power(P_{\max})}{I_{SC} \times V_{OC}} = \frac{I_{\max} \times V_{\max}}{I_{SC} \times V_{OC}} = \frac{Area\ A}{Area\ B} \tag{3.44}$$

where I_{SC} is the short circuit current, V_{OC} is the open circuit voltage, P_{max} is the maximum power, I_{max} is the current at maximum power, and V_{max} is the voltage at maximum power. At voltages below V_{max}, the photocurrent through the external load is relatively independent of output voltage (Figure 3.11). When voltage increases (> V_{max}), recombination of increasing number of charges takes place within the solar cells rather than the charges flowing in external circuit through the load. At V_{OC}, all charges recombine internally. Fill factor is

related to resistive losses in a solar cell. Theoretically, the best solar cell will have a completely square I-V curve where *FF* =1. Such a cell will generate the same current independent of the voltage.

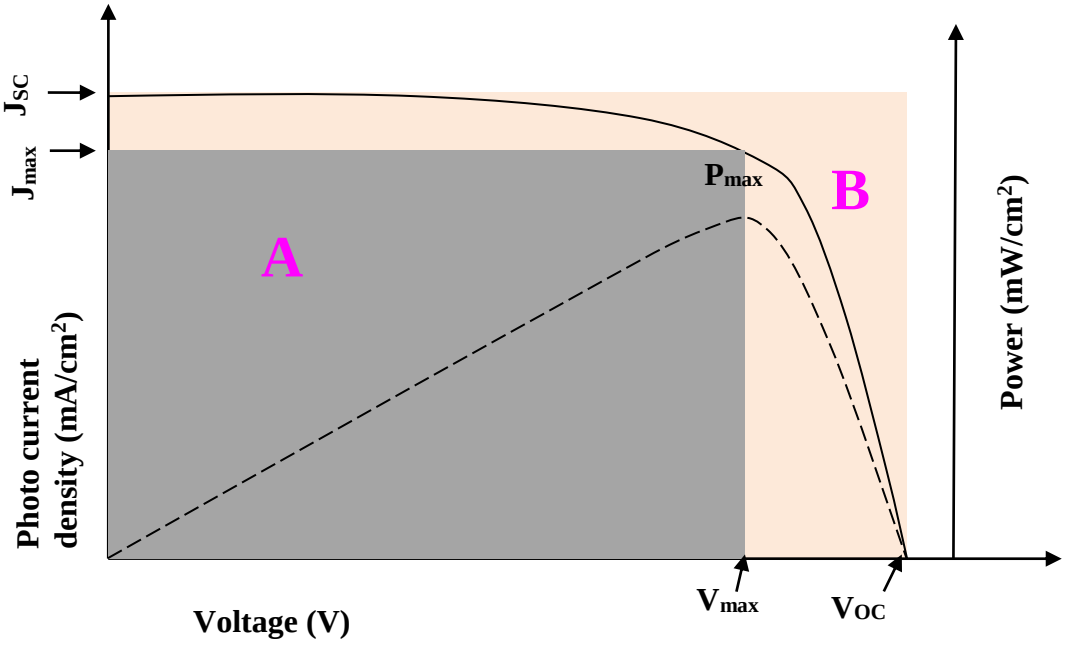

Figure 3.11: Typical graph of solar cell's output current (solid line) and power (dashed line) as function of voltage. Also shown are rectangles A and B related to *FF*, the cell's short circuit current density (J_{SC}), and open circuit voltage (V_{OC}) (Bowden *et al*., 2010).

In practice, however, no such level of squareness has been achieved. Some recent record *FF* values of different material based solar cells are shown in Table 3.1. A Fill factor loss of photon energy in solar cell arises due to series and shunt resistances of a cell. Ideally, the series resistance should be low. High values of series resistance result in reduced short circuit current (I_{SC}) but not the open circuit voltage (V_{OC}). Ideally, the values of shunt resistance (R_{SH}) should be very large (~ hundred ohms). Low values of shunt resistance affect the V_{OC} but I_{SC} remains the same. It is difficult to minimize *FF* loss beyond its fundamental limit

Table 3.1: Recorded fill factor values of various types of solar cells (Green *et al*., 2017).

Material	Record Fill Factor
Si (crystalline)	0.838
Si (multi crystalline)	0.800
GaAs (thin film cell)	0.865
CIGS (cell)	0.776
Dye-sensitized	0.712
Organic	0.742
Perovskite	0.723

(d) The solar cell efficiency (η)

The energy conversion efficiency (η) of the solar cell defines the percentage of solar light converted to electrical energy. Mathematically, it can be obtained from the ratio of maximum power ($P_{\max}$) delivered at operating point to the incident power (P_{in}). The light energy to electric energy conversion efficiency (η) is expressed as;

$$\eta\,(\%) = \frac{Power\ \ output\ \ \times\ 100\%}{incident\ \ light\ \ power} = \frac{J_{SC}\,V_{OC}\ FF\ \ (mW) \times 100\%}{Area\ (cm^2)\ \times\ P_{in}\ (mW/cm^2)} \qquad (3.45)$$

It follows from equation (3.45) that a high short circuit current (J_{SC}), a high open-circuit voltage (V_{OC}) and a fill factor (FF) close to 1 (or 100) are desirable for an efficient solar cell.

3.8 Electrochemical Impedance Spectroscopy

In a dye-sensitized solar cell the electrons injected into semiconductor by the excited dye upon light irradiation diffuse through the semi-conducting film. The electron transport within the film encounters the diffusion impedance denoted by R_d (Cisneros *et al.,* 2014). Other

internal impedances in a dye-sensitized solar cell include; (i) Nernstian diffusion related impedance (Warburg) within the electrolyte (ii) the electron transport impedances in the TiO_2/electrolyte boundary, (iii) charge transfer related impedance at the platinum counter electrode, and (iv) sheet resistance of the FTO (Shin *et al.*, 2010). The term impedance refers to frequency dependent resistance to current flow through a circuit elements such as resistors, inductors or capacitors. In addition, the term electrochemical impedance is used in DSSCs due to the cell's specific hybrid character (Bisquert *et al.*, 2000).

EIS measurements can be taken under any bias voltage and working conditions of the solar cell. The most common approach adopted in EIS measurements involve applying a small-amplitude sinusoidal voltage $V(\omega,t)$ over a wide range of frequency to an electrochemical cell and measuring the corresponding sinusoidal current at open circuit voltage. The small-amplitude excitation sinusoidal voltage $V(\omega,t)$ *d*epends on time according to following expression (Bisquert *et al.*, 2000):

$$V(\omega,t) = V_{OC} + V_0 \exp\, j(\omega t) \tag{3.46}$$

where V_{OC} is open circuit voltage, V_O is amplitude of excitation voltage, and ω is the angular frequency in radians per second. The AC signal is superimposed on a DC voltage at V_{OC} bias potential, resulting in a small-amplitude response alternating current signal $I(\omega,t)$ expressed as function of time in form:

$$I(\omega,t) = I_{OC} + I_0 \ \exp[\, j(\omega t - \phi)] \tag{3.47}$$

where I_{OC} is short circuit current, I_0 is the amplitude, and ϕ is the phase angle through which response signal shifted from the excitation signal.

The impedance $Z(\omega,t)$ of the system can be expressed in an equation derived in manner similar to Ohm's law as:

$$Z(\omega,t) = \frac{V(\omega,t)}{I(\omega,t)} = \frac{V_0 \sin \omega t}{I_0 \sin(\omega t + \phi)} = Z_0 \frac{\sin(\omega t)}{\sin(\omega t + \phi)} \tag{3.48}$$

where Z_0 is amplitude of impedance.

The smallness of amplitudes of both potential $V(\omega,t)$ and current $I(\omega,t)$ signals ensures that $Z(\omega,t)$ is independent of the amplitude of the perturbation. The impedance $Z(\omega,t)$ can then be expressed as a complex quantity because $I(\omega,t)$ contains magnitude as well as phase information:

$$Z(\omega) = |Z_0|(\cos\phi - j\sin\phi) = Z'(\omega) - jZ''(\omega) \qquad (3.49)$$

where $Z'(\omega) = |Z_0|\cos\phi$ and $-Z''(\omega) = -|Z_0|\sin\phi$ are the real and imaginary and components of the impedance, respectively and $j = \sqrt{-1}$.

(e) EIS data presentation

If the imaginary part of the impedance ($-Z''(\omega)$) is plotted on the y-axis and the real part ($Z'(\omega)$) on the x-axis, a Nyquist plot is obtained (Figure 3.12). A point on the Nyquist plot represents the impedance, measured at a given frequency. When real component of impedance is plotted against logarithmic frequency, the Bode plot is obtained (Bisquert & Fabregat-Santiago, 2010).

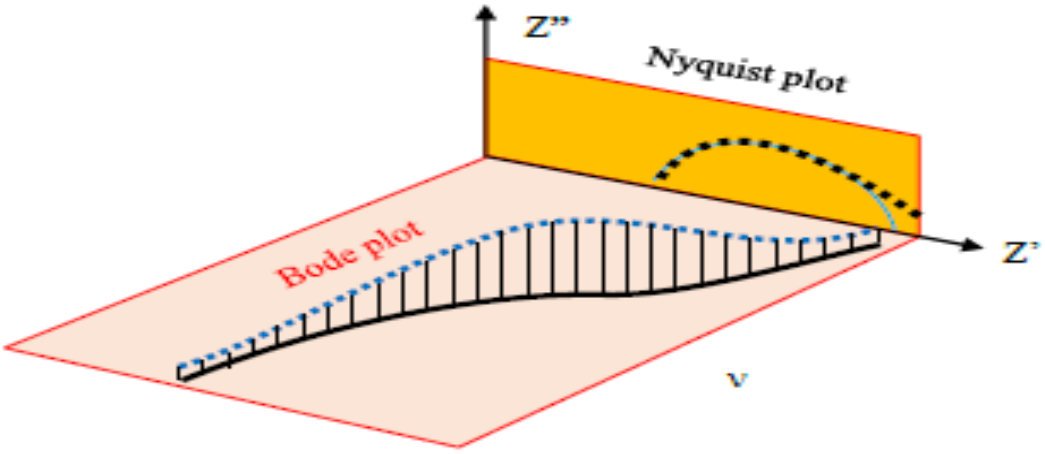

Figure 3.12: A typical Nyquist plot and Bode plots resulting from projection onto $Z'' - Z'$ plane and $Z'' - \nu$ plane for electrochemical system (Yavuz, 2014).

Bode plots explicitly show the frequency dependence unlike Nyquist plots. The semicircle on a Nyquist plot is characteristic of a single time constant. High frequency data appear on left hand side and low frequencies on the right side –positive real axis - of the Nyquist plot (Figure 3.12). Measurements of impedance at low frequencies are useful in ensuring that one approaches the DC regime. The arc in Nyquist plots characterize the time constants namely, electron lifetime (τ_n) and transit time (τ_t), related to RC circuits from which Nyquist plots result. Bode plots are frequently used to determine charge recombination time by the maximum frequency calculations (Yavuz, 2014)

(f) EIS data analysis model elements

Interpretation of EIS data can be performed by the equivalent circuit modeling, which is a method for fitting theoretical data to measured impedance data of an electrochemical device (cell). The EIS data fitting models facilitates translation of internal processes occurring in the device, including charge transport in the film, charge transfer (recombination) across interfaces, and charge accumulation at certain points. The electrical circuits in the models are typically built using (i) passive elements like resistors and capacitors, and (ii) distributed elements such as constant phase elements (CPE) and Warburg impedance (Z_d). These circuit elements can be arranged in series, parallel or their combination to build complex equivalent circuits models for the given set of data and the Kirchoff's laws applied (Autolab, 2012). Most impedance systems have data fitting programs useful for estimating model parameters.

(g) Circuit element resistance

When frequency (ω) of applied perturbation is very low $(\omega \to 0)$, the conditions in a system approximate those driven by a direct current and impedance $Z(0)$ becomes equal to DC resistance (R_{DC}), i.e.,

$$Z(0) = {V(0)}/{I(0)} = R_{DC} \tag{3.50}$$

where $V(0)$ is applied potential difference and $I(0)$ is the current at very low frequencies. The resistor's impedance is thus unaffected by frequency and has zero phase difference. Nyquist plot corresponding to a resistor becomes a vertical line. The ohmic resistance can be

obtained in a Nyquist plot at the junction of the impedance curve and the real impedance axis, corresponding to very low frequency.

When frequency (ω) becomes high, certain procedures in the system become unresponsive to the applied perturbation yet impedance must include contributions from such processes (Bisquert & Fabregat-Santiago, 2010).

(h) Circuit element Capacitor

If we divide the change in electric charge $Q(\omega)$ by a voltage perturbation $V(\omega)$, we obtain a frequency-dependent capacitance $C(\omega)$. The impedance (capacitive reactance) $Z_C(\omega)$ of a circuit element capacitance $C(\omega)$, is given by:

$$Z_C = 1/j\omega C \tag{3.51}$$

The capacitive impedance decreases as frequency increases and at very large frequencies ($\omega \to \infty$, the capacitor becomes short-circuited (Bisquert & Fabregat-Santiago, 2010). On the other hand, at very low frequencies ($\omega \to 0$) the capacitor can be substituted by an open-circuit with total impedance equal to infinity. In this case, there is no dc current flowing in the system as dc resistance is infinity. The constant phase element (CPE) rather than capacitance is usually used in modeling where surface under investigation lack homogeneity (Autolab Application Note, 2012)

(i) Constant phase element (CPE)

The impedance Z_{CPE} relating to constant phase element (CPE) is expressed as:

$$Z_{CPE} = A/(j\omega)^b \tag{3.52}$$

where A is a constant and b is an integer ($0 \le b \le 1$). When $b = 0$ the CPE acts as an ideal resistor, while it acts as an ideal capacitor when $b = 1$. When $b = 0.5$, the CPE is the equivalent of the so-called Warburg element, described below.

(j) Warburg impedance (Z_d)

Warburg impedance models the diffusion resistance of ionic species at the interface of ionic species. The impedance of a diffusion layer is obtained from;

$$Z_d = \frac{1}{Y_0\sqrt{j\omega}} \tag{3.53}$$

where Y_0 is the diffusion admittance. Warburg impedance contributes to phase change of 45° since identical real and imaginary impedance contributions characterize it.

The equivalent circuit of transmission line model used to fit impedance spectra of dye-sensitized solar cells is shown in Figure 3.13 (Jennings *et al.*, 2012). In this figure, blocks have been used to represent the TCO of photoelectrode, TiO_2 film, electrolyte, and the platinum-coated TCO of counter-electrode. The equivalent circuit shown in Figure 3.13 treats each nanoparticle of the film as a resistive element coupled to the electrolyte through the film/electrolyte interface (Gratzel, 2005).

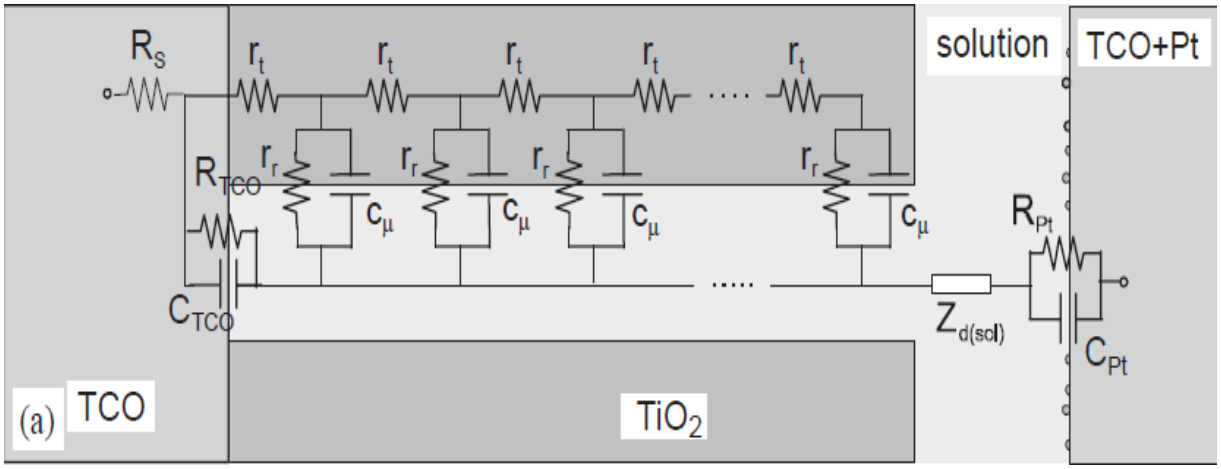

Figure 3.13: Equivalent circuit of Transmission line (TL) model used to fit impedance spectra of dye-sensitized solar cells (Sarker *et al.*,2014).

The elements of the equivalent circuit of transmission line model shown in the Figure 3.13 are defined as shown in following Table 3.2; (Fabregat-Santiago *et al.*, 2005).

Table 3.2: The description of elements of the equivalent circuit of Transmission line (TL) model (Fabregat-Santiago *et al.*, 2005).

Elements of EIS	Definition
R_S	Series resistance, accounting for charge transport resistance in the TCO glass;
z	Thickness of the TiO_2 film;
$R_t (= r_t z)$	Electron diffusion (transport) resistance between TiO_2 nPs and TiO_2 film and FTO glass;
$R_r (= r_r / z)$	Recombination resistance at the interface between the TiO_2 film and the liquid electrolyte;
$C_\mu (= c_\mu z)$	Chemical capacitance of the TiO_2 film representing change of electron density as a function of Fermi level;
Z_d	Warburg impedance representing the Nernst diffusion of tri-iodide species in the electrolyte;
R_{pt}	Charge-transfer resistance at the platinized TCO glass counter electrode;
C_{pt}	Interface capacitance at the platinized counter electrode and electrolyte interface;
R_{TCO}	Charge-transfer resistance for electron recombination from uncovered layer of the conducting glass (TCO) to electrolyte;
C_{TCO}	Capacitance at the triple contact TCO/TiO_2/electrolyte interface.

The impedance function of the transmission line model is given by following expression: (Fabregat-Santiago *et al.*, 2005; Wang *et al*., 2005)

$$Z = \left(\frac{R_t R_r}{1 + \left(j\omega / \omega_r \right)} \right)^{\frac{1}{2}} \coth\left[\left(\omega_r / \omega_d \right)^{\frac{1}{2}} \left(1 + j\omega / \omega_r \right)^{\frac{1}{2}} \right] \qquad (3.54)$$

where R_t is the electron diffusion resistance, R_r is the recombination resistance, $\omega_d = 1/ R_t C_\mu$ is the characteristic frequency of diffusion and $\omega_r = 1/R_r C\mu$ is the rate constant for recombination. The recombination resistance (R_t) is sum of resistance between the TiO_2 nanoparticles and resistance between TiO_2 film and the FTO glass substrate (Bisquert *et al*., 2009). It can be calculated from:

$$R_t = 3\left(R_{tot} - R_r\right) \qquad (3.55)$$

where R_{tot} is the total resistance of the cell.

The charge-transfer resistance (R_{pt}) at the platinum counter electrode is associated with the red-ox reaction involving I^-/I_3^- species (Wang *et al.,* 2005). Low R_{pt} values implies high catalytic activity for reduction of the red-ox couple. The chemical capacitance (C_μ) reflects the density and distribution of the electronic sites in the band gap of the semiconductor (Li *et al.,* 2012).

The Warburg impedance (Z_d) representing the Nernst diffusion of tri-iodide species in the electrolyte is described by following expression (Fabregat-Santiago *et al.,* 2011);

$$Z_d = R_d \frac{\tanh\left[\left(j\omega/\omega_d\right)^{\frac{1}{2}}\right]}{\left(j\omega/\omega_d\right)^{\frac{1}{2}}} \tag{3.56}$$

where R_d is diffusion resistance of ions in electrolyte and ω_d is characteristic frequency of diffusion.

The chemical capacitance (C_μ) can be calculated as follows, (Rahman *et al.*, 2015)

$$C_\mu = \frac{1}{\omega_r R_r} \tag{3.57}$$

The electron diffusion coefficient (D_n) is obtained from (Adachi *et al.,* 2006; Rahman *et al.*, 2015);

$$D_n = \left(\frac{R_r}{R_t}\right) z\,\omega_r \tag{3.58}$$

where R_r is recombination resistance, R_t is electron diffusion resistance, z is film thickness, and ω_r is the rate of recombination.

If $R_t > R_r$ the impedance of the diffusion-recombination follows the Gerischer impedance. This is not desired in DSSC because the photoinjected electron will be lost through recombination with the electrolyte before it reaches the TCO/TiO_2 interface.

The diffusion length (L_d) of electrons is a key parameter for enhancing conversion efficiency in a DSSC and can be calculated according to

$$L_d = \sqrt{(D_n \tau_n)} \tag{3.8}$$

The electron lifetime (τ_n) within the film is calculated using following expression (Luo *et al*., 2016);

$$\tau_n = \frac{1}{2\pi f_{\max}} \tag{3.59}$$

where $f_{\max}$ is the maximum peak frequency. In Figure 3.14, recombination resistance R_r is represented by R_{rec} and frequency ω_r represented by ω_{rec}.

Electrochemical impedance spectroscopy (EIS) measurements can be conducted with the instrument in potentiostatic mode and in combination with the frequency response analyzer (FRA). In potentiostatic mode, potential is controlled and current measured. In EIS measurements, the FRA module produces a small-amplitude sinusoidal wave with a user-defined frequency (NOVA, 2016). This excitation signal and the applied DC voltage are then superimposed on the cell. The response small-amplitude signal potential is then measured using the FRA module and impedance (Z) computed. Both the real and imaginary parts of impedance are computed together with phase angle shift between the excitation and response signals. The frequency response analyzer (FRA) module produces three main equivalent circuit elements; the series resistance (R_S), parallel resistance (R_P) and chemical capacitance ($C\mu$) or constant phase element (CPE).

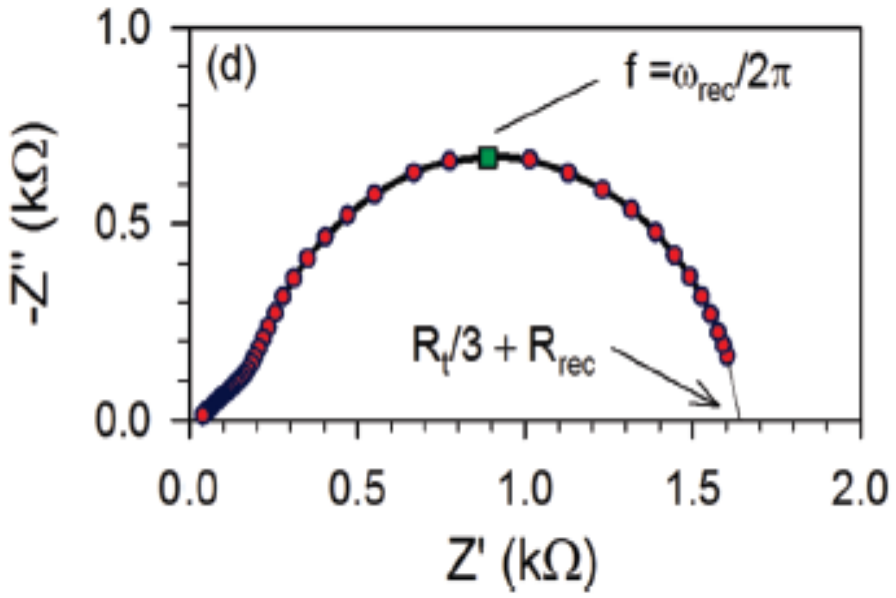

Figure 3.14: Characteristic Nyquist plot measured on a liquid electrolyte based DSSC showing the angular frequency at top of the arc that corresponds to the electron lifetime (Bisquert *et al*., 2009).

These circuit elements are related to combinations of the circuits elements shown in previous Figure (3.13) for the transmission line circuit model. For example, the series resistance (R_S) represents the sum of TCO resistance, charge-transfer resistance at counter electrode, and diffusion resistance in electrolyte, all of which produce a loss in the electrochemical potential of the cell outside the active layer (Fabregat-Santiago *et al*., 2011; Luo *et al*., 2016).

CHAPTER FOUR

MATERIALS AND METHODS

4.0 Introduction

This chapter contains the experimental procedures for fabricating and characterizing both the TiO_2/Nb_2O_5 composite films and the dye-sensitized solar cell (DSSC). The films were prepared using the electrophoretic deposition (EPD) method. Details on optimization of the EPD process-parameters, characterization of both composite films and the fabricated solar cell are presented.

4.1 Preparation of Transparent and Electrical Conducting Electrode

Commercially available transparent glass substrates (16 mm × 25 mm × 1 mm) coated with a conducting layer of fluorine doped tin oxide TiO_2 (FTO, $F:SnO_2$) (Pilkington, Hartford Glass Co. Inc., USA) having sheet resistances of 8 Ω/square were used as electrodes in EPD technique. These FTO glass substrates were cut into smaller pieces ($2.5mm \times 2.0mm \times 1.0mm$) and properly cleaned to remove contaminants and dust which could interfere with adhesion of deposited film on the glass surface. The cleaning of the substrate included the following steps: First, the FTO glass substrates were cleaned using detergent solution in a sonicator for 10.0 min. Secondly, the substrates were rinsed using distilled water. Finally, they were sonicated in acetone for 10.0 min after which they were rinsed using distilled water in ultrasonic bath. These glass slides were subsequently connected to EPD assembly as anode and cathode for film deposition.

4.2 Preparation of the EPD Suspension

The experimental EPD suspension was created by dispersing commercial titanium dioxide (TiO_2) nanopowder (CAS No. 13463-67-7, Aldrich) and Niobium (V) oxide (Nb_2O_5) nanopowder (CAS No. 1313-96-8, Acros Organics BVBA, Belgium), in 2-propanol (IPA: Isopropyl alcohol) (Scharlau Chemie) contained in a Pyrex beaker. Varied amounts of both TiO_2 and Nb_2O_5 powders were weighed and poured into a Pyrex beaker containing 40mL of

2-propanol to form the EPD suspension. In each case, the two metal oxide powders were mixed in equal ratios (1:1). In addition, $5x10^{-5}$M magnesium nitrate hexahydrate pellets ($Mg(NO_3)_2 \cdot 6H_2O$ 99.9%, Aldrich) were weighed and added to the EPD cell to form an electric charging system thereby controlling the zeta potential of the suspension as reported by (Bandy *et al*., 2011; Lee *et al*., 2011). The suspension was then stirred for 30 minutes using a power sonicator (Sonic 405) before it was used in the EPD equipment for film deposition. The acidic (or basicity) levels of the suspension were determined by measuring the pH values using a pH meter.

4.3 Electrophoretic Deposition of the TiO_2/Nb_2O_5 Composite Films

The EPD apparatus included EPD cell (Pyrex glass beaker), DC power supply (Thurlby Thadar TS30225), electrodes consisting of FTO coated glass substrates and equipment to support the electrodes when partially immersed in the suspension. The EPD equipment was set up as shown in Figure 4.1.

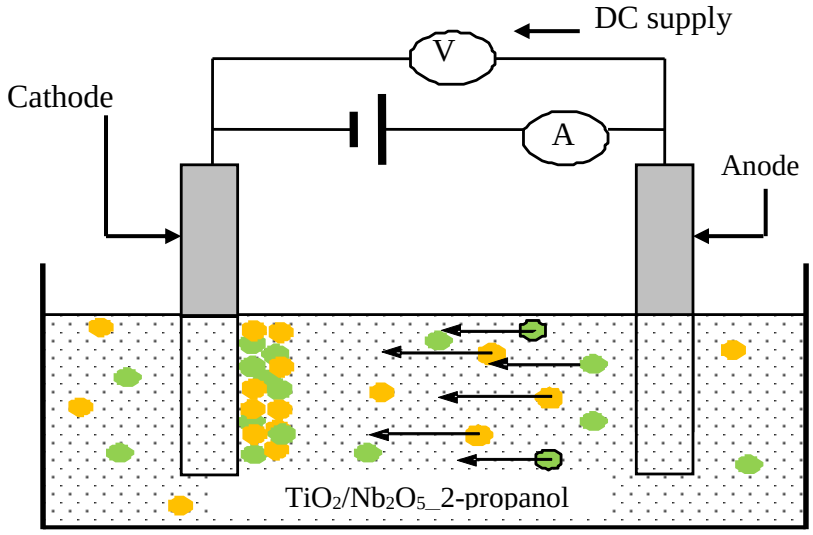

Figure 4.1: A schematic drawing of the EPD setup showing the two FTO coated glass slides partially immersed into TiO_2/Nb_2O_5_2-propanol suspension in a beaker. also shown are the ammeter (A) and voltmeter (V) and applied DC voltage.

The FTO-coated glass substrate (cathode and anode) were arranged with conducting sides facing each other in a parallel-plate configuration, separated by 1.2 cm, and partially immersed in suspension made up of TiO_2 and Nb_2O_5 powders, magnesium nitrate, and

2-propanol. A DC electric voltage of 35V was then applied across the electrodes for between 60s and 180s. A film was seen to form on the cathode implying that positive charges formed on the surfaces of TiO_2 and Nb_2O_5 particles when 2-propanol and magnesium nitrate were used for the suspension. After the desired deposition time had elapsed, the film coated glass substrate was slowly pulled out of the suspension thereby minimizing drag forces that could affect quality of the film. The films were then annealed at 450°C for 6h with a heating rate of 5°C per minute. The furnace was then turned off and the substrate allowed to cool gradually to room temperature (25°C).

Determination of (a) optimum mixing ratio of Nb_2O_5 and TiO_2 and (b) the particle concentration in suspension for film formation.

The mixing ratios (by mass) of solid in the suspension can play an important role for the many component electrophoretic deposition (EPD). Then the particle concentration (g/L) of nanoparticles for use in film formation was established. The following section 4.4 describes the process of establishing optimum mixing ratios (by mass) of niobium (v) oxide and titanium dioxide nanopowders i.e., TiO_2:Nb_2O_5 used in film deposition. Section 4.5 outlines the process of determining the particle/powder concentration (g/L) in fixed ratio for preparing the EPD suspension.

4.4 Determination of optimum mixing ratio of Nb_2O_5 and TiO_2 for Film Formation

The optimum ratio of Nb_2O_5 & TiO_2 nanoparticles for use in fabricating the composite films was determined from Hall effect measurements. The Hall Effect measurements involved establishing the variation of the Hall voltage (V_H) with particle concentrations of different ratios of TiO_2 and Nb_2O_5 particles in suspension. The optimum ratio of TiO_2 and Nb_2O_5 particles forming film with largest Hall voltage was chosen. The optimum ratio was maintained constant in all subsequent film depositions. Thus powder/particle concentrations (g/L) were prepared by mixing fixed ratios of TiO_2 and Nb_2O_5 particles but varying the amounts (in g) of particles in suspension.

4.5 Optimization of Particle Concentration in EPD Suspension

Varied amounts (0.01 g to 0.03 g) of both TiO_2 and Nb_2O_5 powders/particles at fixed mass ratio established according to description in preceding section, were weighed and poured into a Pyrex beaker containing fixed volume (40mL) of 2-propanol to form the EPD suspension. 5mM Magnesium nitrate hexahydrate ($Mg(NO_3).6H_2O$) was added into the suspension that was then stirred for 30 min using a sonicator (Power Sonic 405). The electrodes were partially immersed in the suspension and a DC voltage applied across them for specified duration. The films deposited using varying particle concentrations were then annealed and subjected to UV-Vis-NIR spectrophotometer for measurement of transmittance and reflectance in wavelength range of $300 \leq \lambda \leq 3000$ nm. The plots of transmittance and reflectance versus wavelength were obtained. Transmittance data was analyzed and used to plot transmittance versus particle concentration curves. From these curves, the particle concentration that produced films of the highest transmittance were obtained.

4.6 Optimization of DC Applied Voltage for EPD

The suspensions with fixed particles ratio and concentrations (e.g., 0.25g/L: 0.25 g/L) for TiO_2 and Nb_2O_5 powders/particles in 2-propanol were prepared and used in determining the optimum deposition voltage. Using the EPD method- the electrodes were partly dipped in the EPD suspension and varying applied voltages ranging from 25V to 60V were applied for 90s. The voltage was supplied by a DC dual faced power supply. The deposited films were then subjected to transmittance measurements using UV-Vis-NIR spectrophotometer and graphs of transmittance against wavelength plotted. The obtained transmittance data was then plotted against voltage to determine the optimum applied voltage that produced films of the highest transmittance at constant particle concentration and constant deposition time.

4.7 Optimization of Deposition Time for EPD

In order to optimize deposition time, the EPD suspensions of fixed particles ratio and concentrations (e.g., 0.25g/L: 0.25 g/L) for TiO_2 and Nb_2O_5 powders/particles in 2-propanol were prepared and applied in film deposition for varied deposition times ranging from 60 s to

300 s. A constant applied DC voltage of 35V was applied across the electrodes partially immersed in the suspension The deposited films were then subjected to transmittance measurements using UV-Vis-NIR spectrophotometer. In this case the graphs of transmittance against deposition times were plotted. The transmittance data was then plotted against time to determine the optimum deposition time.

4.8 Measurement of Film Thickness

The Film thickness (z) was measured using surface profilometer. The films were then subjected to electrical, optical, morphological and structural characterization.

4.9 Characterization of TiO_2/Nb_2O_5 Composite Films Deposited by EPD Technique

Physical characteristics of the deposited TiO_2/Nb_2O_5 composite films impact on the performance of the dye-sensitized solar cell. The TiO_2/Nb_2O_5 composite films deposited by the electrophoretic technique were characterized using appropriate analysis techniques for morphological, structural, electrical and optical properties.

4.10 Optical Characterization

Optical characterization of the TiO_2/Nb_2O_5 composite thin films was carried out using Shimadzu-DUV spectrophotometer. A baseline on spectrophotometer was recorded prior to the measurement to calibrate the instrument. Spectroscopic transmission measurements of the thin films were determined at normal incidence and at wavelengths in the range $200nm \leq \lambda \leq 3200nm$. Optical parameters like refractive index (n), extinction coefficient (k), dielectric constant (ε), optical band gap energy E_g, and Urbach energy (E_U) were computed using primarily the Tauc equation and relevant equations discussed in chapter 3.

4.11 Electrical Characterization

The Hall Effect equipment and the four point probe were used to conduct electrical characterization of the films. The electrical characteristics of a photoelectrode indicate the suitability of a film in facilitating electron injection into and transport through the photoelectrode. The following is a detailed description of application of Hall effect and four point probe techniques.

(a) The Hall Effect measurement

The Hall Effect measurements involved measurements of the Hall voltage (V_H) and current (I_x) for constant applied magnetic field (B_y). The Hall voltage was measured in a perpendicular direction to the magnetic field and to the direction of an electric current flowing through the semiconductor using the configuration shown in Figure 4.2. The constant direct-current and power supply meters were used to measure the supplied electric current (I_x) and Hall voltage (V_H) respectively.

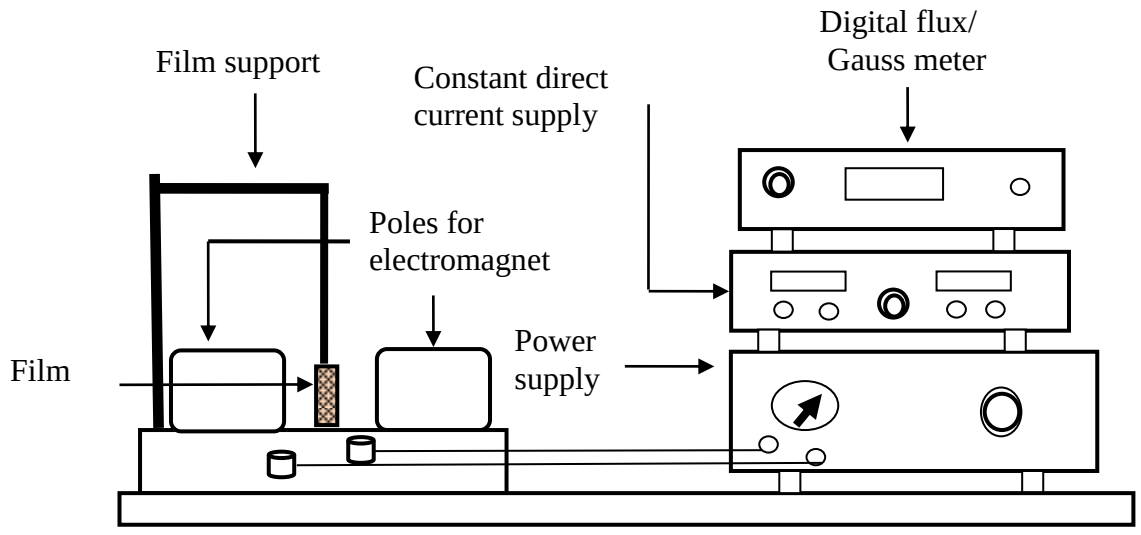

Figure 4.2: Schematic drawing of Hall Effect measurement showing meters that provide current and magnetic fields and clamp which support probes and the film.

The uniform magnetic field intensity (B_y) was measured using the digital flux/gauss meter (Figure 4.2). Each sample was mounted individually onto a printed circuit, clamped and attached to a stand placed between electromagnetic poles. The Hall voltage and current values were measured and recorded for magnetic field of 3G (=0.0003T) at room temperature

(25°C). The data and necessary equations were used to determine the Hall coefficients, type of majority carriers, and charge carrier density in the semiconductor film.

(b) The Four point probe

The sheet resistance of the TiO_2/Nb_2O_5 composite thin films was measured using the four point probe, model SRM-232 (Figure 4.3). In a four-point probe, the four probes are placed in a straight line. The voltage is measured across the inner probes while current is measured across the outer probes. A four-point probe operates by passing a calibrated constant current source of 4.53mA through the two outer tips (Figure 4.3). The probe was manually operated by pressing the 4-point probe to the film. A current source was activated and the sheet resistance (R_s) values measured and displayed on the 16 digit LCD front panel display. The sheet resistance was used in equation (3.36) to determine the film resistivity (ρ).

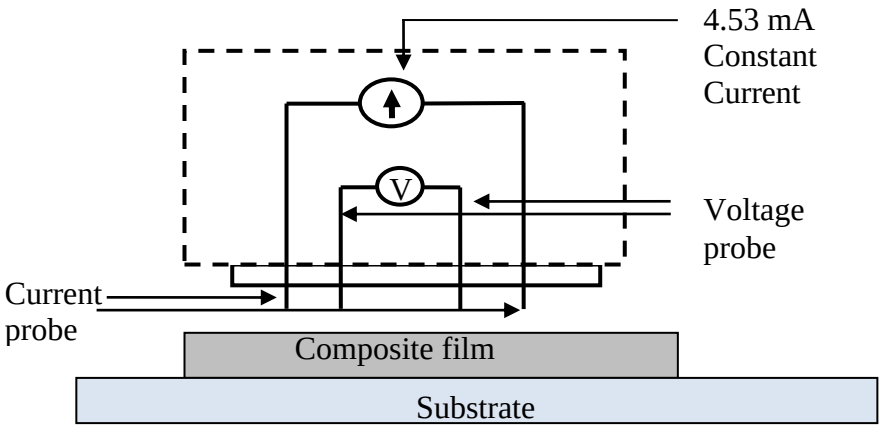

Figure 4.3: Functional block diagram of SRM-232 four point probe showing four probes: inner two for measuring voltage and outer two for measuring current.(After Bridge Technology).

4.12 Morphological Characterization

The surface morphology of TiO_2/Nb_2O_5 composite electrode thin films was investigated using the scanning electron microscope (SEM) model S4100 HITACHI™ to determine the quality of the deposited films. No prior treatment was required before the scanning process since all the films were coated on FTO glass substrate. The SEM images were taken at varied magnifications that ranged from $\times 1{,}000$ to $\times 30{,}000$ and at a constant accelerating potential of 5kV.

4.13 Structural Analysis

Structural analysis of TiO_2/Nb_2O_5 composite electrode thin films was conducted using Shimadzu X-Ray Diffractometer with Cu Kα (k=15.418nm) radiation in the scanning range of 2θ from 0 to 80° to investigate crystalline material structure, including crystallite size and atomic arrangement. For any particular Bragg angle (source and detector fixed), the specimen was rotated such that the incident and diffracted beam made different angles to the specimen surface (the angle between them remaining fixed at 2θ). The XRD pattern was analyzed using the International Center for Diffraction Data (JCPDS card) (Feist & Davies, 1992; Frevel, 1955 (in Liu, *et al*., 2015)), Appendix A & B). Crystallite size is usually taken as the cube root of the volume of a crystallite. The crystallite size (D) was examined from XRD peaks based on the Scherer's equation, (4.1).

$$D = \left(0.94\,\lambda\right) \Big/ \left(\Delta w \cos\,\theta\right) \tag{4.1}$$

where λ is the wavelength of X-ray radiation equal to 0.15406 nm for Cukα radiation, θ is the Bragg' diffraction angle, and Δw is the half-peak width of the X ray diffraction lines (Khoby-Shendy *et al*., 2012). The half-peak width (Δw) is inversely proportional to crystallite size (D). However, the half-peak width is difficult to calculate for many line X-ray diffraction lines due to the dimensions involved.

4.14 Preparation of Components and Assembly of DSSCl

Subsequent to electrophoretic deposition of TiO_2/Nb_2O_5 composite films, the films were chemisorbed with dye and used to assemble the DSSC. The procedure for preparing the dye, electrolyte and counter electrodes is described in the following subsection.

(a) Ruthenium dye staining of composite film

A synthetic Ruthenium-dye solution of 0.5 mM was prepared according to standard procedure.

Ru-N719 whose chemical name is cis-diisothiocyanato-bis (2,2'-bipyridyl-4,4'-dicarboxylato) ruthenium(II) bis(tetrabutylammonium) (CAS 207347-46-4) was purchased from Sigma Aldrich and applied without further purification. The short formula for Ru-719 dye is $RuL_2(NCS)_2$:2TBA where (L=2,2'-bipyridyl-4,4'-dicarboxylic acid; TBA=tetrabutyl ammonium). The dye solution was prepared by dissolving 6 mg of Ru-719 in 10 mL of ethanol and sonicated until thoroughly mixed. The electrophoretically deposited TiO_2/Nb_2O_5 composite films were preheated to 200.0°C for 10.0 minutes to remove adsorbed water. They were then partially scrapped off to form an active area of 0.49 cm^2. The films were immersed into the dye solution whilst hot (~80°C) to prevent readsorption of water. The soaking of the electrode in dye solution was maintained for 24 hours to enable proper dye chemisorption. After the dye sensitization, the photoelectrodes were rinsed with ethanol to detach the unabsorbed dye molecules after which they were immediately used as DSSC photoanodes.

(b) Preparation of the electrolyte

An electrolyte is required in a dye-sensitized solar cell to complete the circuit between the sensitized photoelectrode and the counter electrode. In this work, an iodide/triiodide (I^-/I_3^-) red-ox couple based electrolyte prepared by dissolving: 0.101 g (0.04 M) iodine (CAS 7553-56-2), 0.134 g (0.1M) lithium iodide (CAS 10377-51-2), and 1.477 g (0.5M) tetra-n-butylammonium iodide, in 10 mL of acetonitrile (CAS 75-05-8) was used. Two drops of 4-tert-butylpyridine (CAS 3978-81-2) were added to the electrolyte to augment the voltage output in the same manner as described by Yang, (2011).

(c) Preparation of the Counter electrode

The platinum-coated counter electrodes (CEs) were fabricated by placing drops of 5 mM hexachloroplatinic acid (H_2PtCl_6) (Fluka) on a cleaned FTO glass. The acid spread out evenly covering the whole FTO-glass surface. The platinum film was obtained after heating the acid-wet FTO glass at 450°C for 45 minutes and cooling the CE to room temperature. Presence of platinum was confirmed by placing a drop of hydrogen peroxide on the glass slide resulting in formation of bubbles.

(d) Assembling the dye-sensitized solar cell

The dye-sensitized TiO_2/Nb_2O_5 composite photoelectrode was placed over platinum coated counter electrode to form a sandwich arrangement. The edges of the cell were sealed by hot

pressing the two electrodes together with a 25-µm thick hot-melt gasket of Surlyn monomer placed between them. The electrolyte containing iodine/tri-iodide red-ox couple was inserted inside the sandwich arrangement via two small (0.5mm) holes drilled in the counter electrode (CE). Consequently, the sealing of holes in CE was done using a small piece of microscope covering plastic. The schematic diagram and photograph of assembled solar cell are shown in Figures 4.4 and 4.5 respectively.

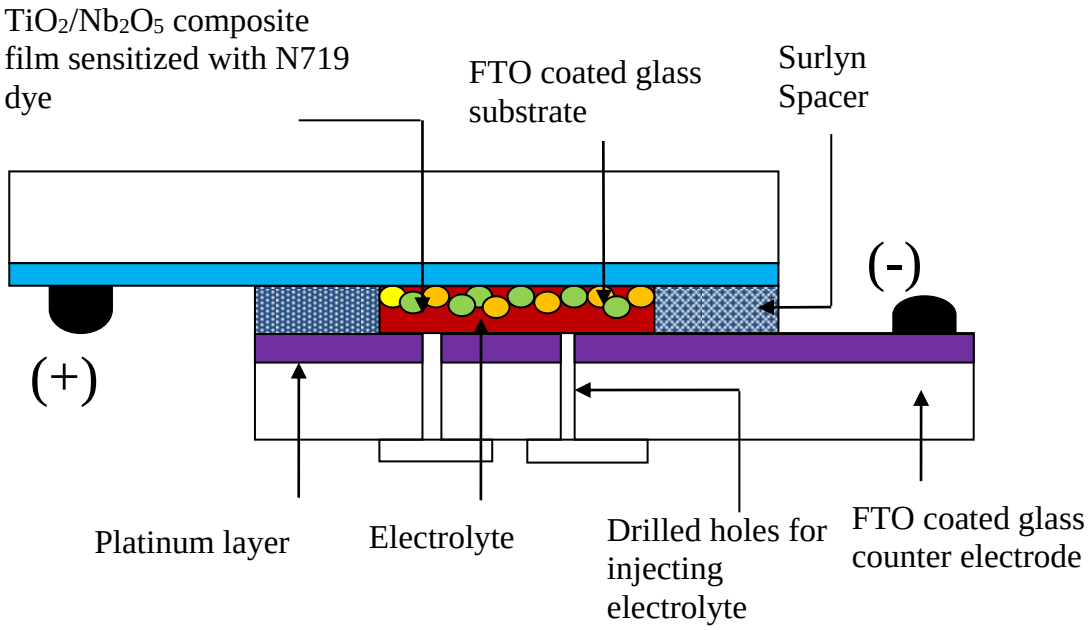

Figure 4.4: Schematic diagram of assembled dye-sensitized solar cell employing TiO_2/Nb_2O_5 composite electrode film.

Figure 4.5: Photograph of the assembled dye-sensitized solar cell based on TiO_2/Nb_2O_5 composite electrode film showing predrilled holes through which electrolyte was injected to cell.

4.15 Current-Voltage (I-V) Characterization of DSSC

The photoelectric current-voltage (I-V) characteristics of the cell were determined using a digital source meter (Keithley-2400) under simulated sunlight of one sun. The simulated light was provided by a solar simulator which closely approximates the solar radiation using the light from a xenon ultra high pressure lamp through various filters. The currents and voltages generated by the solar cell for diverse load resistances were measured under a set of standard test condition for solar cells using the Keithley meter and computer (Jose *et al.,* 2009). These test conditions as outlined in international standards, e.g., ASTM E927-05 documents essentially specify that the power density of the light illuminating the cell should be 100 mW cm^{-2}, temperature of 25°C, and the radiation condition should be AM 1.5 global for terrestrial applications. The active area of the cell was 0.49 cm^2.

The short-circuit current density (J_{SC}), open-circuit voltage (V_{OC}), fill-factor (*FF*), and energy conversion efficiency **(** η **)** were derived from the I-V curves and recorded. In addition, tables with photovoltaic parameters for DSSCs employing electrophoretically deposited photoelectrode for varied deposition time, applied voltage and particle concentration in suspension were obtained.

4.16 Electrochemical Impedance Spectroscopy (EIS) Measurement of DSSC

The instrumentation required for EIS includes potentiostat, impedance analyzer and software for data acquisition and analysis. Figure 4.6 shows the experimental set up for EIS measurements on dye-sensitized solar cells (DSSC). The calibrated photodiode holder fitted with two sliding clamps was used to fix the DSSC onto the holder. The cell was then illuminated with red light (λ= 627nm) supplied by a light emitting diode (LED) powered by Autolab LED driver (Figure 4.6). The spectra was obtained under 0.1 sun illumination at 0.5V direct current biasing. An AUTOLAB (PGSTAT204) equipment (Autolab, Switzerland) in potentiostatic mode, connected to a computer was used to power the photodiode and the LED driver. EIS -measurements were performed on the cell with the AUTOLAB instrument joined with the frequency response analyzer (FRA32M) module. During the EIS measurement, the FRA32M module (0.014V, 50Ω, 3906.9Hz) supplied a single-sine shaped voltage of 5 to 15 mV. Upon application of a small-amplitude sinusoidal perturbation

potential of 10mV at fixed frequency, the sinusoidal current response was measured using the NOVA software and the impedance at each frequency computed.

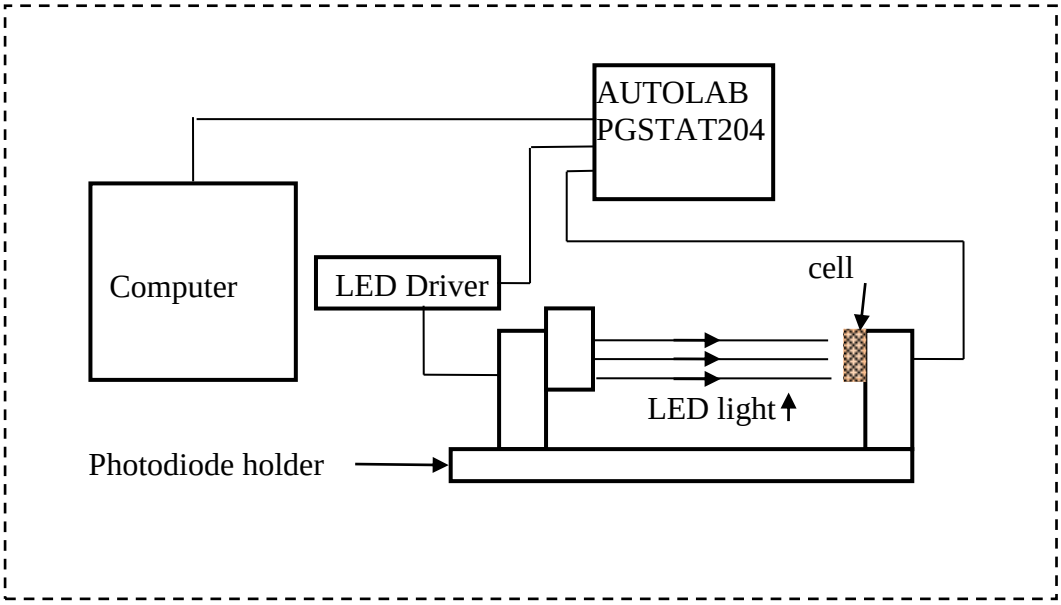

Figure 4.6: Electrochemical impedance spectroscopy measurement set up showing Autolab connection to LED driver and the DSSC.

The measurements of impedance was repeated for frequencies supplied in the range of 10kHz (highest applied) to 0.1Hz (lowest supplied). The frequencies were scanned at 5-10 measurements per decade. The biasing DC voltage of 0.5V was used in the EIS - measurements because this value approximated the V_{OC} of the fabricated solar cells. Open circuit voltage is an important parameter in I-V characterization of solar cells. As such, the impedances of the cells at biasing potential of around V_{OC} was of interest. The real part and imaginary parts of the impedance were then plotted to yield the Nyquist plot used to analyze the solar cell. The results were then analyzed using the equivalent circuit as described in following section.

The three main equivalent circuit elements; the series resistance (R_S), parallel resistance (R_P) and chemical capacitance (C_μ) or constant phase element (CPE)were extracted from EIS measurements under illumination at open circuit condition of 0.5V DC, by frequency response analyzer (FRA) module coupled with NOVA software in Autolab instrument (galvanometer). The EIS measurements were analyzed by fitting them with an equivalent circuit constructed using various circuits elements provided in the NOVA software. NOVA

software analysis tools provides an electrochemical circle fit tool, that is used in estimating the parameters of the equivalent circuit. For better fitting of theoretical data, all capacitor elements were replaced by constant phase element (CPE or Q). Impedance data was fitted in the electrochemical circle option using a predefined R(RQ) equivalent circuit. The electrochemical circle option tool uses the measured data points of the circular portion of Nyquist plot to calculate the values of the elements of the equivalent circuit. Electron recombination lifetime (τ_n) was estimated from maximum frequency values in Bode plot using equation 3.59.

CHAPTER FIVE

RESULTS AND DISCUSSION

This chapter presents the experimental results and discussion related to (i) optimization of the electrophoretic deposition (EPD) parameters, (ii) morphological, structural, electrical, and optical characterization of the TiO_2/Nb_2O_5 composite electrode thin films and (iii) the current-voltage (I-V) and electrochemical impedance spectroscopy (EIS) characterization of the fabricated dye-sensitized solar cell.

5.0 The pH and Optimization of Ratios of TiO_2 and Nb_2O_5 Particles in Suspension

The TiO_2/Nb_2O_5 composite electrode thin films were successfully deposited by electrophoretic technique. Similar negative (-ve) charges formed on both TiO_2 and Nb_2O_5 particles suspended in 2-propanol and contributed to film formation on EPD cathode electrode (cathodic deposition). The pH values of suspension were found to influence the deposition of nanocrystalline TiO_2/Nb_2O_5 composite electrode thin films. For $pH \geq 5$, the no observable deposition took place after 3 minutes. Optimum pH for TiO_2/Nb_2O_5 composite thin films was 4.9, a value that was consistent with that (4.7) obtained by Teleki *et al*., (2006) for deposition of nanocrystalline TiO_2 film. Although each type of particle has same negative charge developed on its surface, the particles could follow diverse deposition rates based on the mass ratio of powders in suspension. Thus, optimization of mixing ratio by mass of the powders was determined using Hall effect results.

Figure 5.1 shows a plot of Hall coefficients versus the increasing proportion of Nb_2O_5 forming ratio of Nb_2O_5 and TiO_2 in suspension. The negative polarity of the Hall coefficient values indicated that majority carriers in the TiO_2/Nb_2O_5 composite films were n-type (electrons). This polarity could have been caused by incorporation of Nb^{+5}, and O^{-2} ions in the composite. The bulk sized TiO_2 is an n-type semiconductor due to presence of titanium vacancies in TiO_2 and due to oxygen vacancies which could be treated as donor type defects. However, the many attributes of nanomaterials deviate from those of the same materials in bulk. Niobium (v) oxide (Nb_2O_5) is reported to become an n-type semiconductor at lower

oxygen content. The Hall coefficient (R_H) is known to be large for high Hall mobility of charges (Jewett & Serway, 2010).

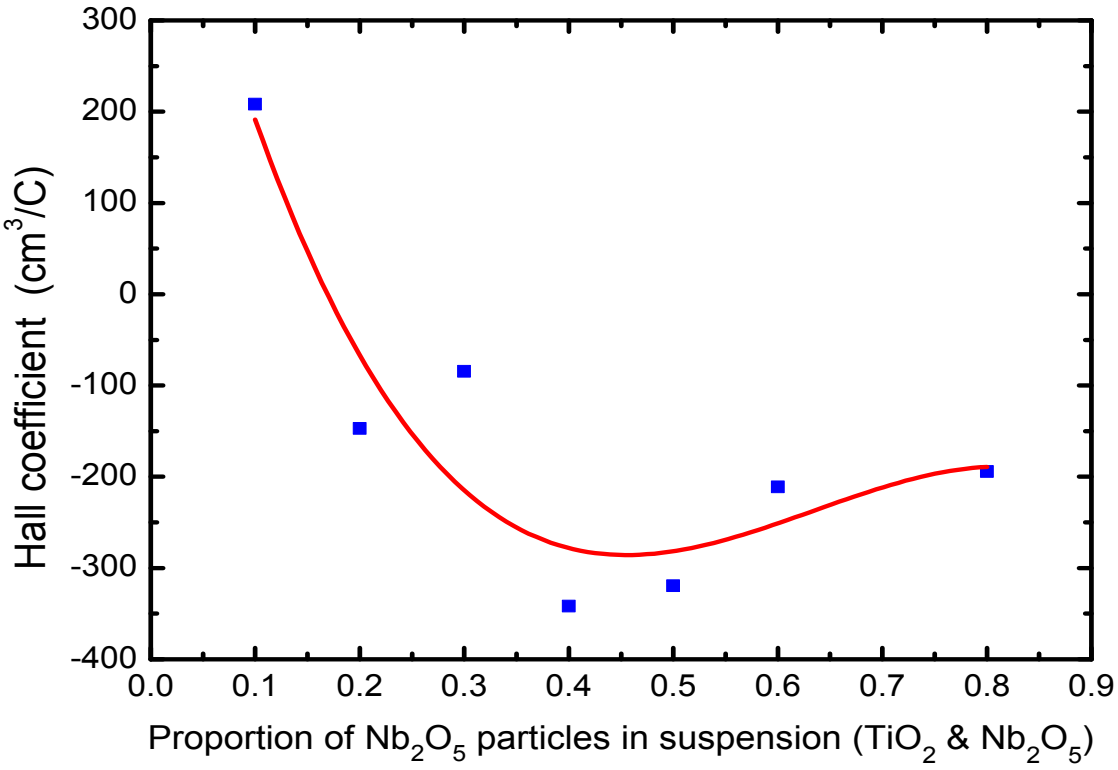

Figure 5.1: Hall coefficient versus proportion of Nb_2O_5 by mass in suspension. Proceeding from left to right of the figure, proportion of Nb_2O_5 increased while that of TiO_2 decreased. Films deposited using EPD technique using 35V, and deposition time of 90s.

In preparation of suspension used to deposit the films of Figure 5.1, the mixing of nanoparticles was carried out by increasing the proportion by mass of Nb_2O_5 (from 0.1 to 0.9) while decreasing proportion of TiO_2 (from 0.9 to 0.1). The largest value of absolute Hall coefficient (R_H) was obtained for proportion 0.45 (of Nb_2O_5) and 0.55 (of TiO_2) in suspension. For experimental purpose of measuring TiO_2 and Nb_2O_5 by mass during the film preparation, the ratio of 0.45: 0.55 was approximated to 0.5 : 0.5 or 1 : 1 (TiO_2:Nb_2O_5).

5.1 Optimization of Concentration of TiO_2 and Nb_2O_5 Particles in Suspension

Figure 5.2 shows plots of (a) transmittance against wavelength, (b) peak transmittance against particle concentration and (c) film thickness against particle concentration for TiO_2/Nb_2O_5 composite films.

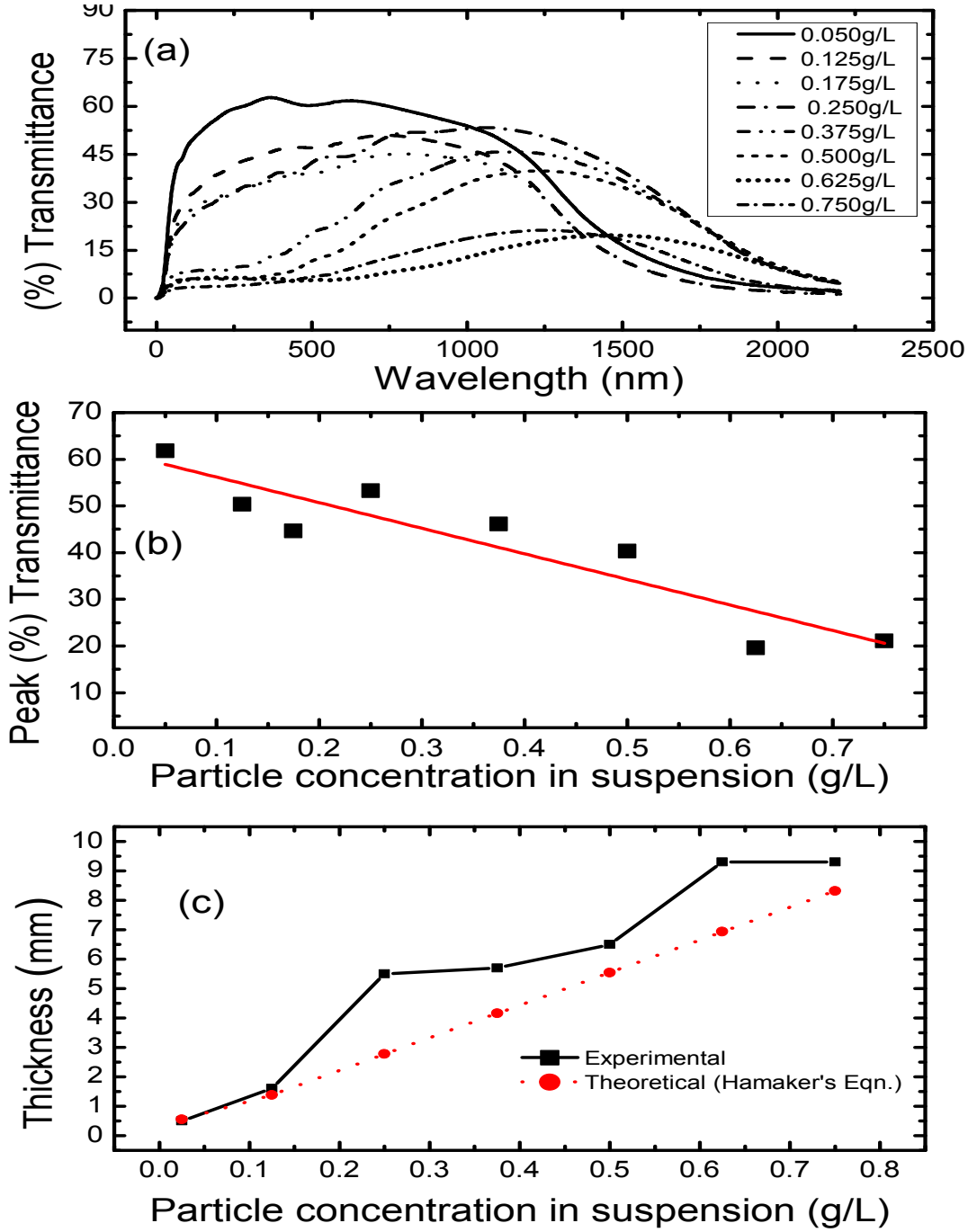

Figure 5.2: (a) Variation of transmittance with wavelength, (b) variation of peak transmittance with particle concentration and (c) film thickness versus concentration for TiO_2/Nb_2O_5 composite films deposited by EPD technique using applied voltage of 35V and deposition time of 90s.

In preparing different particle concentrations, equal amounts (in g) of the nanopowders of both Nb_2O_5 and TiO_2 were mixed in 2-propanol thus maintaining a constant mass ratio of 1:1 in suspension for electrophoretic film deposition. In EPD preparation of each film, deposition time of 90 s and the applied DC voltage of 35V were used. The concentration of TiO_2 and Nb_2O_5 particles ranged from 0.05 g/L to 0.75 g/L. From Figure 5.2a, it is observed that the deposition of nanostructured TiO_2/Nb_2O_5 composite film reduced transparency of the conducting electrode (FTO) over near-infrared and the entire visible region of solar spectrum. Plain FTO coated glass (0 g/L) had the highest transmittance (~ 80%). Further it can also be seen in Figure 5.2a that peaks of maximum transmittance decreased and shifted towards the long wavelengths region as the particle concentration in suspension, used for films deposition, was increased. This shifting and reduction of peaks could be explained in terms of reduction of photon energy $(h\upsilon)$,

$$E = h\upsilon = hc/\lambda \tag{5.1}$$

through the absorption of some photons in the composite film through which they traversed. Thus, the transmitted photons had reduced energy (and large wavelength) leading to the spectral shift. Thicker films obtained for higher particle concentrations were responsible for greater reduction of the energy of the photons transmitted through them than did the thinner films (Figure 5.2c). Thus the energy of transmitted photons reduced in thicker films which accounts for the shift in maximum transmittance peaks towards longer wavelengths. Figure 5.2b shows the variation of peak transmittance with particle concentration is, while Figure 5.2c shows the variation of the film thickness with particle concentration. From Figure 5.2c, it is noted that thickness of the films increased with particle concentration. Thus the decrease of transmittance with particle concentration is due to the increase in thickness of the films and hence absorption. Light transmission through a thick film experiences enhanced attenuation. These findings were consistent with observations of Miyasaka and Kijitori, (2004) that high particle concentration leads to particle aggregation in the deposited film. Hamaker's equation;

$$m \propto CVt \tag{5.2}$$

with the proportionality constant, $0.0701\, m^4 Kg^{-1} V^{-1} s^{-1}$ showed that the predicted film thicknesses (mass/area) of the composite films varied linearly with increasing particle

concentration. The experimentally obtained thicknesses were slightly higher than the theoretically obtained thicknesses. The difference in thicknesses was attributed to possible non ideal stability of suspension with tendency to settle down unlike the prediction by Hamaker's equation. Although films deposited from concentrations less than 0.25 g/ L produced high transmittances, they barely formed films of any appreciable thickness useful for dye adsorption for application in DSSCs. Visual inspection showed that the films corresponding to 0.25 g/L concentration had the best quality and cracks free films. Thus, 0.25 g/L was chosen as optimum EPD particle concentration for film preparation.

5.2 The Optimization of Deposition Time

Figure 5.3 shows plot of (a) transmittance versus wavelength, (b) peak transmittance versus deposition time and (c) film thickness versus deposition time for TiO_2/Nb_2O_5 composite films deposited by EPD technique at applied voltage of 35 V and particle concentration of 0.25 g/L in the suspension of 2-propanol. The peaks of maximum transmittance decreased and shifted towards the long wavelengths region for films deposited using increased EPD deposition time. This reduction and shifting could be attributed to reduced energy (and large wavelength) of the transmitted photons resulting from absorption of part of the energy by the film.

The variation of peak transmittance with deposition time is shown in Figure 5.3b while the variation of film thickness with deposition time is shown in Figure 5.3c. It is noted, from Figure 5.3c, that thickness of the films increased with deposition time. Thus, the decrease of transmittance with deposition time is due to increase in thickness of the films and hence light absorption. The typical TiO_2 film layer thickness for DSSCs range between 5 and 15μm (Jarernboon *et al*., 2009). The TiO_2/Nb_2O_5 composite films electrophoretically deposited for 90 s ($5.5\,\mu m$), produced the highest transmittance of 53% at λ = 1300 nm. In addition, the best quality films from visual inspection correspond to deposition time of 90s. Figure 5.3c shows the variation of thickness with deposition time for the composite films electrophoretically deposited at 35 V and 0.25 g/L. According to theoretical (Hamaker's equation) prediction of film thickness formation, the thickness varied linearly with deposition time. The equation assumes complete stability of suspension which shows no tendency to

settle down. The slight deviation from predicted linear relationship was attributed to suspension instability.

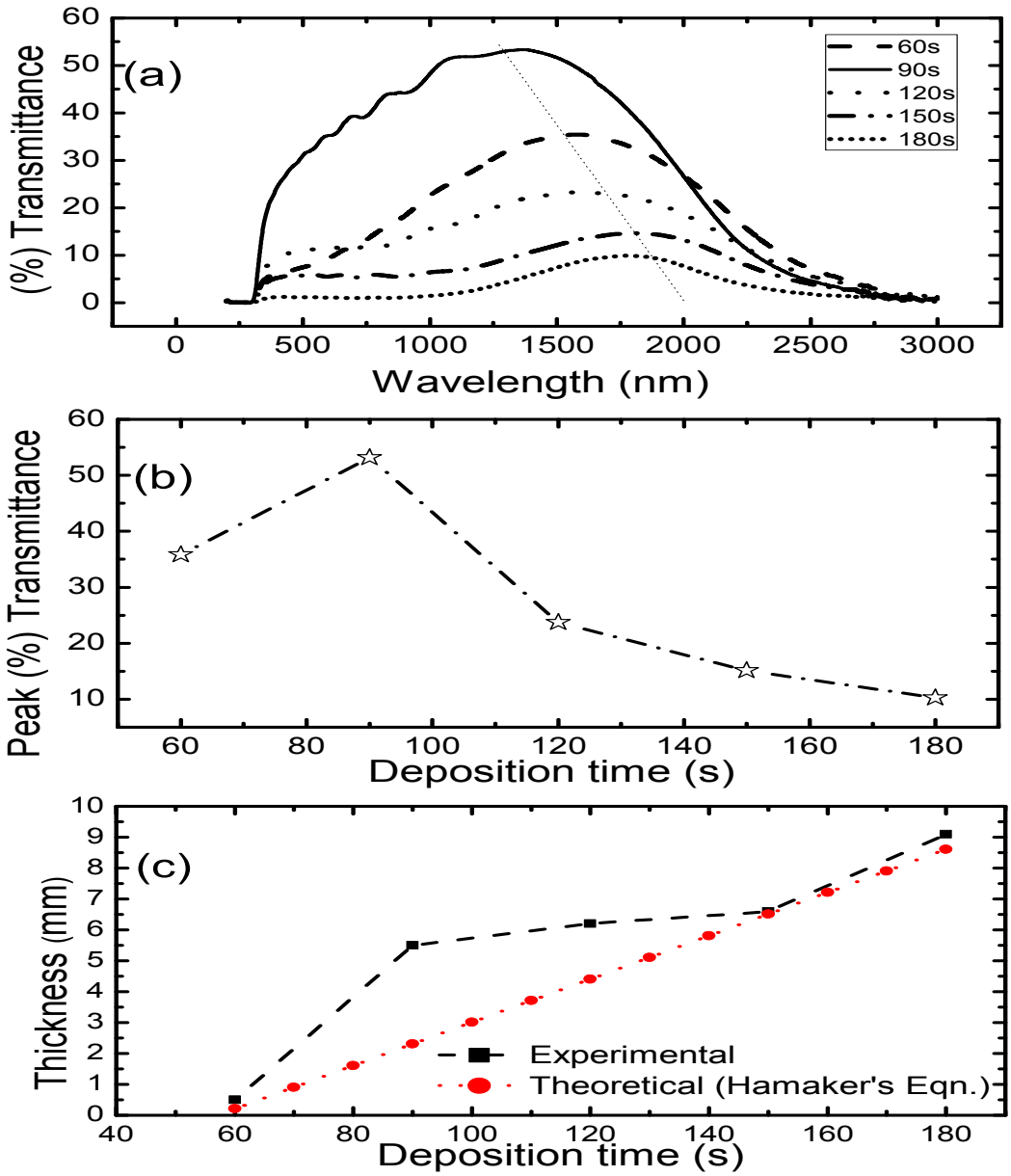

Figure 5.3: (a) Variation of transmittance with wavelength, (b) variation of peak transmittance with deposition time and (c) thickness versus deposition time for TiO_2/Nb_2O_5 composite films deposited by EPD technique at applied voltage of 35V and particle concentration of 0.25g/L in 2-propanol suspension.

5.3 Optimization of Applied Voltage

Figure 5.4 shows plots of (a) variation of transmittance with wavelength, (b) variation of peak transmittance with applied voltage, and (c) variation of film thickness with applied voltage for TiO_2/Nb_2O_5 composite films deposited by EPD method using particle concentration of 0.25g/L and deposition time of 90s.

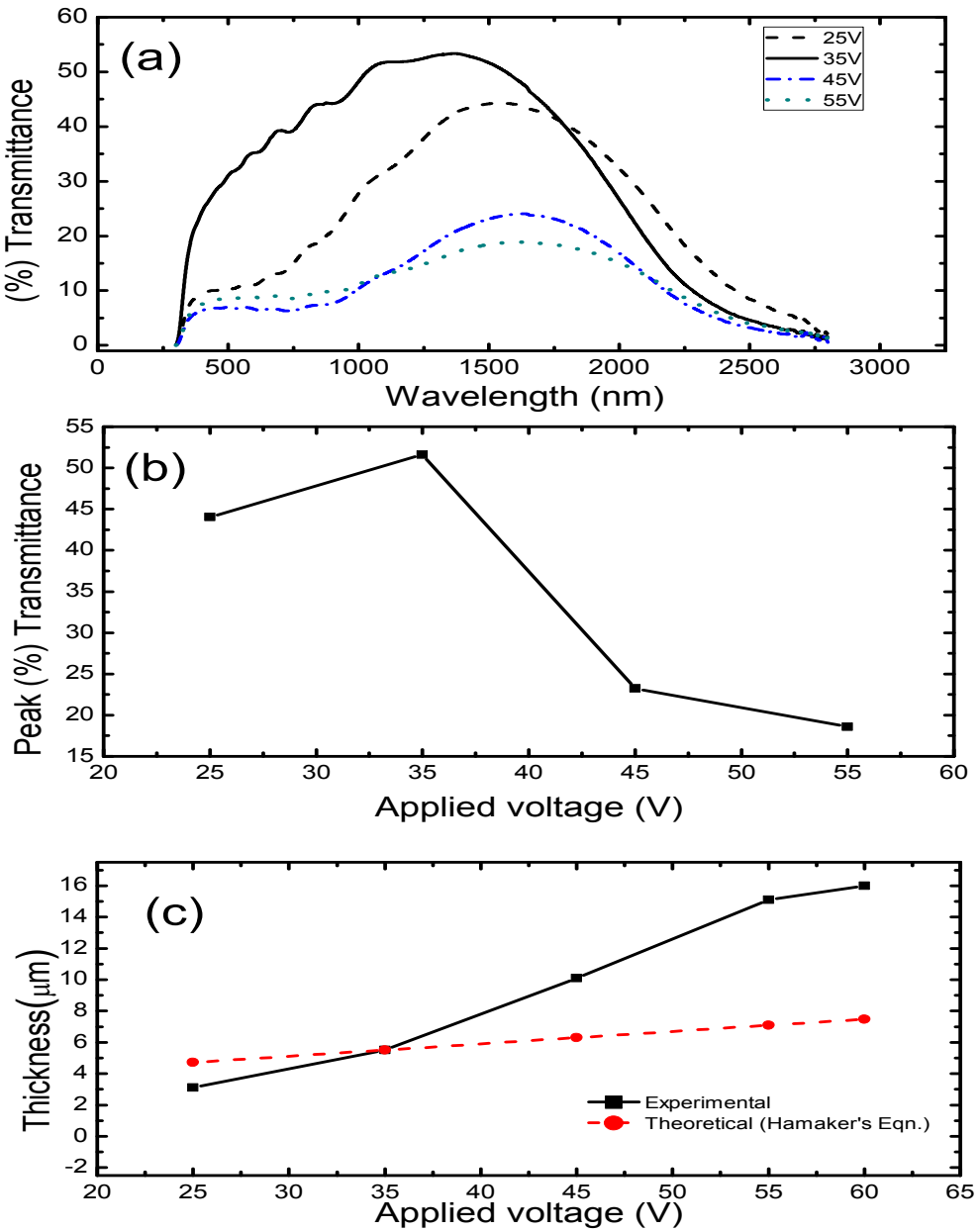

Figure 5.4: (a) Variation of transmittance with wavelength, (b) variation of peak transmittance with applied voltage, and (c) thickness versus applied voltage for TiO_2/Nb_2O_5 composite films deposited by EPD method using particle concentration of 0.25g/L and deposition time of 90s.

Transmittance was measured for composite films electrophoretically deposited at varied DC voltage in the range 25 V to 60 V. It can also be seen in Figure 5.4 that peaks of maximum transmittance decreased for films fabricated using increased values of EPD applied voltage. In addition, the peaks of maximum transmittance shifted towards the long wavelengths region as the applied voltage for films fabrication was increased. This shifting was attributed to the reduced energy (and large wavelength) of transmitted photons since part of their energy was absorbed by the film. The films deposited using higher EPD voltages had low transmittance which could have resulted from increased absorption of light that travelled through the thicker films. Thus the energy of transmitted photons reduced in thicker films which accounts for the shift in maximum transmittance peaks towards longer wavelengths.

The variation of peak transmittance with applied voltage is shown in Figure 5.4b while Figure 5.4c shows the variation of film thickness with applied voltage. From Figure 5.4c, it is noted that the thickness of films increased with increasing applied voltage. Thus, the decrease of transmittance with applied voltage was due to increase in thickness of the films and hence increased absorption of light as it travelled through the thicker films. These results were consistent with observation by Boccacini, (2010), that high voltages produce agglomeration of particles resulting in thicker films. Figure 5.4c also shows variation of theoretically determined film thicknesses with applied voltage.

The Hamaker's Equation was used to fit the thicknesses. The apparently large divergence between the experimental and theoretical results at large (≥ 35V) was attributed to greater throwing power of high applied voltages thus higher thicknesses. Consequently, the applied voltage of 35V corresponding to highest transmittance (53%), (Figure 5.4b) was chosen as the optimum applied DC voltage for deposition of TiO_2/Nb_2O_5 composite thin films. Table 5.1 shows the summary of the optimum EPD process parameters, namely DC applied voltage, deposition times and particle concentrations. Even for electrophoretic deposition of TiO_2 only, many different EPD process parameters have been used by other authors (Yum *et al*., 2005; Kim *et al*., 2007; Bandy *et al.,* 2011) as was shown previously in Table 2.1. It is clear that there are no unique process parameters for film deposition by EPD technique. That is why it is important to obtain the best deposition parameters in every situation. Composite films deposited using these optimized EPD process parameters were used in fabrication of the dye-sensitized solar cells in this study.

Table 5.1: Optimized electrophoretic deposition (EPD) process parameters for TiO_2/Nb_2O_5 composite electrode films deposition.

Concentration of TiO_2/Nb_2O_5 particles in 2-propanol suspension	Applied voltage across electrodes	Distance between electrodes	Deposition time
0.25 g/L	35 V	12 mm	90 sec

5.4 Morphological Characterization of TiO_2/Nb_2O_5 Composite Electrode Thin Films Using Scanning Electron Microscope (SEM)

Figure 5.5 shows the scanning electron microscope (SEM) images of electrophoretically deposited TiO_2/Nb_2O_5 composite thin films of varied film thickness. The SEM images show that a three dimensional network of interconnected TiO_2 and Nb_2O_5 nanoparticles formed when EPD method was applied in film deposition. The films compared in Figure 5.5 were: film, A, (i-iii) deposited using EPD parameters of 0.25g/L, 35V and 90s, film B (i-iii) deposited using EPD parameters of 0.25g/L, 35V and 270s. The SEM images of TiO_2/Nb_2O_5 composite thin films show that films at 270s formed some cracks (Figure 5.5 Biii) unlike those deposited for 90s (Figure 5.5 Aiii). Extended deposition times provided for more particles to move and form thicker films. These results concur with other studies (Basu *et al*., 2001) that indicate film quality deteriorates for extended deposition times. The SEM images show that mixed particles-composite structures described in chapter three (Figure 3.4b) were formed.

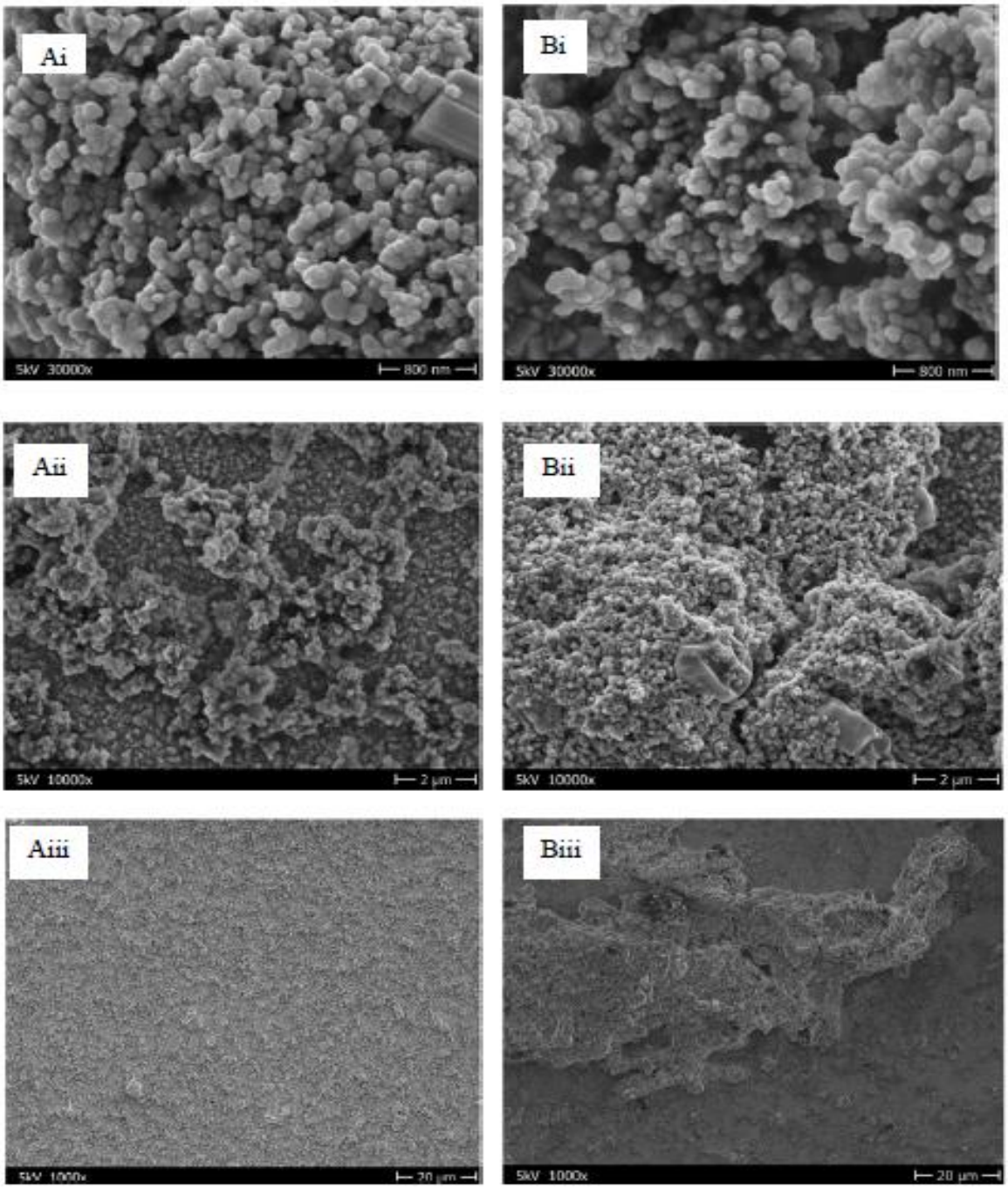

Figure 5.5: SEM images of TiO_2/Nb_2O_5 composite films electrophoretically deposited on FTO glass slide from suspension in 2-propanol at 35V from 0.25g/L. film A: deposition time of 90s, film B: deposition time of 300s. The films were annealed at 450°C for 6h.

5.5 Structural Characterization of TiO_2/Nb_2O_5 Composite Electrode Thin Films Using X-Ray Diffraction Analyzer

The crystal structure of TiO_2/Nb_2O_5 composite thin films was investigated by X-Ray Diffractometer using CuKα ($\lambda = 15.41\ nm$) radiation. Figure 5.6a shows the X-RD patterns for TiO_2/Nb_2O_5 composite film electrophoretically deposited at applied voltage of 35 DCV, for 90 s from particle concentration of 0.25 g/L. The diffractograms were recorded in the 2-Theta range of 10 - 80° and analyzed using the International Center for Diffraction Data (JCPDS card) (Feist and Davies, 1992; Frevel, 1955 (in Liu, *et al*., 2015)). In addition, X-RD graphs of TiO_2 films (Figure 5.6b) and Nb_2O_5 films (Figure 5.6c) are shown for comparison. The Diffraction peaks corresponding to films exhibit crystalline phases of both TiO_2 (2θ = 25.5, 33.8, 37.9 & 51.5) degrees and Nb_2O_5 (2θ= 26.5, 34.5, & 52.6) degrees. The dominant peak of TiO_2 was at 2-theta of 25.5 deg while that of Nb_2O_5 was at 26.5 deg. The diffraction peaks confirmed the presence of both titanium dioxide and niobium (v) oxide particles in the TiO_2/Nb_2O_5 composite film. Applying Scherer's equation (4.1), the average crystallite sizes at these peak positions were 15.36 nm and 15.49 nm and hence the crystallite dimensions were confirmed to the nanoscale.

However, the peak (= 1,600 a.u.) of TiO_2 was longer than that of Nb_2O_5 (= 900 a.u) which translates to ratio 1.78:1. The length of peaks corresponds to degree of crystallinity (Chang *et al*., 2009). It follows, therefore, that the crystallinity of TiO_2 was higher than that of Nb_2O_5. The intensity peaks were identified from standard JCPD diffraction data for TiO_2 and Nb_2O_5 shown in appendix II.

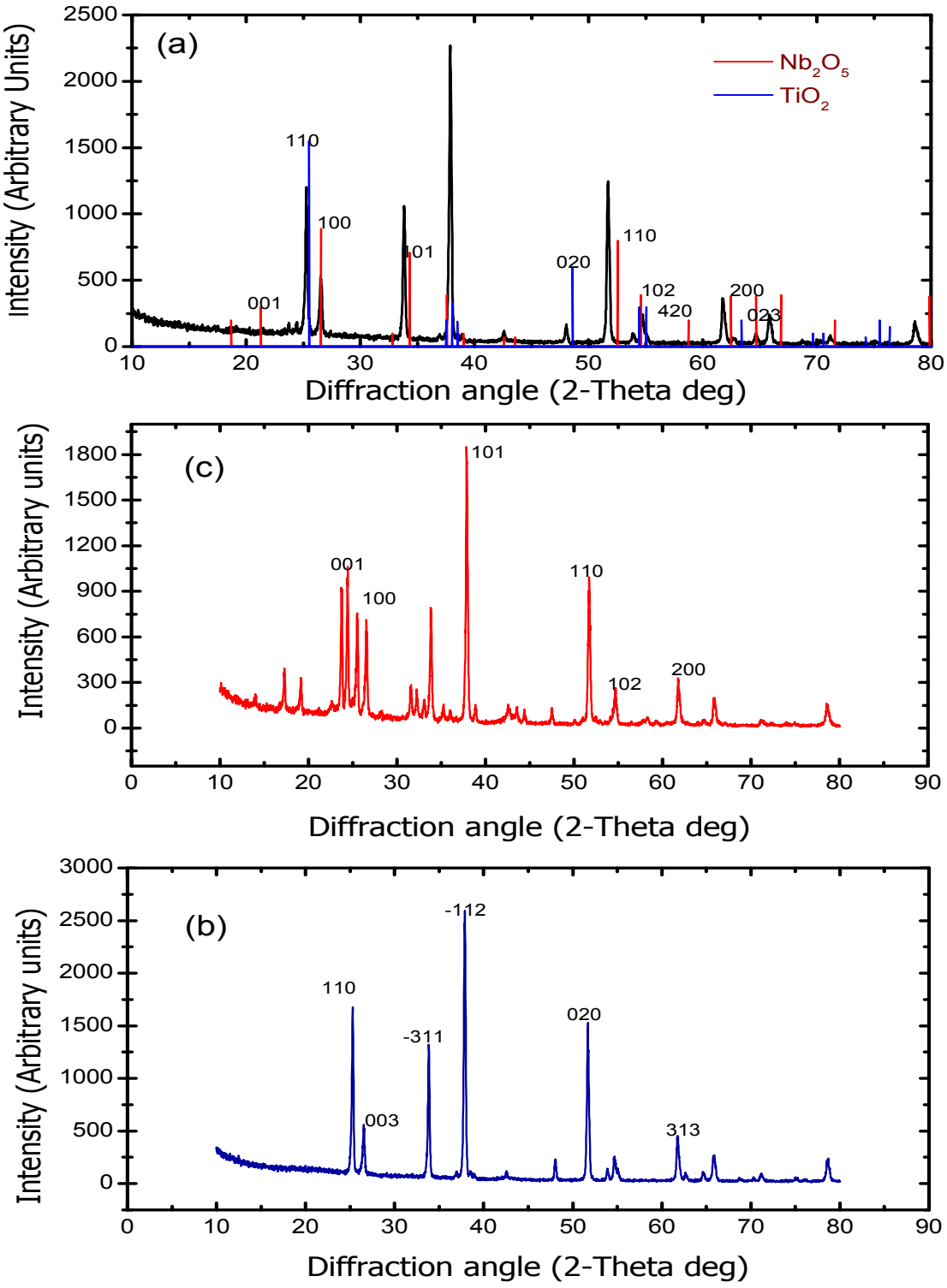

Figure 5.6: XRD spectra of thin films deposited with EPD parameters of 35 V, 90 s & 0.25 g/L (a) TiO_2/Nb_2O_5 composite (b) TiO_2 (c) Nb_2O_5. All films annealed at 450°C for 6h under atmospheric conditions.

5.6 Evaluation of Optical Band Gap Energy (E_g) of TiO_2/Nb_2O_5 Composite Films

Figure 5.7 shows plot of $(\alpha h\upsilon)^2$ versus photon energy ($h\upsilon$) for evaluating band gap of TiO_2/Nb_2O_5 composite thin films, and pure TiO_2 and pure Nb_2O_5 thin films. The linear variation of $(\alpha h\upsilon)^2$ versus $h\upsilon$ at the absorption edge indicates direct transitions took place across the band gap of the material (Gould & Lamont, 2010). The optical band gap energy (E_g) was estimated by drawing a tangent to the linear part of the curve and extrapolating the tangent to intercept the $h\upsilon$ - axis.

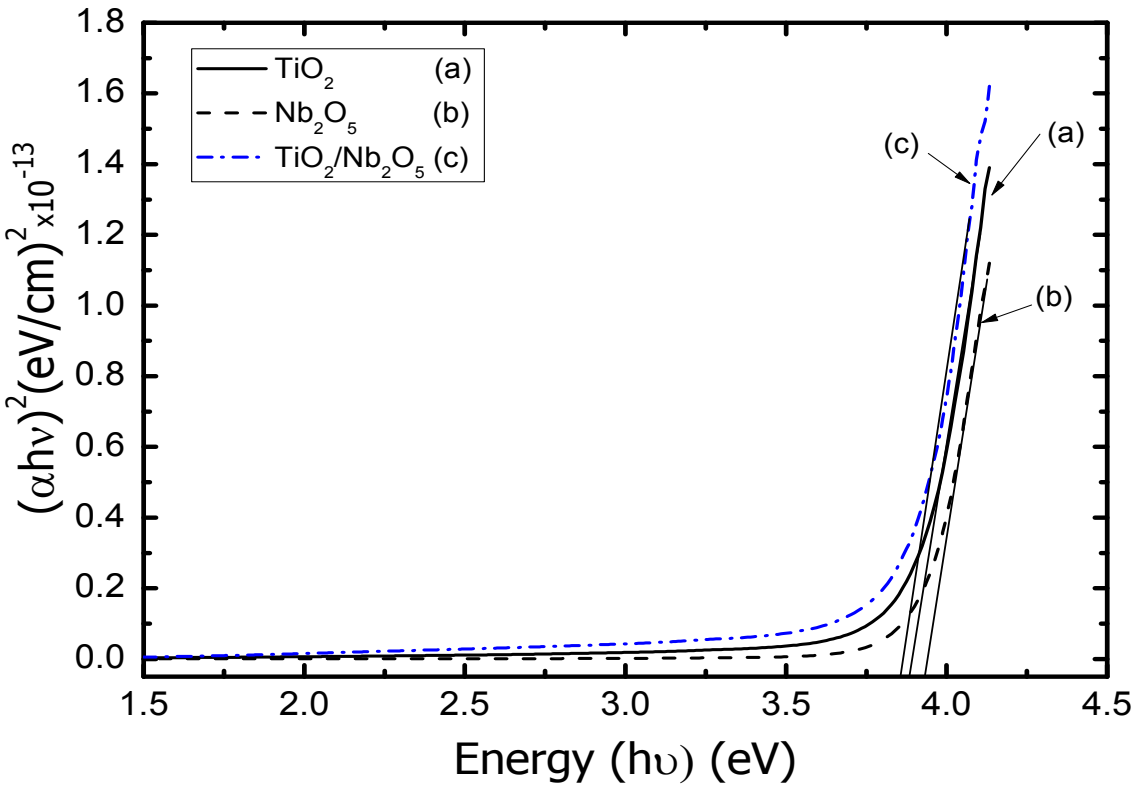

Figure 5.7: Variation of $(\alpha h\upsilon)^2$ versus photon energy ($h\upsilon$) for direct band gap transitions in TiO_2 (a), Nb_2O_5 (b) and TiO_2/Nb_2O_5 (c) composite films at particle concentration of 0.25g/L all the films were deposited using EPD technique at 35V, 0.25g/L, and 90s.

All films were deposited using the same EPD process parameters; i.e., applied voltage (35 V), particle concentration (0.25 g/L) and deposition time (90 s). Band gap energies E_g =3.932 eV for pure Nb_2O_5, E_g = 3.884eV for pure TiO_2 and E_g = 3.858 eV for TiO_2/Nb_2O_5 composite

films were obtained. It follows that band gap energy obtained experimentally for the composite film was lower than those obtained for pure TiO_2 and pure Nb_2O_5. This decrease in energy band gap for composite film was explained in terms of development of sub-band gap states in the TiO_2/Nb_2O_5 composite films. These sub-band gap states lie deep in the tail of the density of states in the films and lead to decreasing the optical energy gap and shifting the absorption edge towards the higher wavelength of the incident photons. The theoretical direct band gap value of TiO_2 is E_g = 3.25 eV (Nowotny *et al*., 2008) and for Nb_2O_5 is E_g = 3.49 eV (Jose *et al*., 2009). Thus, values of energy band gaps obtained experimentally for both TiO_2 and Nb_2O_5 were greater than the corresponding theoretical values. It is noteworthy that the band gap from Tauc equations and corresponding plots were estimates and that the slope of the absorption edge could have been affected by defects in the crystals.

Table 5.2, shows a comparison of band gap energies for TiO_2 determined in this study with those reported in literature. It is observed that the measured E_g values lie in the range 3.25eV to 4.14 eV of the reported E_g values.

Table 5.2: Values of direct and indirect optical band gaps of TiO_2 and Nb_2O_5 reported by various authors.

Type of Thin film	E_g (eV) (direct)	E_g (eV) (indirect)	Reference
TiO_2	3.25	NA	Jose *et al*., (2009)
	3.88	NA	Narayan & Raturi (2012)
	4.14	3.4	Ghrairi & Bouaicha (2012)
	3.88	NA	Yavuz, (2014)
	3.5-3.9	2.1-3.0	Oommen *et al*., 2012
	3.93	**NA**	***in this Study***
Nb_2O_5	3.49	NA	Sancho-Paramon, *et al*., (2008)
	3.9	NA	Parakh & Garg (1985)
	3.75	NA	Kovendlan *et al*., (2011)
	NA	3.4	Yan *et al*., (2012)
	3.86	**NA**	***In this Study***
TiO_2/Nb_2O_5	**3.88**	**NA**	***In this Study***

NA ≡Not available

These results support the position that the band structure of nano-materials is greatly deviated from their bulk counterpart (Jose *et al*., 2009).The condition that must be met for good performance of a dye-sensitized solar cell is that the conduction band (CB) edge in semiconductor has to match the lowest unoccupied molecular orbital (LUMO) of the excited dye molecule to enable effective electron injection from the molecule's excited state to the semiconductor's CB (Maluta, 2010). If the conduction band is lower in energy than the excited state of the dye molecules, electron injection from the dye into the CB is good. On the other hand, if CB is higher in energy, the electron injection is suppressed. The suppression of electron injection contributes to low currents in the cells resulting in low conversion efficiencies.

5.7 Effect of Annealing Time on Optical Band Gap of Composite Films

Figure 5.8 shows the plot of $(\alpha h\upsilon)^2$ against the photon energy $h\upsilon$ for TiO_2/Nb_2O_5 composite films. The effect of annealing (dwelling) time on optical band gap was studied by annealing the TiO_2/Nb_2O_5 composite thin films at 450°C for different dwelling times between 1 and 6 hours. All the films were deposited using electrophoretic technique for deposition time of 90 s, applied voltage of 35V, and from particle concentration of 0.25g/L.

Values of the measured band gap energies were recorded in Table 5.3. The optical band gap of the as-deposited (un-annealed) film was found to be 4.063eV (Figure 5.8) which was a value higher than any value of the annealed films. The decrease in band gap upon annealing of films could be attributed to improved crystalline structure of the TiO_2/Nb_2O_5 composite films with increase in annealing temperature (from room temperature to 450°C).

The lowest states in conduction bands are localized (traps) due to the disordered arrangement of the films deposited at low temperature (Matthew *et al*., 2012). These localized states make the absorption edge shift to a higher energy. The crystallinity of the films was discussed previously using XRD graphs (Figure 5.6) which show the intensity peaks with their width for specific crystalline regions within a material. After annealing at 450°C for between 1 and 6 hours, the band gap decreased from 3.891eV for films annealed for 1 hour to 3.797 eV for similar films annealed at same temperature for 6 hours.

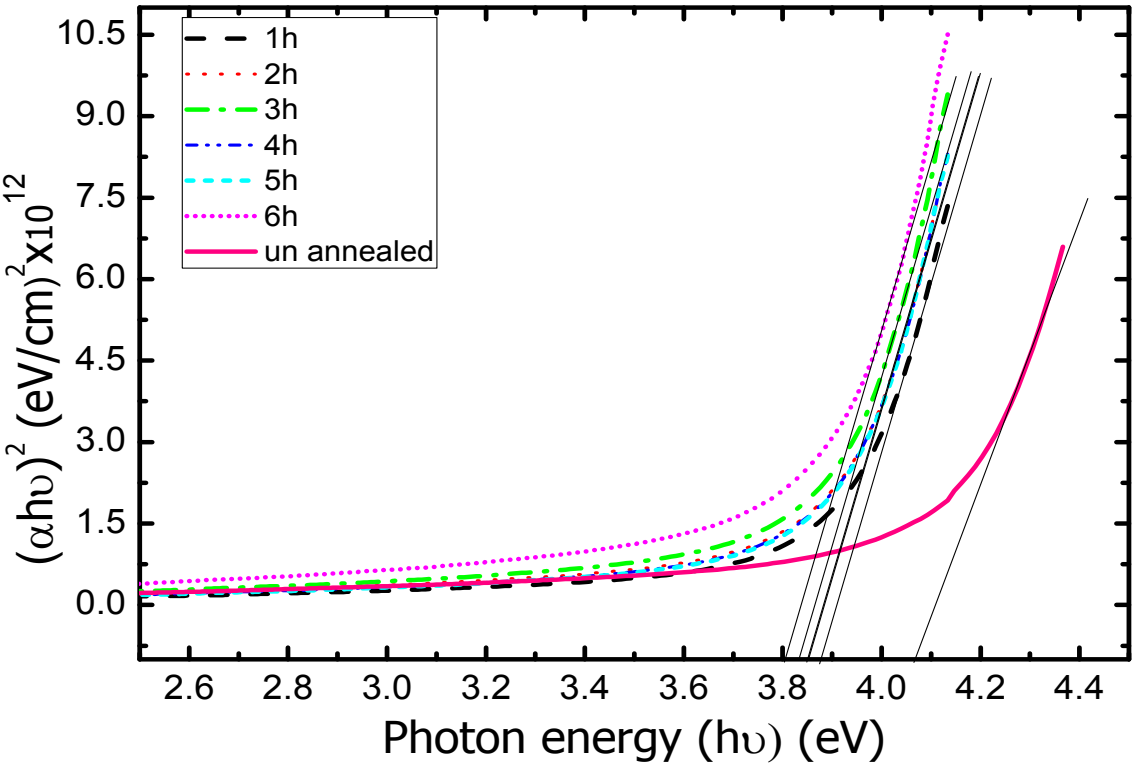

Figure 5.8: Variation of $(\alpha h\upsilon)^2$ with photon energy $(h\upsilon)$ for direct transitions in TiO_2/Nb_2O_5 composite films deposited using electrophoretic technique using 35V, 0.25g/L, for 90s and annealed for 1 to 6 hours.

Table 5.3: Band gap energies for TiO_2/Nb_2O_5 composite films annealed at 450°C for different annealing times between 1 and 6 hours.

Annealing (dwelling) time (hrs)	Band gap energy (eV)
1	3.8911
2	3.8520
3	3.8515
4	3.8319
5	3.8315
6	3.7965
As-deposited	4.0633

The variation of band gap energies with annealing (dwelling) time is shown in Figure 5.9. It was observed that the band gap energy values decreased linearly with increased annealing

time intervals. Decrease in band gap for increased annealing time has also been reported in literature (Sanjeev & Kekuda, 2015). The narrowing of band gap could have resulted from decrease in transitions due to reduction of the oxygen defect width as a result of air annealing which fills up the vacant oxygen levels.

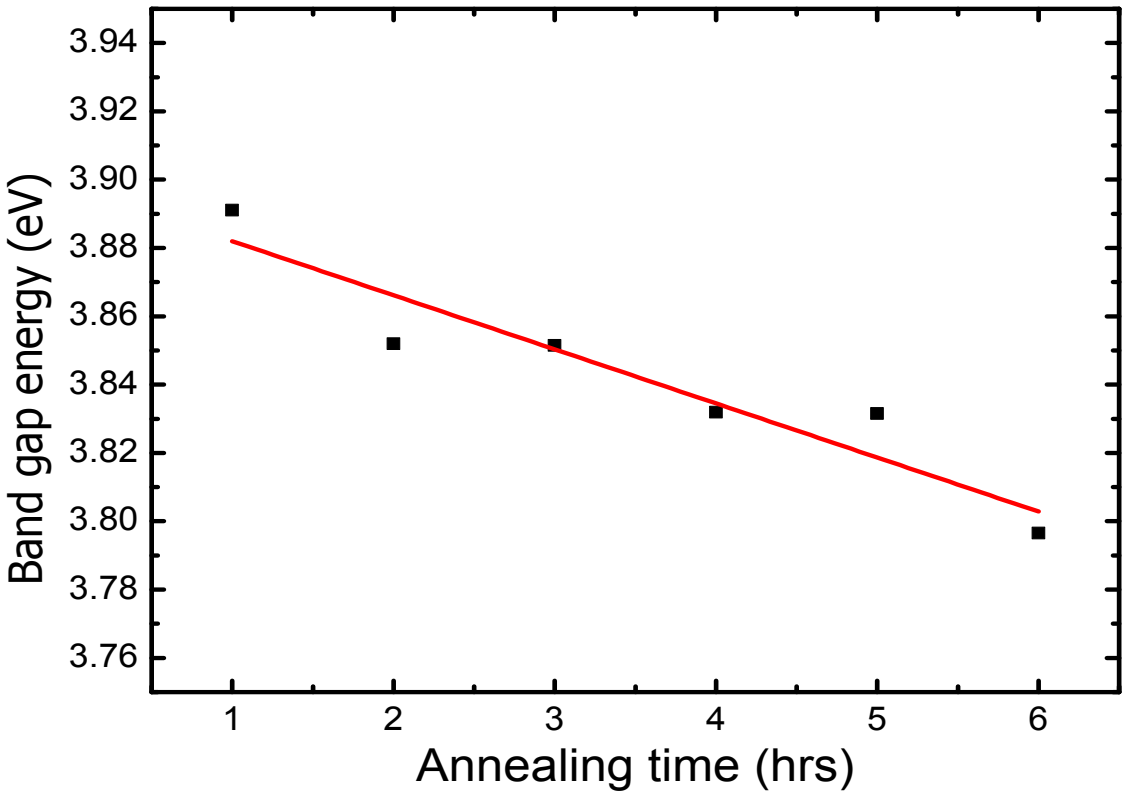

Figure 5.9: Band gap energy versus annealing time for TiO_2/Nb_2O_5 composite thin films annealed at 450°C for different annealing (dwelling) times between 1 and 6 hours. The films were deposited using the EPD technique from 0.25g/L, 35V, and 90s.

5.8 Evaluation of Urbach Energy

The values of Urbach energy were calculated from the plot of $\ln(\alpha)$ versus photon energy ($h\upsilon$) for the TiO_2/Nb_2O_5 composite films (Figure 5.10). The plot is governed by equation (3.23);

$$ln(\alpha) = ln(\alpha_0) + h\upsilon / E_U \qquad (5.2).$$

The reciprocal gradient of the linear portion of the curve was used to calculate the Urbach energy and a value of 434meV was obtained. The values of E_U can be used to measure

structural disorder in the prepared samples. The Urbach energy value of 434meV indicated that there was considerable introduction of tail states at the band edges thus influencing the electron transport in the film. Increase in annealing time is known to restrict the shuffling motion of atoms in composite films. Such limited motion could have contracted the Urbach tailing thus lowering the E_U, due to reduced number of vibrational energy levels for a given electronic state.

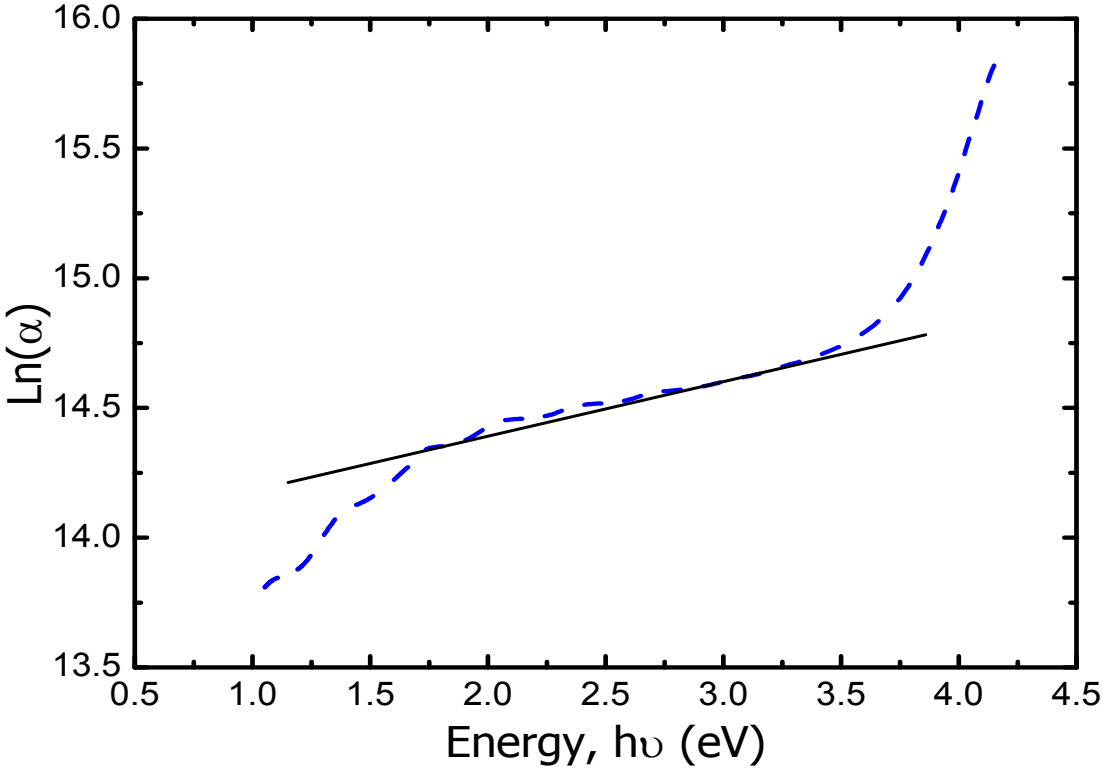

Figure 5.10: Variation of $\ln(\alpha)$ with photon energy for TiO_2 / Nb_2O_5 composite thin films prepared using electrophoretic deposition technique. using 0.25g/L, 90s and 35V and annealed at 450°C for 6h

The value of Urbach energy obtained in the study compares closely with 455eV for ZnO thin films obtained by Yakuphanoglu *et al*., (2007). The obtained value of E_U was within the range (460 to 660 meV) for semiconductors reported by Sta *et al*., (2014). The Urbach energy value of 434meV obtained in this study was significant in indicating the introduction of tail states at band edges that influence electron transport.

5.9 Extinction Coefficient

Figure 5.11 shows the plot of absorption coefficient α $\alpha(\lambda)$ against inverse of wavelength (1/λ) for TiO_2/Nb_2O_5 composite thin films in the wavelength range $400 \leq \lambda \leq 700$nm (visible

light region). The slope of Figure 5.11 was used to calculate the value of extinction coefficient (k), and an average value of k = 0.0354 at $400 \leq \lambda \leq 700$nm for fabricated TiO_2/Nb_2O_5 composite thin films was obtained.

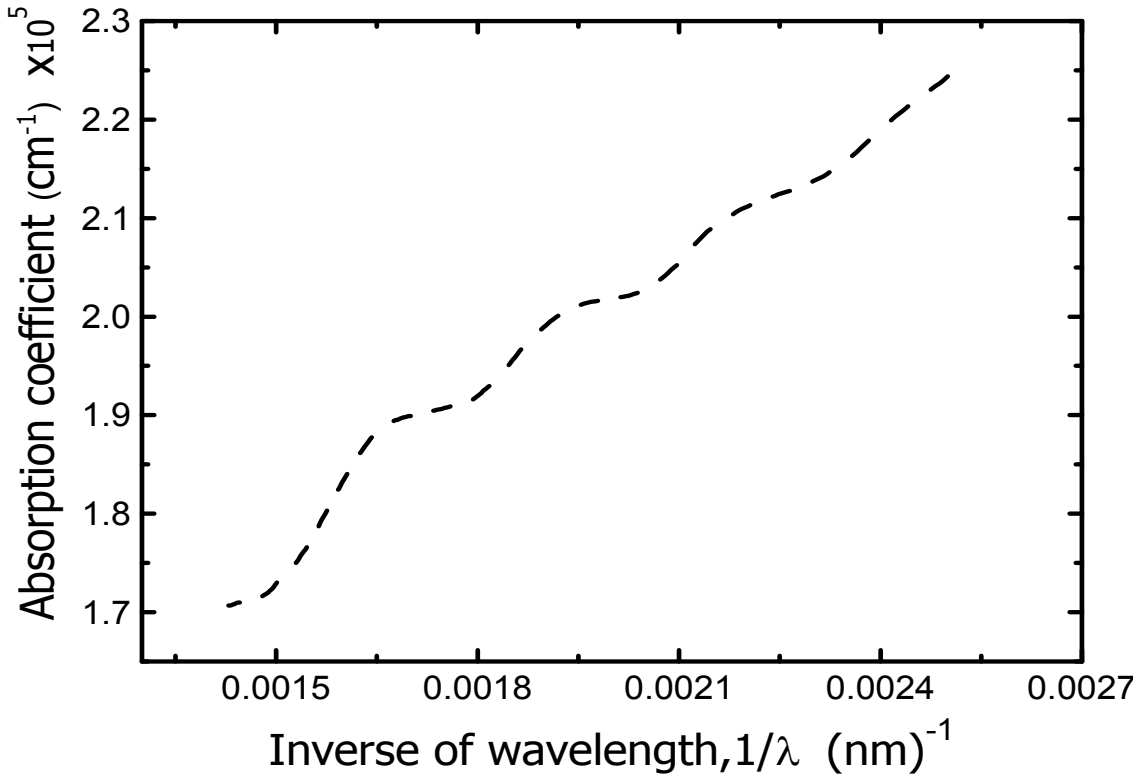

Figure 5.11: Variation of absorption coefficient (α) versus inverse of wavelength for TiO_2/Nb_2O_5 composite films deposited using EPD technique at 35v, 0.25g/L, and for 90s and annealed at 450°C for 6h.

The extinction coefficient (k), is an optical property of the semiconductor material and determines how much light is absorbed by the material. Light is absorbed when $k > 0$, while light travels straight through the material when $k = 0$. In this study, a value of 0.0354 was obtained for extinction coefficient (k) which was attributed to low absorption of light by the TiO_2/Nb_2O_5 composite electrode thin films due to their large energy band gap. The results are consistent with the knowledge about high band gap semiconductors that cannot require sensitization with a dye to function as photoelectrodes in a dye sensitized solar cells

5.10 Evaluation of Refractive Index (n)

Refractive index is associated with refraction of light passing through a material. The absorbance of TiO_2/Nb_2O_5 composite thin films was plotted against wavelength in the range 200 to 2800 nm (Figure 5.12). Absorbance is the capacity of a material (film) to absorb light of a specified wavelength.

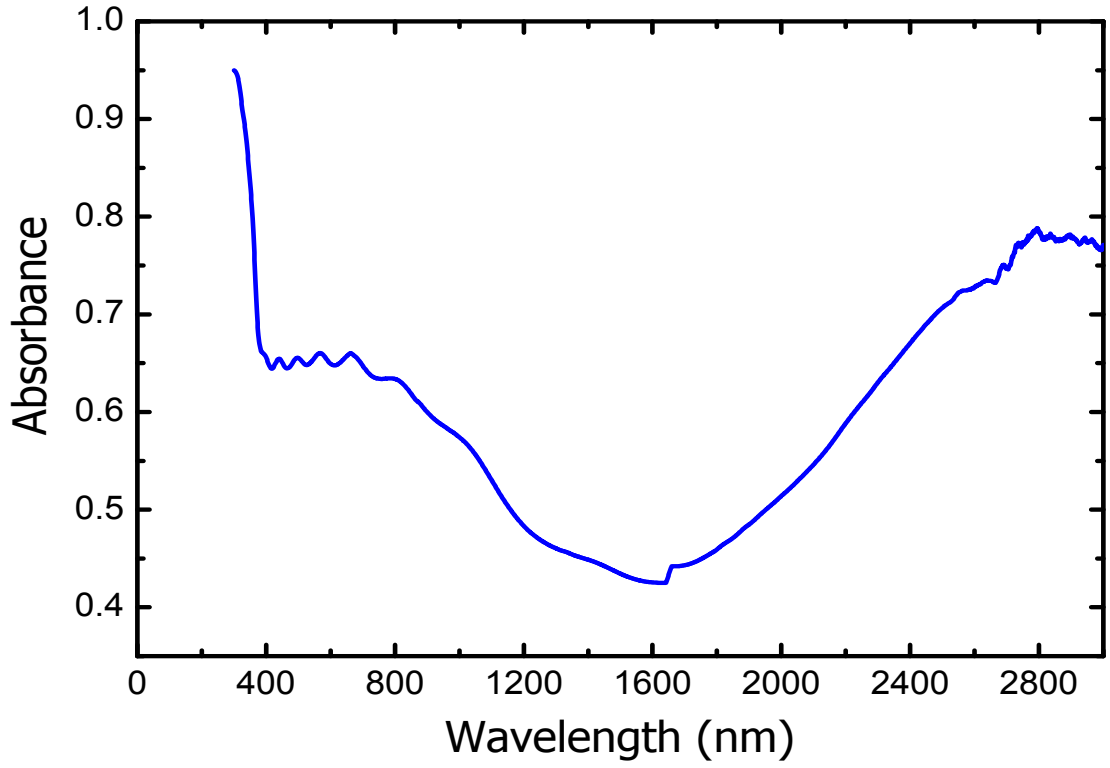

Figure 5.12: Absorbance spectrum: values calculated from transmittance and reflectance data for TiO_2/Nb_2O_5 composite thin filmsdeposited by EPD method at 35V, 0.25g/L, for 90s and annealed for 450°C for 6h.

As shown in Figure 5.12, the absorbance by the composite film is non-uniform as a function of wavelength; with some regions showing low and others showing high absorbance. Simlar phenomenon has also been reported by other authors (Born & Wolf, 2005). In the region corresponding to wavelength range $400 \leq \lambda \leq 800$nm in the absorption spectrum, the absorbance was fairly constant (0.65) and therefore equation (5.3):

$$n = (1 + R + 2\sqrt{R}) / (1 - R) \tag{5.3}$$

was applied to evaluate refractive index (n) over the corresponding spectrum region.

The refractive index of $n = 1.643$ was obtained for wavelengths between 400 nm and 800 nm (Figure 5.12). Different values of refractive indices have been reported by authors like Hosaka *et al.*, (1997), who obtained refractive index equal to 2.55 for TiO_2 at $\lambda = 600\,nm$. Mandic (2015) also reported refractive index $n = 2.493$ for TiO_2 at $\lambda = 632.8\,nm$. At $\lambda = 550\ nm$ the refractive index of TiO_2 films annealed at 600°C was 2.11 (Matthews *et al.*, 2009). The refractive index (n) was found to be 1.65 at λ =800 nm (Govindasamy, *et al.*, 2016). Lemarchand, (2012), reported refractive index $n = 2.321$ of Nb_2O_5 at $\lambda = 632\,nm$. This large divergence between results of n obtained in this study and those reported in literature was attributed to changes in film density caused by different deposition processes. From the rule of mixtures;

$$n_c = f\, n_{TiO_2} + (1 - f) n_{Nb_2O_5} \tag{5.4}$$

the average value of $n_{TiO_2} = 2.535$ and $n_{Nb_2O_5} = 2.359$, in the wavelength range $400 \le \lambda \le 800\,nm$, and $f = 0.5$ were substituted in to Equation 3.27 to predict n_c. The refractive index of TiO_2/Nb_2O_5 composite film was found to be 2.476. This predicted value for the composite film was higher than value obtained in this study. A plausible reason for the difference in refractive index values was that experimental conditions to satisfy assumptions made in derivation of Equation (3.23) may not have been fully met. Derivation of Equation (3.23) was based on assumptions that the absorption of light was high and interference was nil. It was observed, however, that plots of transmittance (Figures 5.2a; 5.3a; 5.4a) indicated the presence of some interference.

5.11 The Polarity of Charge Carriers

The variation of current (I) as a function of Hall voltage (V_H) for TiO_2/Nb_2O_5 composite thin films has been studied and the results shown in Figure 5.13. it can be seen in the figure that the current increased with Hall voltage despite the voltage biasing. The sign of the Hall voltage (V_H) and Hall coefficient (R_H) indicate a net positive carrier concentration for $F:SnO_2$ coated glass, and TiO_2 (Figure 5.13). The majority charge carriers are positive charges or holes. Bulk TiO_2 is an n-type semiconductor. However, as pointed out by Jose *et al.*, (2009), the band structure of nanomaterials is deviated from that of the bulk material. The net

positive carrier concentration could be attributed to donor-type defects including oxygen vacancies and titanium (cation) interstitials. The p-type properties could have been caused by the presence of titanium vacancies in TiO_2 as was also observed by Nowotny *et al*., (2008).

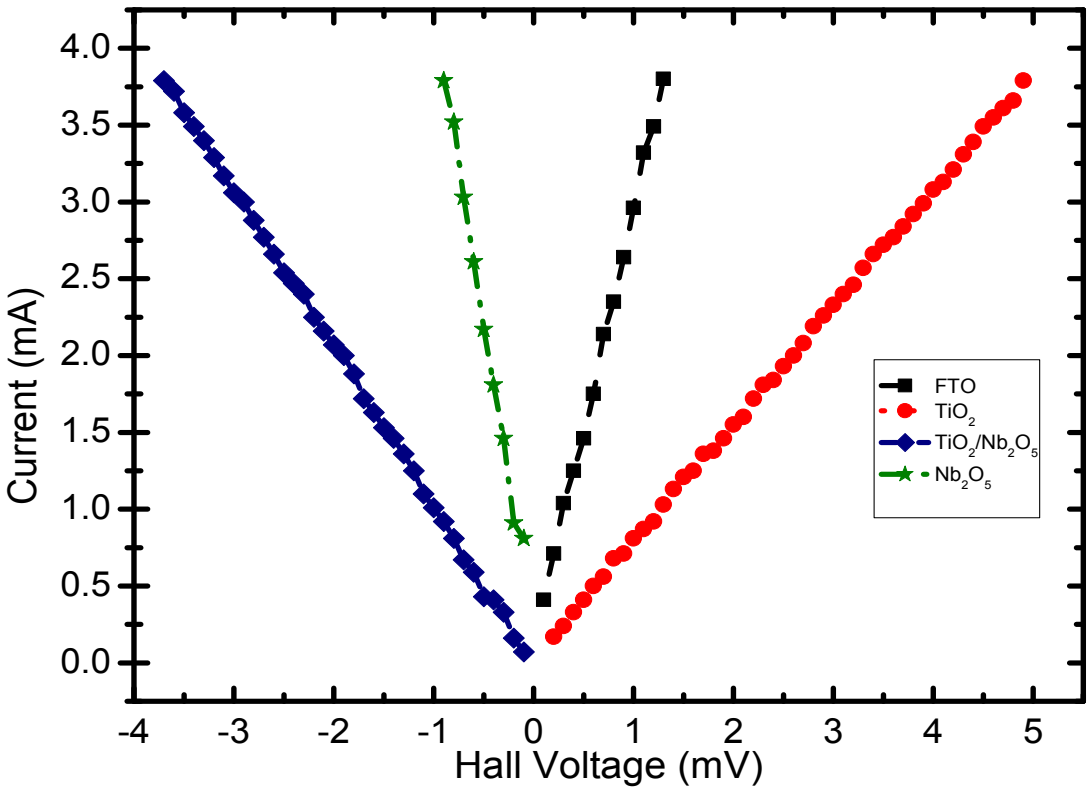

Figure 5.13: Current versus Hall voltage for pure TiO_2, Nb_2O_5 and Nb_2O_5/TiO_2 composite films deposited using EPD technique at 35V, 0.25g/L, for 90s and annealed for 450°C for 6h.

Films whose Hall voltage showed a positive sign were p-type while those whose Hall voltage showed negative sign were n-type. Fluorine doped tin oxide (FTO) film was found to be

n-type. It is reported (Hartnagel *et al*., 1995) that tin oxide becomes doped n-type by adding Fluorine which incorporates on oxygen sites. Films of niobium pentoxide (Nb_2O_5) only, and films of TiO_2/Nb_2O_5 composite films yielded a net negative carrier sign indicated by both the Hall voltages and Hall coefficients. In these films, the electrons form the majority charge carriers. Nb_2O_5 is reported to become an n-type semiconductor at lower oxygen content (Diebold, 2003). The net electron concentration could also be due to donor impurities with hydrogen being a likely candidate. Unintentional impurities such as hydrogen are likely sources of observed unintentional conductivities in metal oxide semiconductors. Hydrogen is

a widely available impurity which diffuses as an interstitial impurity and is capable of assuming substitutional positions as Wu *et al*., (2012) also observed. The n-type behaviour of TiO_2/Nb_2O_5 composites films could be due to incorporation of Nb^{+5}, and O^{-2} donor ions. The bulk sized TiO_2 is an n -type semiconductor that contains donor type defects such as oxygen vacancies and interstitial titanium.

5.12 Charge Carrier Density and Carrier Mobility

Table 5.4 shows the values of Hall coefficient, charge carrier density and carrier mobility obtained in this study and compared with those reported by other authors. The values of Hall coefficient compared closely with those reported in literature. On the other hand, charge carrier density values for TiO_2/Nb_2O_5 composite thin films were an order of magnitude lower higher than those reported by authors like Tang *et al*., (1994). The Hall coefficient and carrier density are inversely related according to equation (3.35);

$$n_d = \left(qR_H\right)^{-1} \tag{5.5}$$

The low values of carrier concentration could be attributed to electrons trapping in surface states of the high surface area composite film while reduction of carrier mobility could have resulted from increased grain boundaries between the TiO_2 and Nb_2O_5 particles in a composite film. The reciprocal gradient of the linear portion of the curve was used to calculate the Urbach energy and a value of 434meV obtained for E_U confirmed considerable introduction of tail states at the band edges that influence the electron transport.

Different magnitudes of carrier mobility reported could be attributed to different measurement techniques like time-of-flight photocurrent measurements and space charge limited current measurements. Charge carrier mobility is an important factor affecting the current density in a solar cell. An undisputed observation is that charge (electron) mobility in mesoporous TiO_2 is many orders of magnitude lower than that in nanoparticles (Tang *et al*., 1994).

From the rule of mixtures, 2.152 $cm^2V^{-1}s^{-1}$ was obtained as carrier mobility of TiO_2/Nb_2O_5 composite film, a value lying between 1.812 for TiO_2 and 2.492 for Nb_2O_5.

Table 5.4: Hall Effect parameters from the study compared to those reported by several authors.

Type of thin film	Hall coefficient (cm^3/C)	Charge carrier density (cm^{-3})	Carrier mobility ($cm^2V^{-1}s^{-1}$)	Reference
In this study				
TiO_2	0.758	7.89×10^{18}	1.812	*in this study*
TiO_2/Nb_2O_5	0.975	6.14×10^{18}	2.653	*in this study*
Nb_2O_5	3.725	1.61×10^{18}	2.492	*in this study*
Other authors				
TiO_2	4.33	1.44×10^{18}	0.0226	Hateef *et al*., (2012)
TiO_2 Anatase	0.5	5.00×10^{18}	0.1 - 4	Tan, (1994)
TiO_2 Rutile	-	1.00×10^{19}	0.2	Springer, (2004)
TiO_2 Anatase	-	1.00×10^{19}	4	Tang *et al*., (1994)
TiO_2 Rutile	-	2.50×10^{19}	0.1	Tang *et al*., (1994)
SnS:Ag	0.8	7.24×10^{14}	14.3	Jia *et al*., (2010)
GaAs (thick film)	2.7	2.30×10^{18}	0.0125	Fraser, (2011)

The low values of mobility resulted from charge recombination since holes and electrons have opposite average drift velocities. Increase in concentration of Nb_2O_5 led to decrease in charge density therefore the resistivity decreased. However, higher particle concentration could explain the increased particle-to-particle interfacial resistances which serve as centers for dispersion of mobile carriers and causes increase in resistivity of the composite films.

5.13 Characterization of a Complete Solar Cell by Measuring Photoelectric Current-Voltage (I-V) Parameters

Figure 5.14 shows the current density versus voltage (J-V) curves of DSSCs fabricated using TiO_2/Nb_2O_5 composite thin film photoelectrodes of varying thickness. The films were deposited by EPD technique by applying voltage of 35 V, and using particle concentration of 0.25g/L. The cell fabricated using 5.5 μm thick composite films produced the highest current density and the highest cell efficiency equal to 1.99% (~2%) under 100 mW/cm^2 at AM 1.5 illumination. Low efficiency of assembled cells was attributed to poor film adhesion to the glass substrate.

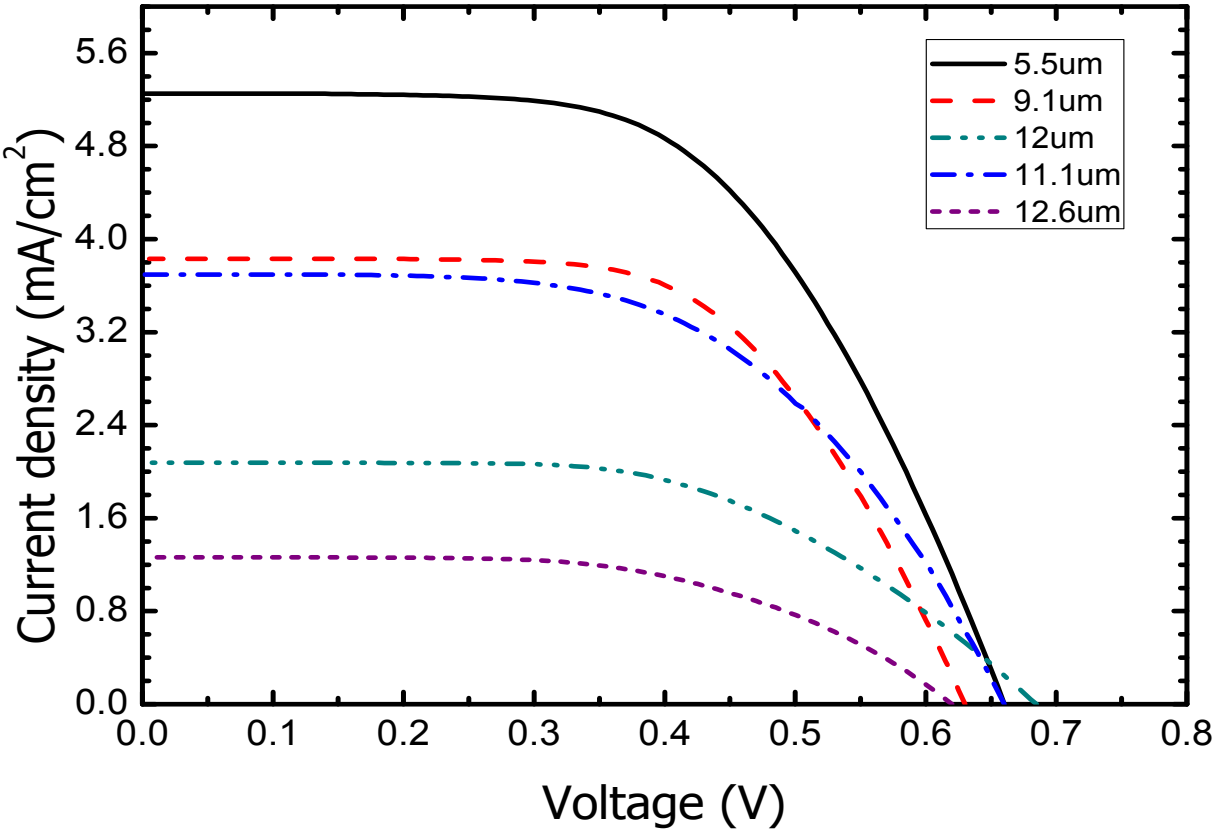

Figure 5.14: Current density-voltage curve of DSSCs fabricated using TiO_2/Nb_2O_5 composite photoelectrode thin films of varying thickness.deposited by EPD method at 35V, from 0.25g/L, for 90s resulting in films of different thicknesses. The films were annealed at 450°C for 6h.

Films thicker than 5.5 μm showed lower current densities and cell efficiencies which rapidly decreased with increasing thickness. This was attributed to a high recombination rate of the electrons injected into the film. The injected electrons in the TiO_2/Nb_2O_5 composite films possess a too small diffusion length so that they recombine with electrolyte before they reach the FTO. Also, low current density could have resulted from poor coverage of particles with dye or low electron injection by light. The cells were further analyzed using the electrochemical impedance spectroscopy (EIS).

5.14 Characterization of a Complete Solar Cell by Measuring Electrochemical Impedance Spectroscopy (EIS)

Figure 5.15 shows the Nyquist and Bode plots for EIS measurements on fabricated dye-sensitized solar cells of varying thickness. A series resistance and parallel RC combination

circuit (d) was used to analyze the measured impedance data through the use of NOVA software.

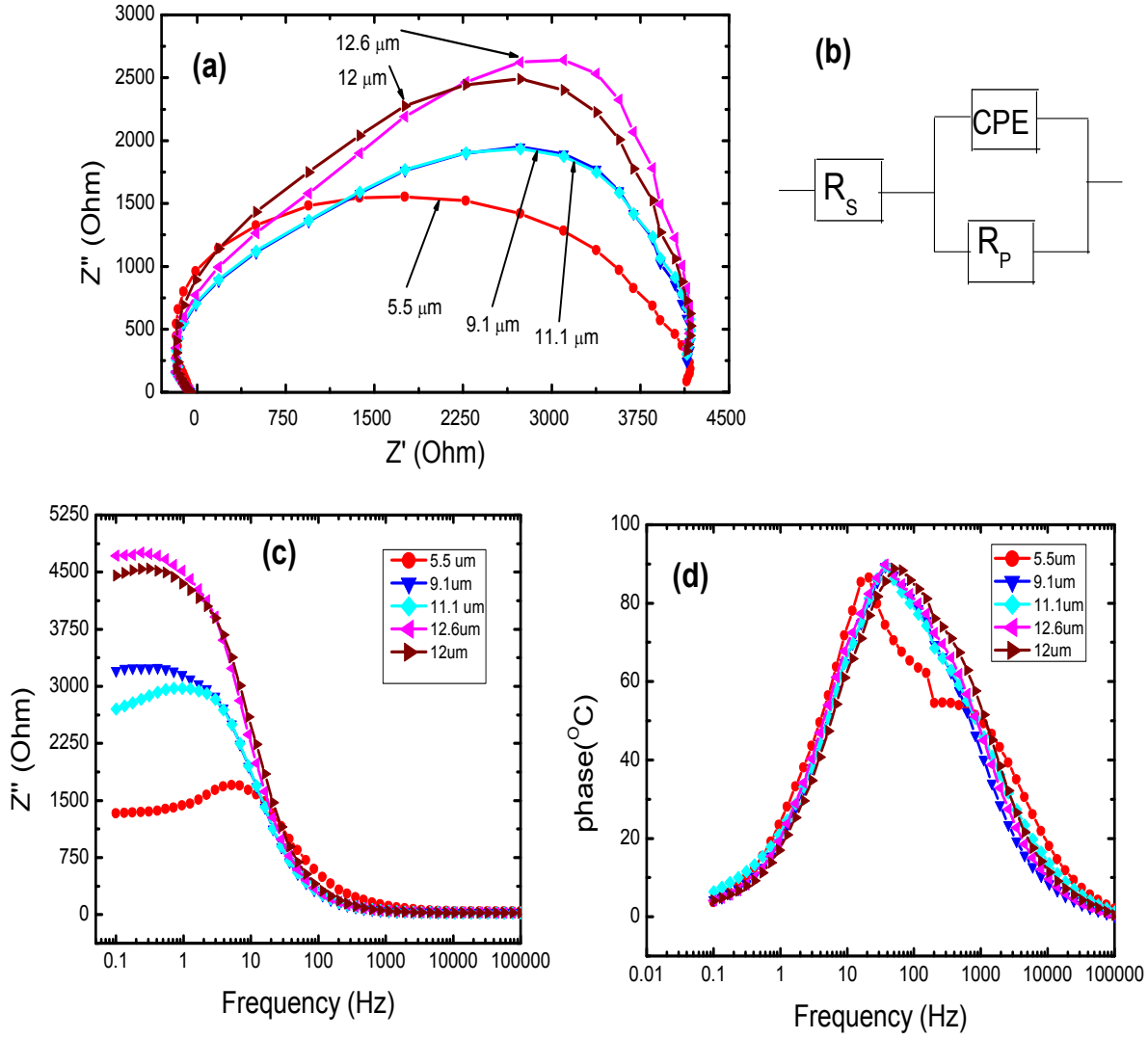

Figure 5.15: (a) Nyquist plot (b) the equivalent circuit showing elements R_S (series resistance), *CPE* (constant phase element) and R_P (the parallel resistance) . (c) Bode plot and (d) Bode phase of DSSCs assembled using TiO_2/Nb_2O_5 composite electrode films. The films were prepared by electrophoretic deposition at 35V, from 0.25g/L and different deposition times resulting in different film thickness. The cells were subjected to 0.5V forward biasing in frequency range of 10KHz to 0.1KHz.

Only one major semicircle was observed to be evident in the measured frequency range of 10 KHz - 0.1 KHz. This central semicircle is seen to lean to the positive side of the real impedance indicating that the charge transport resistances (R_t) in TiO_2/Nb_2O_5 composite

films were less than charge recombination (R_r) at the TiO_2/electrolyte interface. A capacitor can be substituted by an open circuit at low frequency because capacitive reactance is inversely related to frequency ($Z_C = 1/j\omega C$). At low frequency, the Nyquist plot (Figure 5.15a) corresponds to variation of the parallel resistance with thickness, which in turn implies a change in the characteristic time since ($t = R_P CPE$).

The absence of the arc in the low frequency region could mean the mass transport impedance (Z_d) due to diffusion of red-ox species in electrolyte was negligible in this case. This factor could be explained by use of high performing electrolytes in cell fabrication. Also not evident, were the arcs associated with high frequency region where impedance contributions originate from the double-layer capacitances and platinum coated-counter-electrode transfer resistances. This could be related to small currents flowing through the complete cell thus causing little diffusion effects. The impedance of the diffusion-recombination follows the Gerischer impedance if $R_t > R_r$ In a DSSC, it is desired that $R_t < R_r$ to avoid loss of injected electrons through recombination with the electrolyte.

The shape of the Nyquist plot with only one arc (the Gerischer impedance) is likely to be evident at high potential (0.5V) in which case, the equivalent circuit exhibits behaviour of the working electrode (Fabregat-Santiago *et al.*, 2007). In Gerischer impedances, Nyquist plot reduces to one main arc generated by parallel arrangement of charge-transfer resistance (R_r) of TiO_2 and the chemical capacitance (C_μ) of TiO_2 to electrolyte.

In our measurements, Gerischer impedance was attributed to the transport resistance in the composite film (R_t), charge-transfer resistances (R_r) at the film/dye/electrolyte interface represented by *Rp* and chemical capacitances in the composite films /electrolyte interfaces represented by constant phase element (*CPE)*. The genesis of high values of *Rp* was attributed to the relatively poor adhesion of the film on to FTO glass slides. The poor adhesion could be demonstrated by scratching the TiO_2/Nb_2O_5 composite films from the FTO-coated glass slides which resulted in film easily rubbing off. The poor adhesion introduced high contact resistance for the charge transfer from film to the FTO glass surface. Further Although the XRD micrographs showed peaks of relatively high crystallinity of the nanostructured TiO_2/Nb_2O_5 composite film, the composite films could still be treated as a

relatively disordered material with electronic traps affecting not only the surface events, but any kinetic measurements, including the chemical capacitance and recombination lifetime (Bisquert *et al*., 2000).

he EIS measurements performed on the cells revealed that the charge-transfer resistance of the TiO_2/electrolyte interface in the cell with thicker films were lower than those of cells of thinner films (Figure 5.15). This may be the reason for faster recombination in the cells with thicker photoelectrodes. The presence of Gerischer impedance confirms that the electron recombination reaction is faster than the transport of charge carriers through the film. This fact can explain why measured short circuit currents were very low, thus contributing to low conversion efficiencies for the assembled solar cells. In the Bode phase diagram (Figure 5.15c), there is a shift of frequency peaks in order of increasing thickness. The cell with photoelectrode films of 5.5μm yielded the longest electron lifetime compared to cells of thicker films. Longer lifetime means more electrons reached the photoelectrode and hence conducted to external circuit.

Figure 5.15b shows the Bode plot of impedance varying with frequency for various film thicknesses. It shows the transition of the high impedance values at low frequencies (0.1-100Hz) to low impedances at high frequencies (100-10,000Hz). The measured values of series resistance (R_S), parallel resistance (R_P or R_{ct}) and constant phase element (CPE) are recorded in Table 5.5 The calculated values of electron lifetime of electron in the cell and the cell efficiencies are also shown.

It was observed in Table 5.5, that as the thickness of the films increased, so did the values of series resistances. Films with low series resistances produced high electron lifetimes. From Table 5.5, it was also observed that the shunt resistances decreased with increasing film thickness. The electron lifetimes were low for low shunt resistances. The best performing cell had the lowest series resistance and highest shunt resistance and highest electron lifetime. Shorter electron lifetimes could have resulted from slow diffusion of electrons through the composite film and hence higher probability of recombination between electrons and electron-accepting species in electrolyte.

Table 5.5: Values of equivalent circuit model elements (EIS) compared with R_s *and* R_{sh} (I-V) for DSSCs based on TiO_2/Nb_2O_5 composite photoelectrodes deposited by EPD

method at 35V, from 0.25g/L and at different deposition times (thus different film thicknesses). Also shown are the calculated values of electron lifetimes.

Thickness, (μm)	R_s *(I-V)* (kΩ)	R_{sh} *(I-V)* (kΩ)	*CPE* (μF)	R_p *(EIS)* (kΩ)	R_s *(EIS)* (kΩ)	Electron lifetime τ_n	Efficiency η (%)
5.5	0.034	13.859	6.627	4.532	4.507	5.08	1.99
9.1	0.045	10.665	6.633	4.531	4.507	2.86	0.79
11.1	0.051	5.406	9.295	5.949	5.886	2.85	0.70
12	0.104	9.681	6.633	4.531	4.507	1.76	0.09

5.15 Influence of the Electrophoretic Deposition Time on DSSC Cell Efficiency

Figure 5.16 shows the cell efficiencies versus EPD time for DSSCs using nanocrystalline TiO_2/Nb_2O_5 composite electrode thin films of varying thickness. By varying deposition time during electrophoretic deposition, films of varied thickness were produced. The short circuit current (I_{SC}) obtained in the cell with photoelectrode film deposited at 90 s was higher than the currents obtained in cells using films of other deposition times. These high I_{SC} values were proportional to high cell efficiencies. The efficiency (1.99%) for cell deposited at 90 s (5.5 μm) was the highest obtained (Figure 5.16). DSSCs are generally known to possess a slow response for photocurrent generation by incident light. However, low J_{SC} values and therefore low cell efficiencies could be attributed to insufficient time allowed to complete photocurrent generation.

Table 5.6 shows solar cell characteristics (V_{OC}, J_{SC}, *FF* and efficiency) of dye-sensitized solar cells fabricated using TiO_2/Nb_2O_5 composite thin films deposited at varying EPD deposition times. With increasing photoanode film thickness from 5.5 to 12 μm, the open circuit voltage (V_{OC}) remained approximately constant at 0.6 V, whereas, short circuit current (J_{SC}) decreased from 5.25 to 0.2 mA/cm^2. We obtained maximum *FF* of 0.65 and conversion efficiency of 1.99 % for the DSSC using 5.5 μm thick composite films deposited and deposited for 90s. The slow response of DSSCs is most probably related to slow diffusion rate of electron across the semiconductor film (Tyagi *et al*., 2013). The films deposited for longer times (> 90 s) resulted in formation of films relatively thicker than those deposited for shorter deposition times (< 90 s). The relatively thin composite films prepared by controlling

the concentration, potential and deposition time resulted in a decreased electron transport distance and decreased electron recombination losses.

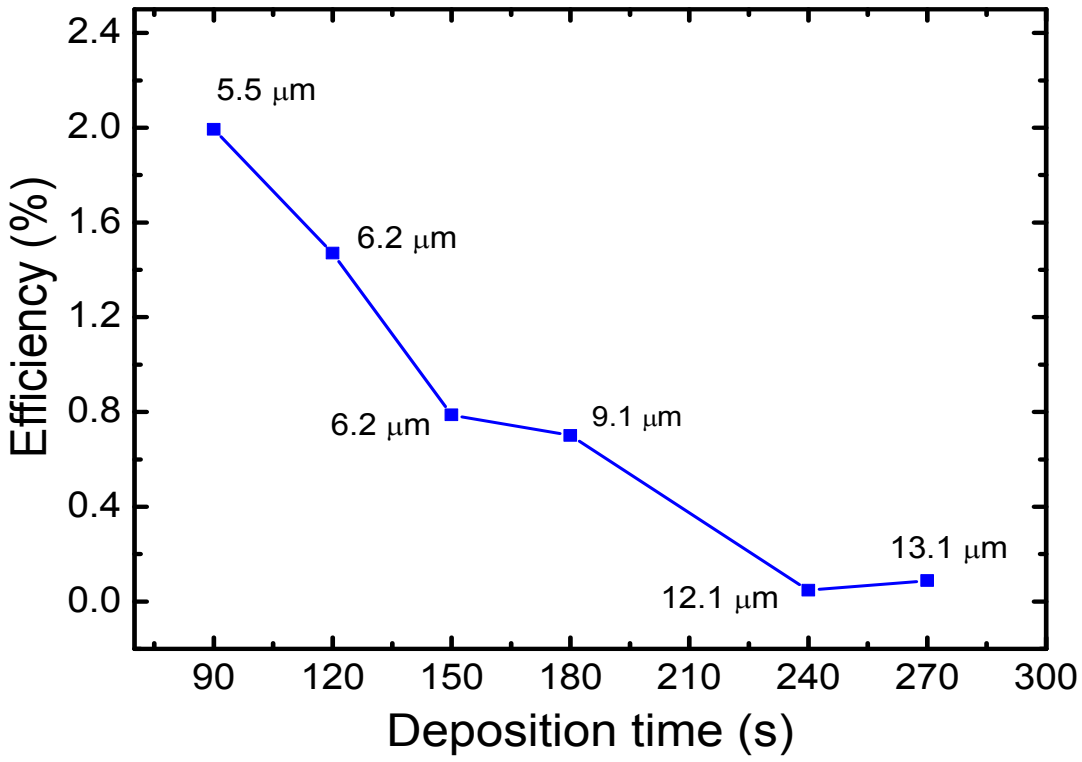

Figure 5.16: Cell efficiency versus deposition time for DSSCs fabricated using nanocrystalline TiO_2/Nb_2O_5 composite electrode thin films the films were deposited using electrophoretic technique using applied voltage of 35V and particle concentration of 0.25g/L.

Thicker nanoparticulate TiO_2 films adsorb relatively more N719 molecules leading to the enhancement in the photocurrent of the DSSC. However, thicker TiO_2/Nb_2O_5 composite films are less transparent which negatively affects light harvesting and the performance of the DSSC (Wu *et al*., 2012). In general, the efficiencies decreased with increasing deposition time (Figure 5.16). This decrease in efficiency with film-deposition time could be attributed to development of an insulating layer on the substrate and the reduction of potential on the surface of deposited layer. Chou *et al*., (2014), deposited TiO_2 film on FTO coated glass substrate by electrophoretic deposition method (EPD) and obtained efficiency of 2.76% for their dye-sensitized solar cells for deposition time of 60 s.

Table 5.6: Solar cell characteristics of DSSCs using TiO_2/Nb_2O_5 composite electrode films deposited at varying EPD deposition time, using 35V applied voltage and 0.25g/L particle concentration. The active area of each cell was 0.49 cm^2.

Process EPD deposition time (s)	Film thickness (μm)	V_{OC} (V)	J_{SC} (mA/cm^2)	*FF*	Efficiency η (%)
90	**5.5**	**0.66**	**5.25**	**0.57**	**1.99**
120	6.2	0.63	3.83	0.61	1.47
150	6.6	0.69	2.08	0.55	0.79
180	9.1	0.66	1.8	0.58	0.7
240	12.1	0.58	0.13	0.65	0.05
270	12.0	0.65	0.23	0.59	0.09

Several authors (Shin *et al*., 2010, Chou *et al*., 2014, Chang *et al*., 2013, Hamadanian *et al*., 2013) have reported characteristics for DSSCs in which efficiency varied from 0.07 to 4.89% as outlined in literature review (Table 2.1). These authors used nanoparticle (nP) titanium dioxide to fabricate the cells unlike in this work where composite of TiO_2 and Nb_2O_5 were used. In particular, Yum *et al*., (2005), assembled a dye-sensitized solar cell using electrophoretically deposited TiO_2 films and obtained fill factor and efficiency of 50% and 1.03% respectively.

5.16 Influence of Particle Concentration on DSSC Efficiency

Figure 5.17 shows a plot of cell efficiencies versus particle concentration in the EPD suspension, for DSSCs using nanocrystalline TiO_2/Nb_2O_5 composite electrode thin films of varying thickness. The films were deposited using electrophoretic method at deposition time of 90s and applied voltage of 35V. A mixed-composite structure was employed to form TiO_2/Nb_2O_5 composite thin films. The dye-sensitized soar cells fabricated with particle concentration in range 0.25 to 0.75 g/L showed a gradual decrease in efficiency with increasing concentration and corresponding film thickness. The solar cell characteristics such as fill factor, short-current density, open-circuit voltage and efficiency, of DSSC using nanocrystalline Nb_2O_5/TiO_2 composite electrode thin films deposited using varying particle concentration are recorded in Table 5.7. With increasing photoanode film thickness from 5.5

to 9.3 μm, the open circuit voltage (V_{OC}) decreased from 0.66 to 0.52 V, whereas, short circuit current (J_{SC}) decreased from 5.25 to 0.75 mA/cm^2.

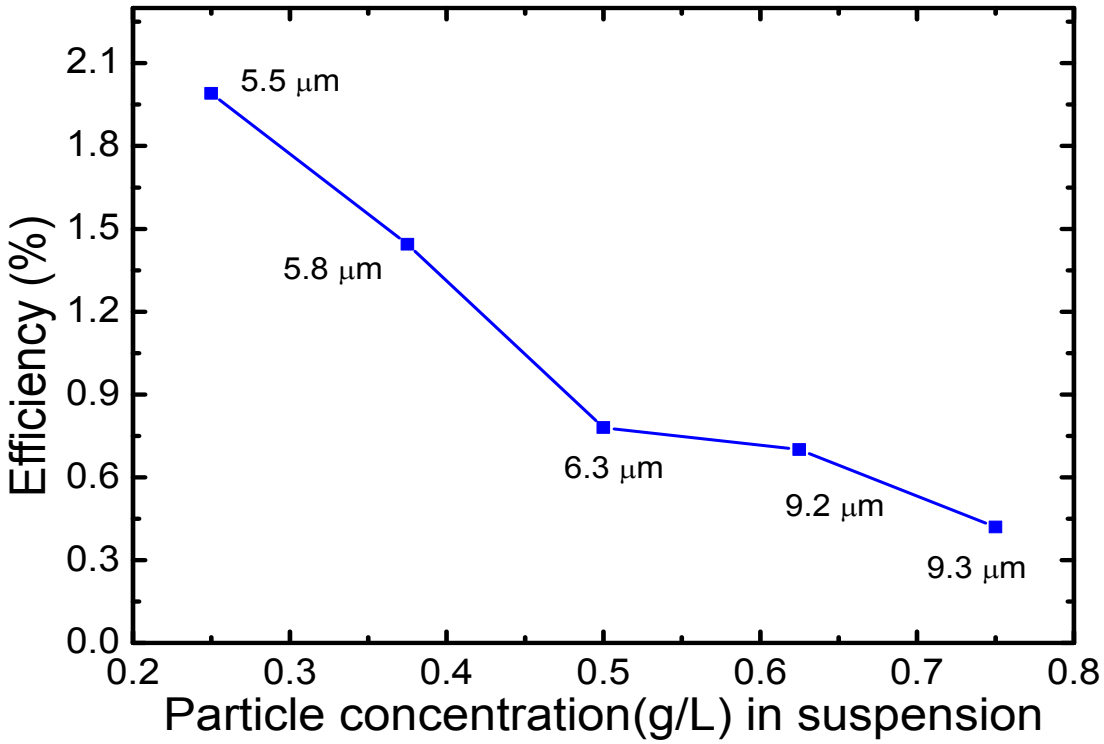

Figure 5.17: Cell efficiency versus particle concentration for DSSCs using nanocrystalline TiO_2/Nb_2O_5 composite electrode thin films. The films were deposited using electrophoretic method using deposition time of 90s and applied voltage of 35V.

Table 5.7: Solar cell characteristics of DSSCs using TiO_2/Nb_2O_5 composite electrode thin films deposited from varying EPD particle concentration, applied DC voltage of 35V and deposition time of 90s.The active area of each cell was 0.49cm^2.

EPD-electrode concentration (g/L)	Film thickness (μm)	V_{OC} (V)	J_{SC} (mA/cm^2)	*FF*	Efficiency η (%)
0.25	**5.5**	**0.66**	**5.25**	**0.57**	**1.99**
0.38	5.8	0.51	2.74	0.51	1.44
0.50	6.3	0.50	1.54	0.49	0.78
0.63	9.2	0.52	1.31	0.51	0.70
0.75	9.3	0.52	0.75	0.53	0.42

The obtained maximum *FF* was 0.65 and conversion efficiency of 1.99 % for the DSSC using 5.5 μm thick composite electrode thin films deposited using particle concentration of 0.25g/L. The maximum efficiency was acquired for DSSC with photoelectrode composite

films of low thickness (5.5 μm), prepared using EPD suspension of low particle concentration. Films prepared using high particle concentration could have developed lesser surface area than the films of low particle concentration due to increased packing density. Generally, the packing density could be enhanced by the increase in the refractive index of film (Sharma *et al*., 2009). The packing density (p) of TiO_2/Nb_2O_5 composite thin films deposited by Electrophoretic technique was calculated using Equation (5.1) (Raja *et al*., 2013)

$$p = \frac{5}{3}\left[\frac{n^2 - 1}{n^2 + 1}\right] \tag{5.6}$$

where n is the refractive index of TiO_2/Nb_2O_5 composite thin films. The value of n =1.643 for the composite films was substituted into Equation (5.1) and a value of 0.76 was obtained as the packing density (p) of the films. This level of porosity could have contributed to low dye loading leading to low short-circuit current density as was also observed by (Jose *et al*, 2009). Low current density could have resulted from reduced surface area for dye adsorption due to niobium pentoxide large unit cell dimensions (a = 0.361nm, b = 0.361nm, c = 0.393 nm and β = 90° (XRD JPDS card no. 28-0317 Nb_2O_5). The reduced efficiency at higher concentrations was possibly caused by particle coagulation. These results are consistent with findings by Dickerson & Boccaccini, (2012), that for concentrations above a critical value, the repulsive forces were overcome by the attractive Van der Waals forces resulting in coagulation.

5.17 Influence of EPD Applied Voltage on DSSC Efficiency

Figure 5.18 shows a plot of cell efficiencies versus EPD applied voltage for DSSCs using nanocrystalline TiO_2/Nb_2O_5 composite electrode thin films of varying thickness. The films were deposited using electrophoretic method from particle concentration of 0.25gL and at deposition time of 90s. The EPD applied voltage was varied from 15 to 60 V. The solar cell characteristics such as fill factor, short-current density, open-circuit voltage and efficiency, of the dye-sensitized solar cells using electrophoretically deposited nanocrystalline Nb_2O_5/TiO_2 composite films of varying applied voltage are recorded in Table 5.8.

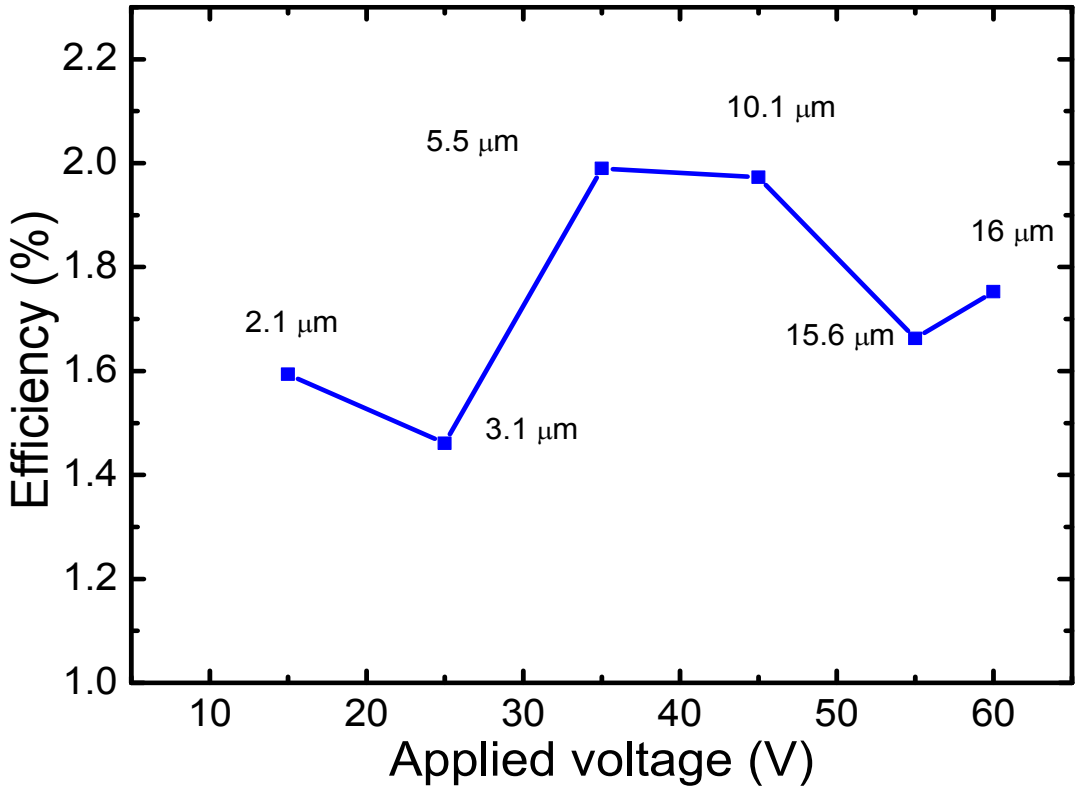

Figure 5.18: Cell efficiency versus applied voltage for DSSCs using nanocrystalline TiO_2/Nb_2O_5 composite films. The films were deposited using electrophoretic method from particle concentration of 2.5g/L and deposition time of 90s. The joining curve is for guiding the eye.

The maximum efficiency (1.99%) was generated by cells with composite films deposited at 35V. At high voltages, deposited film became denser due to increase in packing density of the particles in the film. Similar findings were reported by Yum *et al*., (2005).

Table 5.8: Solar cell characteristics of DSSCs using TiO_2/Nb_2O_5 composite electrode thin films deposited by varying EPD applied voltage , from 0.25g/L particle concentration and at 90s deposition time. The active area of each cell was 0.49 cm^2.

EPD Applied Voltage (V)	Film thickness (μm)	V_{OC} (V)	J_{SC} (mA/cm^2)	*FF*	Efficiency η (%)
15	2.1	0.49	3.47	0.46	1.59
25	3.1	0.486	3.07	0.48	1.46
35	5.5	0.661	5.25	0.57	1.99
45	10.1	0.519	3.78	0.49	1.97
55	15.6	0.65	6.19	0.41	1.66
60	16.0	0.707	3.89	0.60	1.66

Table 5.9 shows a comparison of dye-sensitized solar cells characteristics with those reported by other authors. It was observed that V_{OC} for the composites based cells increased slightly. The increased was attributed to an increase in Nb_2O_5 content in the composite. The high values of V_{OC} (> 0.6 V) were possibly due to higher conduction band of Niobium pentoxide.

Table 5.9: Comparison of DSSC parameters with those reported by other authors.

Film structure	V_{OC} (V)	J_{SC} (mA/cm^2)	*FF*	Efficiency, η (%)	Reference
$50TiO_2/50Nb_2O_5$ composite	**0.660**	**5.25**	**0.57**	**1.99**	**In this study**
$80TiO_2/20Nb_2O_5$composite	0.645	6.83	0.42	1.9	Eguchi, (2000)
$TiO_2/0.1Nb_2O_5$ Doped	0.841	3.1	0.69	1.8	Rajan, (2009)

CHAPTER SIX

CONCLUSIONS AND RECOMMENDATIONS

6.0 Conclusion

The following conclusions were drawn from the discussion of data done in this thesis:

1. TiO_2/Nb_2O_5 composite electrode thin films were successfully deposited by electrophoretic technique, sensitized and used to assemble dye-sensitized solar cells. Electrophoretic deposition (EPD) process parameters which include concentration, applied voltage and deposition time, were successfully optimized in this study for deposition of TiO_2/Nb_2O_5 composite electrode thin films. The optimized process related parameters of Electrophoretic deposition technique obtained were: particle concentration of 0.25 g/L, applied DC voltage of 35 V and deposition time of 90 s.

2. Optical transmittance was reduced with increase in film thickness. The highest optical transmittance obtained was 55% at wavelength (λ) of 1,300 nm for films 5.5 μm thick. The optical properties such as, optical band gap energy, extinction coefficient, and Urbach energy of the composite thin films were investigated in this study. The obtained band gap energies (E_g) for TiO_2/Nb_2O_5 composite films was 3.884eV and was found to be dependent on annealing time. The narrowing of band gap with increased annealing time was attributed to decrease in transitions due to reduction of the oxygen defect width as a result of air annealing which fills up the vacant oxygen levels. A value of 0.0354 for extinction coefficient (k), was obtained and associated with low absorption of light by the TiO_2/Nb_2O_5 composite electrode thin films due to their large energy band gap. The Urbach energy value of 434meV obtained in this study was significant in indicating the introduction of tail states at band edges that influence electron transport.

3. Electrical properties which included the type (polarity) of charge carriers and density of charge carriers (n_d) and were determined for the fabricated composite films. The Hall Effect measurements showed the majority carriers in the TiO_2/Nb_2O_5 composite films to be electrons (n-type). This polarity could have been caused by incorporation of Nb^{+5}, and O^{-2} ions in the composite. The charge carrier density (n_d) values of TiO_2/Nb_2O_5

composite thin films were found to be lower than those reported in literature due to electrons trapping in surface states of the high surface area composite film.

4. The Dye-sensitized solar cell characteristics were dependent on film thickness. The best performing DSSC based on TiO_2/Nb_2O_5 composite electrode thin films was fabricated using 5.5 μm thick composite films and produced open circuit voltage (V_{OC}) of 0.66 V, short circuit current density (J_{SC}) of 5.25 mA/cm^2, fill factor (*FF)* of 57%, and light-to-electric energy conversion efficiency of 1.99% (η ~ 2%) under 100 mW/cm^2 at AM 1.5 illumination.

5. The low cell efficiency was attributed to high recombination rate of the electrons injected into the film. Electrochemical impedance spectroscopy (EIS) measurements showed that the injected electrons in the TiO_2/Nb_2O_5 composite films had a short electron lifetime so that they recombined with electrolyte before reaching the FTO. Cells with thin films yielded the longest electron lifetime compared with cells of thicker films implying that more electrons reached the photoelectrode in thinner films

6. In all the cells, the EIS measurements showed the Gerischer impedance (R_D) with Nyquist plot having a single, central main arc in which charge transfer resistance between the TiO_2/Nb_2O_5 composite films and the electrolyte was lower than transport resistance of electrons within the composite film plus resistance at film/FTO interface. Impedance was attributed to the charge recombination with electrolyte species being faster than the electron transport within the TiO_2 film. The faster charge recombination could have been caused by the relatively poor adhesion of the film on to FTO glass slides. The poor adhesion was demonstrated by scratching the TiO_2/Nb_2O_5 composite films from the FTO-coated glass slides which resulted in easily peeled off film. The poor adhesion introduced high transport resistance and low interfacial resistances. Blocking the electron leak by structural modification by developing a more compact composite structure and improved film/FTO glass adherence that enhances electron conduction across the interface may be a possible way to obtain high JSC s and efficiencies in DSSCs.

6.1 Suggestions for Further Work

The following aspects are recommended for further research for improvement of the EPD technique and solar cell;

1) Synthesize additives to suspension of TiO_2/Nb_2O_5 and 2-propanol to enhance adhesion of composite film to the substrate.

2) Design pulsed DC EPD to investigate effect of frequency as process parameter in enhancing pore generation of deposited films.

3) Fabricate DSSCs that integrate composite electrode films with newly developed cobalt (II/III) based electrolyte rather than electrolyte based on iodide/triiodide that has the limitations of low open circuit voltage and corrosion of electrodes.

4) Synthesis of new charging agents to modify optical and electrical properties of metal-oxide nanoparticles when suspended in a liquid. Successful deposition of nanoparticle films by electrophoretic technique is dependent on charging mechanism employed. The new charging agents for non-agglomerated particles in EPD process could facilitate formation of composite films. Such films could be applied in diverse fields like photovoltaic, batteries, capacitors, and sensors coatings.

REFERENCES

Adachi, M., Sakamoto, M., Jiu, J., Ogata, Y., and Isoda, D. (2006). Determination of parameters of electron transport in dye-sensitized solar cells using electrochemical impedance spectroscopy. *Journal of Physical Chemistry B*, **110**(28), 13872–13880.

Ahmadi, S., Asim, N., Alghoul, M., Hammadi, F., Saeedfar, K., Ludin, N., Zaidi, S., and Sopian, K. (2014). The role of physical techniques on the preparation of photoanodes for dye-sensitized solar cells. *Hindawi, International Journal of Photoenergy*, **2014**, ID 198734, 1-19.

Asim, N., Ahmadi, S., Alghoul, M., Hammadi, F., Saeedfar, K., and Sopian, K. (2014). Research and development aspects on chemical preparation techniques of photoanodes for dye-sensitized solar cells. *Hindawi, International Journal of Photoenergy*, **2014**, ID 518156, 1-21.

Ata, W., Liu, Y., and Zhitomirsky, I. (2014). A review of new methods of surface chemical modification, dispersion and electrophoretic deposition of metal oxide particles. *Royal Society of Chemistry*, DOI: 10.1039/C4RA02218A, 1-56.

Autolab Application Note, 2012.

Awais, M., Rahman, M., and Don, J. (2011). Deposition and characterization of NiO_x coatings by magnetron sputtering for application in dye-sensitized solar cells. *Surface and Coatings Technology*, **204**(16), 2729-2736.

Bandy, J., Zhang, Q., and Cao, G. (2011). Electrophoretic deposition of titanium oxide nanoparticle films for dye-sensitized solar cell applications. *Materials Sciences and Applications*, **2**(10), 1427-1431.

Basu, R., Randall, C., and Mayo, M. (2001). Fabrication of dense zirconia electrolyte films for tubular solid oxide fuel cells by electrophoretic deposition. *Journal of American Ceramics Society*, **84**(1), 33–40.

Benehkohal, N. (2013). *Innovations in electrophoretic deposition of nanotitania-based photoanodes for use in dye-sensitized solar cells.* PhD Thesis, McGill University.

Benno, G., and Joachim, K. (2003). Optical properties of thin semiconductor films. http://home.fnal.gov/~jkopp/tum/pdf/F/hl_spekt.pdf (accessed on 3/31/2014)

Besra, L., and Liu, M. (2007). A review of fundamentals and applications of electrophoretic deposition (EPD). *Progress in Materials Science*, **52**(1), 1-61.

Bingwen, J., Manhua, Z., and Tao, S. (1997). *Advances in dye-sensitized solar cell*. Chinese Academy of Sciences, China.

Bisquert, J., (2002). Theory of the impedance of electron diffusion and recombination in a thin layer. *Journal of Physical Chemistry B,* **106**, 325-333.

Bisquert, J., and Fabregat-Santiago, F. (2010). Impedance spectroscopy: A general introduction and application to dye-sensitized solar cells, in *Dye-Sensitized Solar Cells*, K. Kalyanasundaram, Ed., p. 457-547, CRC; Taylor & Francis, Fla., USA.

Bisquert, J., Fabregat-Santiago, F., Mora-Sero, I., Garcia-Belmonte, G., and Gimenez, S. (2009). Electron lifetime in dye-sensitized solar cells: Theory and interpretation of measurements. *Journal of Physical Chemistry C,* **113**, 17278-17290.

Bisquert, J., Garcia-Belmonte, G., Fabregat-Santiago, F., Ferriols, N., Bogdanoff, P., and Pereira, E. (2000). Doubling exponent models for the analysis of porous film electrodes by impedance relaxation of TiO_2 nanoporous in aqueous solution. *Journal of Physical Chemistry B,* **104**(10), 2287-2298.

Blasing, T., (2014). Recent greenhouse gas concentrations, carbon dioxide information analysis center, DIO:10.3334.

Boccaccini, A., Klein, S., Ma, R., Li, Y., and Zhitomirsky, I. (2010). Electrophoretic deposition of biomaterials. *Journal of the Royal Society Interface,* **7**(5), S581-S613.

Born M., and Wolf, E. (2005). *Principles of Optics*. 7th Edition, Cambridge University Press, New York, 33. ISBN:1139643401.

Boschloo, G., and Hagfeldt, A. (2009). Characteristics of the iodide/triiodide red-ox mediator in dye-sensitized solar cells. *Accounts of Chemical Research,* **42**(11), 1819-1826.

Bowden, S., Honsberg, C., and Schroder, D. (2010). Moore's Law of Photovoltaics. *Future Photovoltaics*, 1-6.

BP- statistical review of world energy reports, 2015 pdf. Accessed on 02/04/2016.

Bridge technologies, a division of Four point probes. www.bridgetec.com/srm. accessed on 3/6/2012.

Burschka, J., Pellet, N., Moon, S-J., Humphry-Baker, R.., Gao, P., Nazeeruddin, M., and Gratzel, M. (2013). Sequential deposition as a route to high-performance perovskite-sensitized solar cells. *Nature*, **499**, 316-319.

Cabanas-Polo, S., and Boccaccini, A. (2015). Electrophoretic deposition of nanoscale TiO_2: technology and applications. *Journal of the European Ceramic Society*, article in press: accessed on 2/3/2017. http://dx.doi.org/10.1016/j.jeurceramsoc.2015.05.030.

Caglar, M., Ilican S., and Caglar, Y. (2006). Determination of the dispersive optical constants of the non-crystalline ZnO thin films. *Physica Macedonica,* **56**, 49-55.

Callister, W., and Rethwisch, D., (2010). *Material Science and Engineering.* 8th Edition, John Wiley & Sons, Incorporated. ISBN: 9780470928202.

Chang, H., Chen, T-L., Chen, S., Jwo, C., and Huang, K. (2009). Dye-sensitized solar cells made with TiO_2-coated multi-wall carbon nanotubes and natural dyes extracted from Ipomoea. *Materials Transactions,* **50**(12), 879-2884.

Chen, C-Y., Mingkui, M., Grätzel, C., Zakeeruddin, S., and Grätzel, M., (2009). Highly efficient light-harvesting ruthenium sensitizer for thin-film dye-sensitized solar cells. *American Chemical Society Nano,* **3**(10), 3103-3109.

Chiu, W-H., Lee, K-M., and Hsieh, W-F. (2011). High efficiency flexible dye-sensitized solar cells by multiple electrophoretic depositions. *Journal of Power Sources*, **196**, 3683–3687.

Chou, C-S., Lin, Y-J., Yang, R-Y., and Liu, K-H. (2011). Preparation of TiO_2/NiO composite particles and their applications in dye-sensitized solar cells. *Advanced Powder Technology*, **22**(1), 31-42.

Choy, K. (2003). Chemical vapor deposition of coatings. *Progress in Materials Science*, **48**(2), 57–170.

Chung, J., Myoung, J., Oh, J., and Lim, S. (2012). Successive ionic layer adsorption and reaction of ZnSe shells for ZnO nanowire-based dye-sensitized solar cells. *Journal of Physics and Chemistry of Solids*, **73**(4), 535–539.

Cisneros, R., Beley, M., Lapicque, F. (2014). Electrochemical impedance model of a (low-cost) dye-sensitized solar cell. *Chemical Engineering Transactions,* **41**, 193-198.

Crabtree, G., and Lewis, N. (2007). Solar energy conversion. *Physics Today*, 37-43.

Das, S., Sudhagar, P., Nagarajan, S., Ito, E., Lee, S., Kang, Y., and Choi, W. (2012). Synthesis of graphene-CoS electro-catalytic electrodes for dye sensitized solar cells. *Carbon,* **50**(13), 4815–4821.

Dean, J. (1999). *Lange's Handbook of Chemistry*, 15th ed. McGRAW-HILL, INC., pp 5.103-5.126.

Deen, M., and Pascal, F. (2006). Electrical characterization of semiconductor materials and devices-review. *Journal of Material Science: Materials in Electronics,* **17**, 549-575.

Diamant, Y., Chen, S., and Zaban, A. (2003). Core–shell nanoporous electrode for dye sensitized solar cells: The effect of the $SrTiO_3$ shell on the electronic properties of the TiO_2 core. *Journal of Physical Chemistry B,* **107**(9), 1977–1981.

Diamant, Y., Melamed, O., and Zaban, A. (2004). Core-shell nanoporous electrode for dye-sensitized solar cells: The effect of shell characteristics on the electronic properties of the electrode. *Coordination Chemical Reviews,* **248**(13), 1271-1276.

Dickerson, J., and Boccaccini, A. (Editors) (2012). *Electrophoretic deposition of nanomaterials*, Springer, **50**, ISBN:978-1-4419-9730-2.

Durr, M., Rosselli, S., and Yasuda, A. (2006). Band-gap engineering of metal oxides for dye-sensitized solar cells. *Journal of Physical Chemistry B,* **110**(43), 21899-21902.

Eguchi, K., Hoga, H., Sekizawa, K., and Sasaki, K. (2000). Nb_2O_5-based composite electrodes for dye-sensitized solar cells. *Journal of the Ceramic Society Japan*, **108**(1264), 1067-1071.

Fabregat-Santiago, F., Bisquert, J., and Palomares, E. (2007). Correlation between photovoltaic performance and impedance spectroscopy of dye-sensitized solar cells based on ionic liquids. *The Journal of Physical Chemistry C,* **111**(17), 6550–6560.

Fabregat-Santiago, F., Bisquert, J., Boschloo, G., and Hagfeldt, A. (2005). Influence of electrolyte in transport and recombination in dye-sensitized solar cells studied by impedance spectroscopy. *Solar Energy Materials & Solar Cells*, **87**, 117–131.

Fabregat-Santiago, F., Garcia-Belmonte, G., Mora-Sero, I., and Bisquert, J. (2011). Characterization of nanostructured hybrid and organic solar cells by impedance spectroscopy. *Phys. Chem. Chem. Phys.*, **13**, 9083-9118.

Feist, T. and Davies, P. (1992). Calculated from ICSD using POWD-12++ Structure. *Journal of Solid State Chemistry*, **101**, 275.

Feltrin, A., and Freundlich, A. (2008). Material considerations for terawatt level development of photovoltaics. *Renewable Energy,* **33**, 180–185.

Feng, Y., Ji, X., and Duan, J. (2012). Synthesis of ZnO/TiO_2 core-shell long nanowire arrays and their application on dye-sensitized solar cells. *Journal of Solid State Chemistry*, **190,** 303–308.

Ferrere, S., Zaban, A., and Gregg, B. (1997). Dye-sensitization of nanocrystalline tin oxide by perylene derivatives. *Journal of Physical Chemistry B,* **101**(23), 4490–4493.

Figgemeier, E., and Hagfeldt, A. (2004). Are dye-sensitized nano-structured solar cells stable? An overview of device testing and component analyses. *International Journal of Photoenergy*, **6**(3), 127–140.

Fraser, I. (2011). *The Hall Effect*. University of British Columbia. Accessed on 5/26/2013 http://www.physics.ubc.ca/~phys409/labs/Hall_Effect_2011.pdf.

Frevel, R., (1955). The standard diffraction pattern of Nb_2O_5 (JCPDS card No. 30-0873). *Analytical Chemistry*, **27**, 1329: in Liu, M., Yau, C., Zhang, Y., (2015). Fabrication of Nb_2O_5 nanosheets for high-rate Lithium ion storage. *Applications Scientific Reports*, **5**, 8326.

Fu, Y., Jin, Z., Ni, Y., Du, H., and Wang, T. (2009). Microstructure, optical and optoelectrical properties of mesoporous nc-TiO_2 films by hydrolysis-limited sol-gel process with different inhibitors. *Thin Solid Films*, **517**(19), 5634–5640.

Ghrairi, N., and Bouaicha, M. (2012). Structural, morphological, and optical properties of TiO_2 thin films synthesized by electrophoretic deposition technique. *Nanoscale Research Letters*, **7**(1), 357-364.

Goetzberger, A., Knobloch, J., Vob, B., and Waddington, R. (1998). *Crystalline silicon solar cells*. John Wiley & Sons, NY, USA, 89.

Gould, M., and Lamont, C. (2010). *Examination of the optical band gap of various semiconducting materials.* Reed College, Portland, OR 97202.

Govindasamy, G., Murugasen, P., and Sagadevan, S. (2016). Investigations on the synthesis, optical and electrical properties of TiO_2 thin films by chemical bath deposition (CBD) method. *Materials Research*, **19**(2), 413-419.

Gratzel, M. (2005). Solar energy conversion by dye-sensitized photovoltaic cells. *Journal of Inorganic Chemistry*, **44**(20), 6841-6851.

Green, M., Ernery, K., Hishikawa, Y., Warta, W., Dunlop, E., Levi, and Ho-Baillie, A. (2017). Solar cell efficiency tables (version 49). *Progress in Photovoltaics: Research and Applications*, **25**, 3-13.

Hafez, H., Lan, Z., Li, Q., Wu, J. (2012). High efficiency dye-sensitized solar cell based on novel TiO_2 nanorod/nanoparticle bilayer electrode. *Nanotechnology, Science and Applications*, **3**, 45-51.

Hagfeldt, A., and Gratzel, M. (2000). Molecular photonics. *Accounts of Chemical Research*, **33**(5), 269–277.

Hall, D., Underhill, P. and Torkelson, J. (1998). Spin coating of thin and ultrathin polymer films. *Polymer Engineering and Science*, **38**(12), 2039-2045.

Hamadanian, M., Gravand, A., and Jabbari, V. (2013). High performance dye-sensitized solar cells achieved via electrophoretic technique by optimizing of photoelectrode properties. *Materials Science in Semiconductor Processing*, **16**, 1352-1359.

Hamaker, H. (1940). Formation of deposition by electrophoresis, in: Besra, L., and Liu, M. (2007). A review of fundamentals and applications of electrophoretic deposition. *Progress in Materials Science*, **52**(1), 1-61.

Han, L., Koide, N., Chiba, Y., and Mitate, T. (2004). Modeling of an equivalent circuit for dye-sensitized solar cells. *Applied Physics Letters*, **84**(13), 2433-2435.

Hara, K., Horiguchi, T., Kinoshita, T., Sayama, K., Sugihara, H., and Arakawa, H. (2000). Highly efficient photon-to-electron conversion with mercuro-chrome-sensitized nanoporous oxide semiconductor solar cells. *Solar Energy Materials and Solar Cells*, **64**(2), 115-134.

Hartnagel, H., Dawar, A., and Jain, A. (1995). *Semiconducting transparent thin films.* CRC PRESS, ISBN 10: 0750303220.

Hateef, A., Balawa, B., Saleh, A., and Mahmmod, M. (2012). Effect of the thickness on electrical properties of TiO_2 thin films prepared by thermal chemical spray pyrolysis. *Journal of Engineering Science, Technology and Innovation*, **1**(6), 175-179.

Hosaka, N., Sekiya, T., Satoko, C., and Kurita, S. (1997). *Journal of the Physical Society of Japan*, **66**, 877.

Hossain, M., Biswas, S., Takahashi, T., Kubota, Y., and Fujishima, A. (2008). Investigation of sputter-deposited TiO_2 thin films for the fabrication of dye-sensitized solar cells. *Thin Solid Films*, **516**(20), 7149-7154.

Ilican, S., Caglar, Y., & Caglar, M. (2008). Preparation and characterization of ZnO thin films deposited by sol-gel spin coating method. *Journal of Optoelectronics and Advanced Materials*. **10**(10), 2578-2583.

IRENA (2016). *Solar PV.* International Renewable Energy National Agency, http://www.irena.org/Publications. accesed on 2/2/2016.

Ito, S., Makari, Y., Kitamura, T., Wadab, Y., and Yanagida, S. (2004). Fabrication and characterization of mesoporous SnO_2/ZnO composite electrodes for efficient dye-sensitized solar cells. *Journal of Material Chemistry*, **14,** 385-389.

Ito, S., Murakami, T., and Comte, P. (2008). Fabrication of thin film dye-sensitized solar cells with solar to electric power conversion efficiency over 10%. *Journal of Thin Solid Films*, **516**(14), 4613-4619.

Jarernboon, W., Pimanpang, S., Manesiri, S., Swatsitang, E., and Amornkitbamrung, V. (2009). Optimization of titanium dioxide film prepared by electrophoretic deposition for dye-sensitized solar cell application, *Thin Solid Films*, **517**(16), 4663-4667.

Jennings, J., Li, F., and Wang, Q. (2010). Reliable determination of electron diffusion length and charge separation efficiency in dye-sensitized solar cells. *Journal of Physical Chemistry C*, **114**(34), 737–740.

Jennings, J., Liu, Y., Safari-Alamuti, F., and Wang, Q. (2012). Dependence of dye-sensitized solar cell impedance on photoelectrode thickness. *Journal of Physical Chemistry* C, **116**, 1556-1562.

Jeong, J., and Kim, H. (2011). Thickness effect of RF sputtered TiO_2 passivating layer on the performance of dye-sensitized solar cells. *Solar Energy Materials and Solar Cells*, **95**(1), 344-348.

Jewett, J., and Serway, R. (2010). *Physics for Scientists and Engineers with Modern Physics*. 8th ed., Brooks/Cole, ISBN: 1439048460, 847-849.

Jia, H-J., Cheng, S-Y., Wu, X-K., and Yang, Y-L. (2010). Effect of annealing temperature on optical properties of SnS:Ag thin films. *Nature Science*, **2**(3), 197-200.

Jiang, C., Koh, W., Leung, M., Hong, W., Li, Y., and Zhang J. (2013). Influences of alcoholic solvents on spray pyrolysis deposition of TiO_2 blocking layer films for solid-state dye-sensitized solar cells. *Journal of Solid State Chemistry*, **198**, 197–202.

Jin, Y., Kim, K., Kim, W., Jang, K., and Choi, H. (2012). The effect of RF-sputtered TiO_2 passivating layer on performance of dye-sensitized solar cells. *Ceramics International*, **38**(1), S505-S509.

Jose, R., Thavasi, V., and Ramakrishna, S. (2009). Metal oxides for dye-sensitized solar cells. *Journal of the American Ceramic Society*, **92**(2), 289-301.

Kalyanasundaram, K., and Gratzel, M. (2009). Efficient dye-sensitized solar cells for direct conversion of sunlight to electricity. *Material Matters*, **4**(4), 88-90.

Kawakita, M., Uchikoshi, T., Kawakita, J., and Sakka, Y. (2009). Preparation of crystalline-oriented titania photoelectrodes on I-TO glasses from a 2-propanol-2,4-pentanedione solvent by electrophoretic deposition in a strong magnetic field. *Journal of the American Ceramic Society*, **92**(5), 984-989.

Kay, A., and Gratzel, M., (1993). Artificial photosynthesis: Photosensitization of TiO_2 solar cell with chlorophyll derivatives and related natural porphyrins. *Journal of Physical Chemistry*, **97**, 6272.

Khoby-Shendy, S., Vaezi, M., and Ebadzadeh, T. (2012). Synthesis of TiO_2/SnO_2 core shell nanocomposite via sol-gel method. *International Journal of Modern Physics:* Conference Series, **5**, 251-256.

Kim, C., and Jeong, H. (2007). Band gap tuning in nanoporous TiO_2-ZrO_2 hybrid thin films. *Bulletin of the Korean Chemical Society*, **28**(12), 2333–2337.

Kim, K., Jang, S., Park, J., Vittal, R., and Kim, K. (2007). Enhancement in the performance of dye-sensitized solar cells containing ZnO-covered TiO_2 electrodes prepared by thermal-chemical vapor deposition. *Solar Energy Materials and Solar Cells*, **91**(4), 366–370.

Kitiyanan, A., and Yoshikawa, S. (2005). The use of ZrO_2 mixed TiO_2 nanostructures as efficient dye-sensitized solar cell electrodes. *Material Letters*, **59**(29), 4038-4040.

Kitiyanan, A., Kato, T., Suzuki, Y., and Yoshikawa, S. (2006). The use of binary TiO_2-GeO_2 oxide electrodes to enhanced efficiency of dye-sensitized solar cells. *Journal of Photochemistry and Photobiology: A*, **179**(2), 130–134.

Konig, K., Novak, S., Bele, M., Zorko, M., and Kobe, S. (2008). Influence of the suspension stability on the electrophoretic deposition of nanosized alumina and silica. *Hot nano topics*, 23-30.

Kopidakis, N., Neale, N., and Frank, A. (2006). Effect of an adsorbent on recombination and band-edge movement in dye-sensitized TiO_2 solar cells: evidence for surface passivation. *Journal of Physical Chemistry B*, **110**(25), 12485-12489.

Kovendhan, M., Joseph, D., Manimuthu, P., Ganesan, S., Maruthamuthu, P., Suthanthiraraj, S., Venkateswaran, C., and Mohan, R. (2011). Spray deposited Nb_2O_5 thin film electrodes for fabrication of dye-sensitized solar cells. *Transactions of the Indian Institute of Metals*, **64**(1), 185-188.

Krebs, F. (2009). Fabrication and processing of polymer solar cells: a review of printing and coating techniques. *Solar Energy Materials and Solar Cells*, **93**(4), 394–412.

Lee S., Noh, J., Han, H., Yim, D., Kim, D., Lee, J., Kim, J., Jung, H., and Hong, C. (2009). Nb-doped TiO_2 :A new compact layer material for TiO_2 dye-sensitized solar cells. *Journal of Physical Chemistry C*, **113**(16), 6878-6882.

Lee, J., Rahman, M., Sarker, S., Nath, N., Ahammad, A., and Lee, J. (2011). Metal oxides and their composites for the photoelectrode of dye-sensitized solar cells, *Advances in Composite Materials for Medicine and Nanotechnology*, **182**, 210-218.

Lee, K., Brewer, E., Christiano, C., Meyo, F., Miguel, E., Podolsky, M., Rosa, J., Wolfram, C. (2016). Electrification for "UnderGrid" households in rural Kenya. *Development Engineering* 1, 26–35.

Lee, S., Jun, Y., Kim, K., and Kim, D. (2001). Modification of electrodes in nanocrystalline dye-sensitized TiO_2 solar cells. *Solar Energy Materials and Solar Cells* **65**(1), 193-200.

Lemarchand, F., Gao, L., and Leguime, M. (2012). Exploitation of multiple incidences spectrometric measurements for thin film reverse engineering. *Optical Express*, **20**, 15734-15751.

Li, Z-Y., Akhtar, M., Kong, B-S., and Yang, O-B. (2012). Graphene application as a counter electrode material for dye-sensitized solar cell. *Materials Letters*, **86**, 96-99.

Luo, X., Kim J., Ahn, J., Lee D., Kim, J., Lee, D., Kim, S., (2016). Electrospraying-assisted rapid dye molecule uptake on TiO_2 nanoparticles for speeding up dye-sensitized solar cell fabrication. *Solar Energy Materials & Solar Cells* **144**, 411–417.

Luo, Y., Li, D., and Meng, Q. (2009). Towards optimization of materials for dye-sensitized solar cells. *Advanced Materials*, **21**(45), 4647-4651.

Maluta, E., (2010). *Simulations of dye-sensitized solar cells*. A PhD Thesis. University of Bath.

Mandic, D. (2015). *How spectral reflectance works*. Filmetrics Europe GmbH, Hauptstr. 42, 82008 Unterhaching, Germany

Matthew N., Morales, E., Cortes-Jacome, M., Antonio, J. (2009). TiO_2 thin films-influence of annealing temperature on structural, optical, and photocatalytic properties. *Solar Energy*, **83**(9), 1499-1508.

Matthew, J., Varghese, G., and Matthew, J. (2012). Effect of post-thermal annealing on the structural and optical properties of ZnO thin films prepared from a polymer precursor. *Chin. Phys. B*, **21**(7), 078104/1-8

Mehmood, U., Rahman, S-U., Harrabi, K., Hussein, I., and Reddy B. (2014). Recent advances in dye-sensitized solar cells. *Hindawi, Advances in Material Science and Engineering*, **2014**, ID 974782, 1-12.

Miyasaka, T., and Kijitori, Y. (2004). Low-temperature fabrication of dye-sensitized plastic electrodes by electrophoretic preparation of mesoporous TiO_2 layers. *Journal of Electrochemical Society*, **151**(11), A1767-A1773.

Musembi, R., (2009). *Fabrication and characterization of $In(OH)_xS_y$ modified highly structured $TiO_2/Pb(OH)_xS_y$/PEDOT:PSS eta solar cell, and study of its transport mechanisms*. PhD Thesis, University of Nairobi.

Narayan, M., and Raturi, A. (2012). Deposition and characterization of titanium dioxide films formed by electrophoretic deposition. *International Journal of Materials Engineering Innovation,* **3**(1), 17-31.

Nazeeruddin, M., Kay, I., Rodicio, A., Humprey-Baker, R., Muller, E., Liska, P., Vlachopoulos, N., and Gratzel, M. (1993). Conversion of light to electricity by *cis*-xzbis (2, 2′-bipyridyl-4,4′-dicarboxylate) ruthenium (II) charge-transfer sensitizers ($X=Cl^-,Br^-,I^-,CN^-$,and SCN^-) on nanocrystalline titanium dioxide electrodes. *Journal of the American Chemical Society,* **115**, 6382-6390.

NOVA, (2016). Impedance measurement tutorial- Autolab, pdf accessed on 1/2/2017.

Nowotny, M., Sheppard, L., Bak, T., and Nowotny, J. (2008). Defect chemistry of titanium dioxide application of defect engineering in processing of TiO_2-based photocatalysts. *Journal of Physical Chemistry C,* **112**(14), 5275-5300.

NREL, 2016. (National Renewable Energy Lab). Accessed on 2/2/2017. http://www.nrel.gov/ncpv/images/efficiency_chart.jpg

Nuryadi, R., and Aprilia, L. (2012). *The growth of TiO_2 Thin Layer using electrophoresis technique based on constant voltage method*. Proceeding of International Conference on Sustainable Energy Engineering and Application, 57-61.

Nyongesa, F., Nyaga, W., and Aduda, B. (2007). *Poster presented at the 6th Edward Bouchet-Abdus Salam Institute International Conference, iThemba LABS*, Cape Town, South Africa.

O'Regan, B., and Gratzel, M. (1991). A low-cost, high-efficiency solar cell based on dye-sensitized colloidal TiO_2 films. *Nature*, **353**(6346), 737-740.

Okuya, M., Nakade, K., and Kaneko, S. (2002). Porous TiO_2 thin films synthesized by a spray pyrolysis deposition technique and their application to dye-sensitized solar cells. *Solar Energy Materials and Solar Cells*, **70**(4), 425–435.

Oommen, R., Rajalakshmi, P., and Sudha, S. (2012). Optical characteristics of TiO_2 thin films sensitized with the natural dye of Clitoria Ternatea. *International Journal of Applied Physics & Mathematics*, **2**(6), 439-441.

Oskam, G., Bergeron, B., Meyer, G., Searson, P. (2001). Pseudohalogens for TiO_2 based dye-sensitized solar cells. *Journal of Physical Chemistry B*, **105**(29), 6867–6873.

Ouedraogo, B., and Savadogo, O. (2013). Electrophoretic deposition of alumina and nickel oxide particles. *Journal of Scientific Research & Reports*, **2**(1) 190-205.

Padera, F. (2013), *Measuring absorbance and refractive index of thin films with the PerkinElmer lambda 950/1050 high performance UV-Vis-NIR Spectrophotometers*, pdf. PerkinElmer, Shelton, USA.

Padinger, F., Brabec, C., Fromherz, T., Hummelen, J. and Sariciftci, N. (2000). Fabrication of large area photovoltaic devices containing various blends of polymer and fullerene derivatives by using the doctor blade technique. *Opto-Electronics Review*, **8**(4), 280–283.

Palomares, E., Clifford, J., Haque, S., Lutz, T. and Durrant, J. (2003). Control of charge recombination dynamics in dye-sensitized solar cells by the use of conformally deposited metal oxide blocking layers. *Journal of the American Chemical Society*, **125**(2), 475-482.

Palomares, E., Clifford, N., Haque, S., Lutz, T., and Durrant, J. (2002). Slow charge recombination in dye-sensitized solar cells (DSSC) using Al_2O_3 coated nanoporous TiO_2 films. *Chemical Communications*, **14**, 1464-1465.

Pan, K-Y., Lin, Y-H., Lee, P-S., Wu, J-M., and Shih, H. (2012). Synthesis of SnO_2-ZnO core-shell nanowires and their optoelectronic properties. *Hindawi Publishing Corporation Journal of Nanomaterials*, **2012**, ID 279245, 1-6.

Parakh N., and Garg, J. (1985). Temperature dependent electrical properties of niobium (v) oxide. *Proceedings of Indian National Science Academy*, **51**(5), 824-831.

Patil, P. (1999). Versatility of chemical spray pyrolysis technique. *Materials Chemistry and Physics*, **59**(3), 185–198.

Paula, L., Amaral, R., Murakami, N., Paniago, R., Machadoa, E., and Patrocinio, A. (2014). New layer-by-layer Nb_2O_5–TiO_2 film as an effective underlayer in dye-sensitised solar cells. *Royal Society of Chemistry Advances*, **4**, 10310-10316.

Pawar, S., Pawar, B., Kim, J., Joo, O., and Lokhande, C. (2011). Recent status of chemical bath deposited metal chalcogenide and metal oxide thin films. *Current Applied Physics*, **11**(2), 117–161.

Pengra, D., Stoltenbergy, J., Van Dyck, R., and Vilches, O. (2014). *The Hall Effect*. pdf.

Pentland, W. (2010). *Solar-powered tablets to target rural students*. Forbes.com, LLC. Synthesis of SnO_2-ZnO core-shell nanowires and their optoelectronic properties. *Journal of Nanomaterials*, **2012**, Article ID 279245, 1-7.

Pugliese D. (2014). *New insights in dye-sensitized solar cells: novel nanostructured photoanodes, metal-free dye, quasi-solid electrolytes and physics-based modeling.* PhD Thesis, Politecnico di Torino.

Qin, Y. and Peng, Q. (2011). Ruthenium sensitizers and their applications in dye-sensitized solar cells. *International Journal of Photoenergy*, **2012**, ID 291579, 1-21.

Quasching, V. (2005). *Understanding renewable energy systems*. Earthscan, London, 1-130.

Radice, S., Bradbury, C., Michler, J., and Mischler, S. (2010). Critical particle concentration in electrophoretic deposition. *Journal of European Ceramic Society*. **30**(5), 1079–1088.

Rahman, M., Nath, N., and Lee, J. (2015). Electrochemical impedance spectroscopy analysis of sensitization-based solar cells. *Israel Journal of Chemistry*, **55**, 990-1001.

Raja, J., Jang, K., Nguyen, H., Trinh, T., Choi, W., and Yi, J. (2013). Enhancement of electrical stability of a-IGZO TFTs by improving the surface morphology and packing density of active channel. *Current Applied Physics* **13,** 246-251.

Rani, R., Zoolfakar, A., Mullane, A., Austin, M., and Kalantar, Z. (2014). Thin films and nanostructures of niobium pentoxide: Fundamental properties, synthesis methods and applications. *Journal of Materials Chemistry A*, **2**, 15683-15703.

Roh, S., Mane, R., Min, S., Lee, W., Lokhande, C., and Han, S. (2006). Achievement of 4.51% conversion efficiency using ZnO recombination barrier layer in TiO_2 based dye-sensitized solar cells. *Applied Physics Letters*, **89**, 25351-2.

Rouhi, J., Mamat, M., Mahmud, S., and Mahmood, M. (2015). High-performance dye-sensitized solar cells based on morphology-controllable synthesis of ZnO-ZnS heterostructure nanocone photoanodes. *PLoS ONE*, **10**(4), 1-14.

Sanchez-Vergara, M., Alvarez-Bada, J., Perez-Baeza, C., Loza-Neri, E., Torres-Garcia, R., Rodrigueq-Gomez, A., and Alonso-Huitron, J. (2014). Morphological and optical

properties of dimetallo-phthalocyaninie-complex thin films. *Advances in Materials Physics and Chemistry*, **4**, 20-28.

Sancho-Parramon, J., Janicki, V., and Zorc, H. (2008). Compositional dependence of absorption coefficient and band gap for Nb_2O_5-SiO_2 mixture thin films. *Thin Solid Films*, **516**(16), 5478-5482.

Sanjeev, S., and Kekuda, D. (2015). Effect of annealing temperature on the structural and optical properties of Zinc oxide thin films prepared by spin coating process. *IOP Conf. Series: Materials Science & Engineering*, **73**, 1-5. doi:10.1088/1757-899X/73/1/012149

Sarkar, P., and Nicholson, P. (1996). Electrophoretic deposition: Mechanisms, kinetics and application to ceramics. *Journal of American Ceramic Society,* **79**(8), 1987-2002.

Sarkar, P., Datta, S., and Nicholson, P. S. (1997). Functionally graded ceramic/ceramic and metal/ceramic composites by electrophoretic deposition. *Composites Part B: Engineering*, **28**(1), 49–56.

Sarker, S., Ahammad, S., Seo, H-W., and Kim, D. (2014). Electrochemical impedance spectroscopy of dye-sensitized solar cells: Fundamentals and spreadsheet calculation. *International Journal of Photoenergy*, **2014**, ID 851705, 1-17.

Schiermeier, Q., Tollefson, J., Scully, T., Witze, A., and Morton, O. (2008). Energy alternatives: Electricity without carbon. *Nature,* **454**, 816-823.

Scriven, L. (1988). Physics and applications of dip coating and spin coating. *MRS Proceedings*, **121**, 717.

Sharma, R., Sehrawat, K., Wakahara, A., and Mehra, R. (2009). Epitaxial growth of Sc-doped ZnO films on Si by sol–gel route. *Applied Surface Science*, **255,** 5781–5788

Shin, I., Seo, H., Son, M-H., Kim, J-K., Prabakar, K., and Kim, H-J. (2010). Analysis of TiO_2 thickness effect on characteristic of a dye-sensitized solar cell by using electrochemical impedance spectroscopy. *Current Applied Physics*, **10**, S422–S424.

Shinde, P., and Bhosale, C. (2008). Properties of chemical vapour deposited nanocrystalline TiO_2 thin films and their use in dye-sensitized solar cells. *Journal of Analytical and Applied Pyrolysis*, **82**(1), 83–88.

Simiyu, J., (2010). *Characterization of Anthocyanin dyes and investigation of charge transport in TiO_2 dye-sensitized solar cells*. PhD Thesis, University of Nairobi.

Smestad, G., Krebs, F., Lambert, C., Granqvist, C., Chopra, K., Matthew, X., and Takakura, H. (2008). Solar cell efficiencies in solar energy materials and solar cells. *Solar Energy Materials & Solar Cells.* **92**(4), 371-373.

Snaith H. (2010). Estimating the maximum attainable efficiency in dye-sensitized solar cells. *Advanced Functional Materials,* **20**(1), 13–19.

Snaith, H., and Schmidt-Mende, L. (2007). Advances in liquid-electrolyte and solid-state dye-sensitized solar cells. *Advanced Materials,* **19**(20), 3187-3200.

Springer, S. (2004). *Free carriers in nanocrystalline titanium dioxide thin films.* Thesis, Ecole Polytechnique Federale de Lausanne (EPFL).

Sta, I., Jlassi, M., Hajji, M., Boujmil, M., Jerbi, R., Kandyla, M., Kompitsas, M., and Ezzaouia, H. (2014). Structural and optical properties of TiO_2 thin films prepared by spin coating, *Journal of Sol-Gel Science and Technology* ,**72**, 421-43.

Swanepoel, R. (1983). Determination of the thickness and optical constants of amorphous silicon. *Journal of Physics E: Scientific Instruments*, **16**, 1214-1222.

Tacchini, I., Anson-Casaos, A., Yu, Y., Martinez, M., and Lira-Cantu, M. (2012). Hydrothermal synthesis of 1-D TiO_2 nanostructures for dye sensitized solar cells, *Materials Science and Engineering B*, **177**(1), 19–26.

Takamoto T., Kaneiwa, M., Imaizumi, M., and Yamaguchi, M. (2005). InGap/GaAs-based multijunction solar cell. *Progress in Photovoltaics Research*, **13**(6), 495-511.

Tan, B., and Wu, Y. (2006). Dye-sensitized solar cells based on TiO_2 nanoparticle/nanowire composites. *Journal of Physical Chemistry B*, **110**(32), 15932 -15938.

Tang, H., Prasad, K., Sanjines, R., Schmid, P., and Levy, F. (1994). Electrical and optical properties of TiO_2 anatase thin films. *Journal of Applied Physics*, **75**(4), 2042-2047.

Tauc, J., Grigorovici, R., and Vancu, A. (1966). Optical properties and electronic structure of amorphous germanium. *Physica Status Solidi,* **15**, 627-637.

Teleki, A., Pratsinis, S., Kalyanasundaram, K., and Gouma, P. (2006). Sensing of vapors by flame-made TiO_2 nanoparticles. *Sensing Actuate, B-Chemistry*, **119**(2), 683-690.

Tepantlan, C., Gonzalez, A., and Arreola, I. (2008). Structural, optical and electrical properties of CdS thin films obtained by spray pyrolysis. *Revista Mexicana De-Fisica*, **54**(2), 112-117.

Tyagi, V., Rahim, N., Rahim N., and Selvaraj, J. (2013). Progress in solar PV technology: Research and achievement. *Renewable & Sustainable Energy Reviews*. **20**, 443-461.

Van der Biest, O., and Vandeperre, L. (1999). Electrophoretic deposition of materials. *Annual Reviews Material Science,* **29**(1), 327-352.

Van Tassel, J., and Randall, C. (2006). Mechanisms of electrophoretic deposition. *Key Engineering Materials,* **314**, 167-174.

Vilarinho, P., Fu, Z., Wu, A., and Kingon, A., (2013). Critical role of suspension media in electrophoretic deposition: The example of low loss dielectric $BaNd_2Ti_5O_{14}$ thick films. *The Journal of Physical Chemical* B, **117**, 1670-1679.

Waita, S., Aduda, B., Mwabora, J., Niklasson, G., Granqvist, C., and Boschloo, G. (2009). Electrochemical characterization of TiO_2 blocking layers prepared by reactive DC magnetron sputtering. *Journal of Electroanalytical Chemistry*, **637**(1-2), 79-83.

Wang, J., Jin, E., Park, J-Y., Wang, W., Zhao, X., and Gu, H-B. (2012). Increases in solar conversion efficiencies of the ZrO_2 nanofiber-doped TiO_2 photoelectrode for dye-sensitized solar cells, *Nanoscale Research Letters*, **7**(1), 98-105.

Wang, P., Zakeeruddin, S., Moser, J-E., Humphry-Baker, R., and Gratzel, M. (2004). Solvent-free, SeCN-/$(SeCN)^{3-}$ Based ionic liquid electrolyte for high-efficiency dye-sensitized nanocrystalline solar cells. *Journal American Chemical Society*, **126**, 7164-7175.

Wang, Q., Moser, J-E., and Gratzel, M. (2005). Electrochemical impedance spectroscopic analysis of dye-sensitized solar cells. *Journal of Physical Chemistry*, **109,** 14945-53

Weerasinghe, H., Huang, F., and Cheng, Y. (2013). Fabrication of flexible dye-sensitized solar cells on plastic substrates. *Nano Energy*, **2**(2), 174-189.

Wei, M., Qi, Z., Ichihara, M., and Zhou, H. (2008). Synthesis of single-crystal niobium pentoxide nanobelts. *Acta Materialia,* **56**(11), 2488-2494.

Wu, J., Cao, J., Han, W-Q., Janotti, A., and Kim, H-C. (Eds), (2012). Functional metal oxide nanostructures. *Springer Series in Materials Science*, **149**, 9930-9936.

Wu, S., Han, H., Tai, Q., Zhang, J., Xu, S., Zhou, C., Yang, Y., Hu, H., Chen, B., Sebo, B., and Zhao, X. (2008). Enhancement in dye-sensitized solar cells based on MgO-coated TiO_2 electrodes by DC magnetron sputtering, *Nanotechnology,* **19**, 1-6.

Xia, J., Masaki, N., Jiang, K., and Yanagida, S. (2007). Fabrication and characterization of thin Nb_2O_5 blocking layers for ionic liquid based dye-sensitized solar cells. *Journal of Photochemistry and Photobiology A*, **188**(1), 120–127.

Xue, Z., Zhang, W., Yin, X., Cheng, Y., Wang, L., and Liu, B. (2012). Enhanced conversion efficiency of flexible dye-sensitized solar cells by optimization of the nanoparticle size with an electrophoretic deposition technique. *RSC Advances*, **2,** 7074-7080.

Yacaman, M., Rendon, L., Arenas, J., and Puche, M. (1996). Maya Blue paint: An ancient nanostructured material. *Science*, **273**, 223-225.

Yakuphanoglu, F., Ilican, S., Caglar, M., and Caglar, Y. (2007). The determination of the optical band gap and optical constants of non-crystalline and crystalline ZnO thin films deposited by spray pyrolysis. *Journal of Optoelectronics and Advanced Materials.* **9**(7), 2180-2185.

Yan, L-T., Wu, F-L., Peng, L., Zhang, L-J., Li, J., Dou, S-Y., and Li, T-X., (2012). Photoanode of dye-sensitized solar cells based on a ZnO/TiO_2 composite film, *International Journal of Photoenergy*, **2012**, 1-4.

Yang, Z. (2011). *Fundamental studies of nano-architectured dye-sensitized solar cells.* PhD Thesis, Northern Illinois University.

Yavuz, H. (2014). *Design of high-efficiency dye-sensitized nanocrystalline solar cells*. PhD Thesis, Middle East Technical University.

Yella, A., Lee, H-W., Tsao, H., Yi, C., Chandiran, A., Nazeeruddin, M., Diau, E., Yeh, C-H., Zakeeruddin, S., and Gratzel, M. (2011). Porphyrin-sensitized solar cells with cobalt (II/III)-based red-ox electrolyte exceed 12 percent efficiency. *Science*, **334**(6056), 629-634.

Yum, J-H., Kim, S-S., Kim, D-Y., and Sung. Y-E. (2005). Electrophoretically deposited TiO_2 photo-electrodes for use in flexible dye-sensitized solar cell. *Journal Photochemistry and Photobiology A: Chemistry,* **173**(1), 1-6.

Zaban, A., Chen, S., Chappel, S., and Gregg, B. (2000). Bilayered nanoporous electrodes for dye-sensitized solar cells. *Chemical Communication (Cambridge)*, **22**, 2231-2232.

Zhang, Q., and Cao, G. (2011). Nanostructured photoelectrodes for dye-sensitized solar cells. *Nano Today*, **6**(1), 91-109.

APPENDIX A: XRD JPDS card no. 74-1940 TiO_2

Name and formula

Reference code:	01-074-1940
Compound name:	Titanium Oxide
Common name:	Titanium dioxide - (B)
ICSD name:	Titanium Oxide
Chemical formula:	TiO_2

Crystallographic parameters

Crystal system:	Monoclinic
Space group:	C2/m
Space group number:	12
a (Å):	12,1787
b (Å):	3,7412
c (Å):	6,5249
Alpha (°):	90,0000
Beta (°):	107,0540
Gamma (°):	90,0000
Calculated density (g/cm^3):	3,73
Volume of cell (10^6 pm^3):	284,22

Comments

ICSD collection code:	041056
Creation Date:	01/01/1970
Modification Date:	01/01/1970
ICSD Collection Code:	041056
Temperature of Data Collection:	REM TEM 17 C
Calculated Pattern Original Remarks:	REM M R(Bragg)=0.046, obtained by dehydration of $H_2Ti_3O_7$, sa
Calculated Pattern Original Remarks:	REM contained some anatase, PDF 46-1238 Test from ICSD: At least one TF implausible
Temperature Factor:	ITF. This entry was previously $TmBO_3$, ICSD 027942. The soft chemical synthesis of TiO_2 (B) from layered titanates. i6 (C12/M1). AX2.

Peak list

No.	h	k	l	d[A]	2Theta[deg]	I[%]
1	0	0	1	6,23799	14,187	60,1
2	2	0	0	5,82159	15,207	39,5
3	-2	0	1	5,06023	17,512	5,7
4	2	0	1	3,74354	23,749	8,1
5	1	1	0	3,56184	24,979	100,0
6	-1	1	1	3,22002	27,681	1,4
7	-2	0	2	3,16231	28,197	6,9
8	0	0	2	3,11900	28,597	50,6
9	-4	0	1	2,99582	29,799	34,7
10	1	1	1	2,98014	29,960	14,1
11	4	0	0	2,91080	30,691	10,2
73	-9	1	1	1,26799	74,817	1,0
74	6	2	1	1,26441	75,066	2,2
75	-6	2	3	1,25268	75,892	2,5
76	6	0	3	1,24760	76,257	1,8

No.	h	k	l	d[A]	2Theta[deg]	I[%]
77	3	1	4	1,24426	76,498	1,2
78	7	1	2	1,24154	76,696	6,3
79	1	3	0	1,23997	76,811	2,9
80	4	0	4	1,23239	77,371	0,2
81	-2	2	4	1,22918	77,611	0,6
82	-6	0	5	1,22559	77,881	0,4
83	-1	3	1	1,22265	78,104	0,4
84	-10	0	2	1,21363	78,797	1,0
85	-9	1	3	1,21037	79,050	0,9
86	-4	2	4	1,20756	79,271	4,3
87	-5	1	5	1,19783	80,044	0,6
88	8	0	2	1,19174	80,536	0,2
89	3	3	0	1,18728	80,901	0,8
90	-3	3	1	1,18605	81,003	1,0
91	-8	2	1	1,17935	81,560	0,4
92	-10	0	3	1,17309	82,089	0,4
93	-8	2	2	1,16881	82,454	2,5
94	-1	3	2	1,16432	82,842	1,0
95	6	2	2	1,15390	83,758	2,0
96	3	3	1	1,14758	84,325	0,6
97	1	1	5	1,14582	84,485	0,9
98	-3	3	2	1,14426	84,627	0,7
99	-6	2	4	1,14057	84,965	2,6
100	-9	1	4	1,12551	86,377	0,5
101	-8	0	5	1,12316	86,602	1,2
102	-8	2	3	1,12129	86,783	0,6
103	-5	3	1	1,10923	87,966	0,1
104	-10	0	4	1,10043	88,854	0,3
105	5	3	0	1,09860	89,041	0,2
106	7	1	3	1,09515	89,397	0,1

Stick Pattern

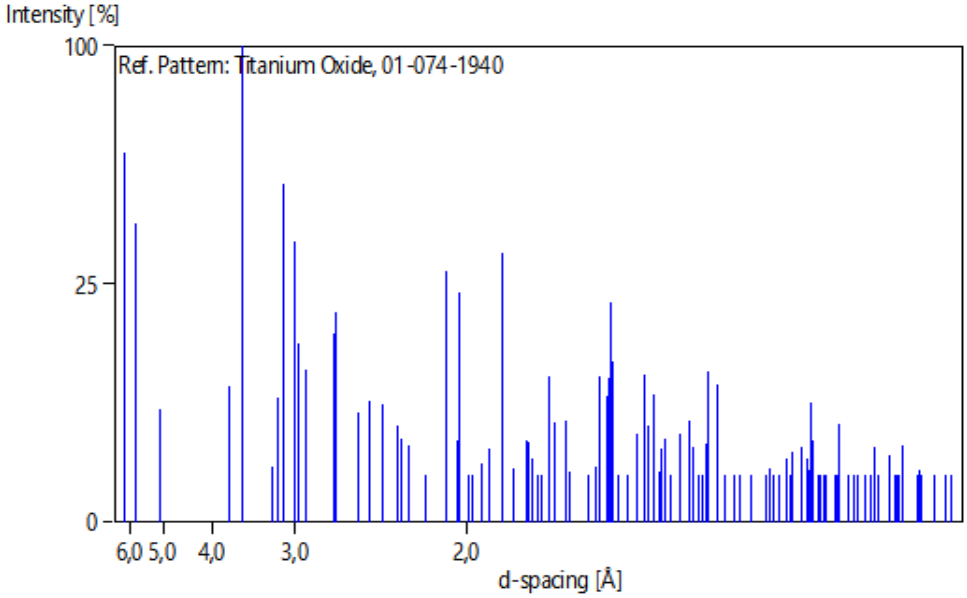

APPENDIX B: XRD JPDS card no. 28-0317 Nb_2O_5

Name and formula

Reference code:	00-028-0317
Compound name:	Niobium Oxide
PDF index name:	Niobium Oxide
Chemical formula:	Nb_2O_5

Crystallographic parameters

Crystal system:	Hexagonal
Space group:	P E
a (Å):	3,6070
b (Å):	3,6070
c (Å):	3,9250
Alpha (°):	90,0000
Beta (°):	90,0000
Gamma (°):	120,0000
Volume of cell (10^6 pm^3):	44,22

Comments

Creation Date:	01/01/1970
Modification Date:	01/01/1970
Comment:	Pattern at high pressure.

Peak list

No.	h	k	l	d[A]	2Theta[deg]	I[%]
1	0	0	1	3,93000	22,607	90,0
2	1	0	0	3,12000	28,587	100,0
3	1	0	1	2,44600	36,712	40,0
4	0	0	2	1,96200	46,234	30,0
5	1	1	0	1,80000	50,674	25,0
6	1	0	2	1,66300	55,187	30,0
7	1	1	1	1,63700	56,141	14,0
8	2	0	0	1,56500	58,971	12,0

Stick Pattern

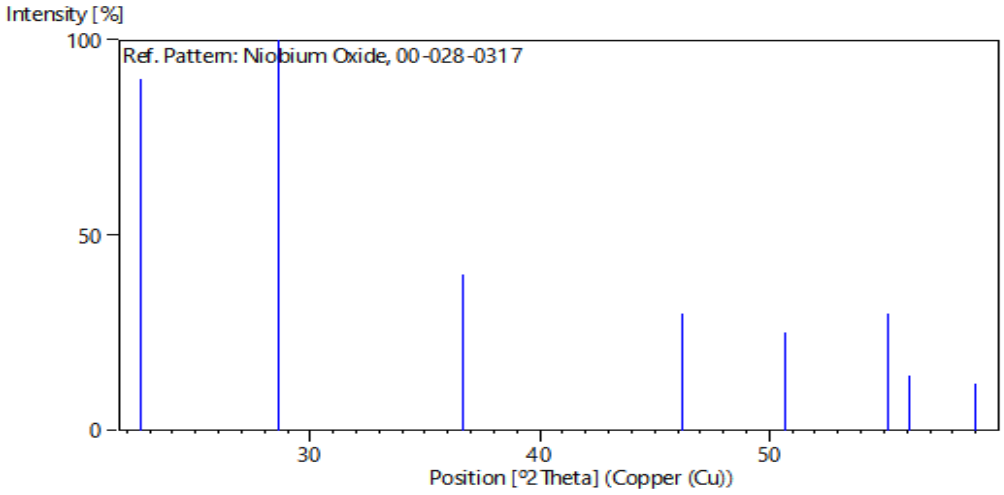

APPENDIX C: PUBLISHED PAPER I

Journal of Energy and Power Engineering 8 (2014) 757-764

Electrophoretic Deposition of TiO_2/Nb_2O_5 Composite Electrode Thin Films for Photovoltaic Application

John Njagi Ngau, Bernard Odhiambo Aduda, Francis Wanjala Nyongesa and Robinson Juma Musembi
Department of Physics, University of Nairobi, Nairobi, P.O.Box 30197-00100, Nairobi, Kenya

Received: September 27, 2013 / Accepted: November 14, 2013 / Published: April 30, 2014.

Abstract: Nano sized powders of TiO_2 (titanium dioxide) and Nb_2O_5 (Niobium (V) oxide) were used to fabricate TiO_2/Nb_2O_5 composites thin films by EPD (electrophoretic deposition) technique. The metal oxide powders, together with magnesium nitrate hexahydrate pellets, were suspended in propan-2-ol inside an EPD cell. The electrodes, placed 1.2 cm apart, were partially immersed in the suspension and a DC potential applied across them. Key EPD process parameters, which include applied DC electric field, deposition time and solid concentration in suspension, were optimized through visual inspection and from UV-Vis-NIR spectrophotometer spectra. The highest (55%) transmittance was obtained for films with deposition time of 90 s, powder concentration of 0.01 g/40 mL, and 35 V DC (direct current) voltage. XRD micrographs confirmed that TiO_2 and Nb_2O_5 particles were presented in the composite film. SEM (scanning electron microscope) micrographs of the composite electrode thin films showed that porous films of high quality with well controlled morphology were deposited by using the EPD technique.

Key words: Electrophoretic deposition, TiO_2/Nb_2O_5 composite electrode thin films.

1. Introduction

The development and application of RET (renewable energy technologies) is the focus of increased scientific research to help mitigate against challenges of climatic change and the possible depletion of the fossil fuels. Solar energy represents an important renewable energy resource which is carbon free and ubiquitous, with terrestrial potential about 600 TW. It is also useful for off-grid utilizations. The commonly used photovoltaic systems are crystalline silicon-based with positive attribute of high power conversion efficiencies (24.7%) [1]. However, these modules require vacuum-based techniques for fabrication resulting in high production costs. A lot of research is focused on developing solar cells that require low production costs and have adequate conversion efficiencies. Consequently, among the excitonic solar cells, the DSSC (dye-sensitized solar cells) have attracted widespread interest owing to their easy fabrication processes, low production costs, less sensitivity to impurities, wide range of temperature for optimal operation, compatibility with glass and flexible substrates and fair solar-to-electrical conversion efficiencies [2].

Whereas, DSSCs have achieved conversion efficiencies of 11.6% [3], there are obstacles to overcome in order to increase efficiency and make the cells reproducible on large scale. Dye sensitized solar cells contain a porous, semiconductor material (photoelectrode) which absorb dye molecules and conduct injected photoelectrons. The dye molecules play the role of capturing light photons by extending the optical adsorption spectrum of the wide energy gap ($Eg > 3$ eV) semiconductor. TiO_2 (titanium dioxide) is the most widely used semiconductor for preparing DSSC photoelectrodes because it provides high energy conversion efficiency [2]. The high efficiency is the result of titanium dioxide films providing ease of electron transmission through them, thus enhancing

Corresponding author: John Ngau, researcher, research field: condensed matter. E-mail: johnjagin@yahoo.com.

APPENDIX D: PUBLISHED PAPER II

International Journal of Innovative Research in Advanced Engineering (IJIRAE) ISSN: 2349-2163
Issue 2, Volume 2 (February 2015) www.ijirae.com

Electrical Characterization of Nano-TiO_2/Nb_2O_5 Composite Thin Films Deposited Using Electrophoretic Deposition Technique

J. N. Nguu[1*], B. O. Aduda[1], F. W. Nyongesa[1], R. J. Musembi[1], S. M. Njogu[1], P.M. Mwathe[2]
[1] Department of Physics, University of Nairobi, P. O. Box 30197-00100, Nairobi, Kenya
[2] Department of Physics, Kenyatta University, P. O. Box 43844-00100, Nairobi, Kenya

Abstract*— This paper reports the results of electrical characterization of TiO_2/Nb_2O_5 composite thin films. Uniform TiO_2 and Nb_2O_5 composites thin films were deposited on FTO coated glass substrate using electrophoretic deposition (EPD) technique. The EPD voltage of 35V (DC) and deposition time of 90s, were used for various volume fractions of Nb_2O_5 in composites. Uniform and crack free composite films were successfully deposited using the EPD technique as shown by the SEM micrographs. The Hall Effect equipment was used to characterize the films through measurement of current and the Hall voltage. Current against Hall voltage plot for films of various volume fractions of Nb_2O_5 were used to determine Hall coefficients and majority charge carrier density. The sign of Hall coefficient values revealed that TiO_2/Nb_2O_5 composite thin films had a net n-type polarity indicating electrons were the majority charge carrier in the composite films. The results showed that dye-sensitized solar cells should be fabricated with TiO_2/Nb_2O_5 composites thin films in ratio of 1:1 because such ratio 1:1 for TiO_2 and Nb_2O_5 in composite yielded the highest electron mobility in the films.

Keywords*— Electrical characterization, TiO_2/Nb_2O_5 composites, Electrophoretic deposition, thin films, Hall Effect,

I. INTRODUCTION

Metal oxide semiconductors have become increasingly important in fabrication of photoanodes used in dye-sensitized solar cell (DSSCs). The efficiency of a DSSC in converting light into electric energy depends on factors such as effectiveness with which light is transmitted through the photoanode, the number of electrons injected into the photoanode and the ease with which electrons are transported through the photoanode. Metal oxide semiconductors used in fabrication of dye-sensitized solar cells are chemically stable and environmentally friendly materials that provide porous films for the cells. High surface area of porous photoanode enhances light harvesting from the increased dye adsorption.

Titanium dioxide (TiO_2) has been the most preferred metal oxide semiconductor to fabricate photoanodes in dye-sensitized solar cells because it is a material that is non-toxic, easily available, of relatively low cost material, environmentally stable, and used to fabricate solar cells with high conversion efficiency [1]. Several studies have been initiated to modify the electrical transport properties of TiO_2 using binary-system electrodes [2]. The TiO_2/Nb_2O_5 systems have been prepared by several methods like the DC magnetron technique [3], sol gel technique [4], power screen printing [5], and pulsed laser deposition [6]. The electrophoretic deposition (EPD) technique has not been fully elucidated to deposit porous, thin films in binary-system electrodes. Electrophoretic deposition technique is a colloidal processing technique that uses electrophoresis mechanism for the movement of charged particles suspended in a solution under an electric field, to deposit them in an ordered manner on an oppositely charged electrode to develop thin and thick films, coatings and free-standing bodies [7]. It is a simple and cost-effective technique usually requiring simple processing equipment and infrastructure. In this work, the EPD technique is used to coat a TiO_2/Nb_2O_5 composite porous thin film from nano sized powders of titanium dioxide (TiO_2) and niobium pentoxide (Nb_2O_5) onto a Fluorine doped tin oxide (FTO) glass substrate.

The deposited films were electrically characterized using the Hall Effect equipment. Since Edwin Hall discovered the Hall Effect in 1879, the Hall Effect using Hall meters has continued to provide the basis of many different practical applications. The Hall meters are used in anti-shoplifting systems, motion detection in car ABS systems, home alarm systems, iPhone digital compasses, and car electronic ignition systems [8]. Applications of the Hall Effect measurements are also critical in electrical characterization of semiconductor materials and films because the type of charge carrier, carrier density, and Hall mobility can be derived from the Hall voltage [9],[10]. For semiconductors, the band structure can give rise to both negative (electron-like) or positive (holes). In this work, electrical conductivity is therefore determined by the density and mobility of charges through TiO_2/Nb_2O_5 composite thin films in which volume fraction of Nb_2O_5 is varied in the composite.

II. METHODS

2.1 Film deposition by EPD technique

Masses in the range 0.01g to 0.3g of commercial TiO_2 nanopowder (Cas No. 13463-67-7 Aldrich), and Nb_2O_5 nanopowder (Cas No. 1313-96-8 Acros Organics BVBA, Belgium), and Magnesium nitrate hexahydrate ($Mg(NO_3)_2.6H_2O$ 99.9%, Aldrich) pellets were added into 40 mL of propan-2-ol in a glass beaker to form EPD suspension. Magnesium nitrate hexahydrate pellets were added to suspension to provide magnesium ions to attach to semiconductors and thereby control the zeta potential of suspension [11].

APPENDIX E: PUBLISHED PAPER III

Africa Journal of Physical Sciences ISSN: 2313-3317

Effect of Process-Related Parameters on Band Gap of Electrophoretically Deposited TiO_2/Nb_2O_5 Composite Thin Films

John N. Nguu, Robinson J. Musembi, Francis W. Nyongesa, and Bernard O. Aduda

Department of Physics, School of Physical Sciences, University of Nairobi, P.O. Box 30197-00100, Nairobi, Kenya
E-mail of corresponding author: johnnjagin@yahoo.com or jnguu@students.uonbi.ac.ke

Abstract

Nano-crystalline composite thin films of titanium dioxide and niobium (v) oxide (TiO_2/Nb_2O_5) were successfully deposited on fluorine-doped tin oxide (FTO) coated glass substrate using electrophoretic deposition (EPD) technique. The colloidal suspension utilized in EPD cell consisted of mixture of TiO_2 and Nb_2O_5 nanopowders and 2-propanol in a Pyrex glass. Values of potential difference (25 to 60V) were applied across the EPD electrodes placed in a parallel configuration 1.2cm apart and partially immersed in the suspension. The optimization of EPD parameters was achieved from transmittance measurements and band gap energy calculations. Both Nb_2O_5 and TiO_2 nanoparticles were seen in XRD graphs to be present in the composite films in the ratio 1 to 1.78 which confirmed that both type of nanoparticles suspended in 2-propanol developed positive surface charges and were moved towards and deposited on the cathode upon application of an electric field. The band gap energy was evaluated for films deposited from varied EPD process-related parameters namely, concentration, deposition times and applied potential. The maximum values of band gap were obtained for films electrophoretically deposited from particle concentration of 0.01g/40mL (or 0.25g/L), applied voltage of 35V, and deposition time of 90s. These values of EPD process-related parameters formed the optimum values for deposition of crack free films of good porosity. The changes in band gap values are attributed to either energy shift of conduction band or valence band energy levels. The TiO_2/Nb_2O_5 composite thin films, fabricated in this study from optimized parameters of EPD technique had smooth morphology as shown by SEM images. Further work is needed to evaluate the potential of TiO_2/Nb_2O_5 composite films deposited by EPD for dye–sensitized solar cell application.

Keywords: Electrophoretic deposition (EPD), TiO_2/Nb_2O_5 composite thin films, PV applications, Solar energy, Optical band gap

1. Introduction

Dye sensitized solar cell (DSSC) designs using titanium dioxide (TiO_2) and liquid electrolyte have continuously been improved since 1991 to enhance the efficiency with a current value of 11.5% (Chen *et al.*, 2009). Hindrance to increase in conversion efficiency for DSSCs has largely been transmission difficulty of injected electron through photoelectrode since some of these electrons end up recombining with the oxidized dye or redox mediator in the electrolyte.

The effectiveness of dye-sensitized solar cells in converting sunlight to electric energy depends on several factors among them the efficiency with which light is harvested, and transmitted through the photoelectrode, the number of electrons injected into the photoelectrode, and the ease with which electrons are transported through the photoelectrode (Zhang *et al.*, 2009). Therefore, the photoelectrode can be considered as an essential component that influences the performance of a solar cell. Inside a DSSC, light photons are converted into electric energy on the photoanode (photoelectrode) which consists of nanoporous network of TiO_2 particles sensitized with a layer of visible light absorbing dye. The key to efficient light harvesting is the high surface area of the nanoporous TiO_2 film which provides increased surface area for dye adsorption. It is highly desirable that morphology of the photoanode be optimized, in order to fabricate DSSCs with high efficiency. The efficiency is greatly influenced by the properties of the materials used to fabricate the photoelectrode.

Titanium dioxide (TiO_2) has been the preferred material in fabricating DSSCs because TiO_2 based cells yield higher conversion efficiency than cells made from other semiconductors. Various studies on electrical, structural and optical properties of nanoporous TiO_2 films fabricated techniques like DC magnetron sputtering technique (Eguchi *et al.*, 2000, Suchea *et al.*, 2007), sol gel technique (Traversa *et al.*, 2001), screen-printing method (Chiba, *et al.*, 2006; *Ito et al.*, 2008), pulsed laser deposition (Tonooka *et al.*, 2009), doctor blade (Lee *et al* 2013) and electrophoretic deposition (EPD) technique (Miyasaka and Kijitori, 2004; Yum, *et al.*, 2005; Bandy *et al.*, 2011; and Narayan & Raturi, 2012) have been conducted.

Conventional techniques such as sputtering and pulsed laser require expensive and complicated equipment.